# FIELD OBSERVATIONS OF LINEAR TRANSITION RIPPLE MIGRATION AND WAVE ORBITAL VELOCITY SKEWNESS



ANNA M. CRAWFORD

# FIELD OBSERVATIONS OF LINEAR TRANSITION RIPPLE MIGRATION AND WAVE ORBITAL VELOCITY SKEWNESS



A Thesis Submitted to the
SCHOOL OF GRADUATE STUDIES
in Partial Fulfillment
of the Requirements for the Degree of
DOCTOR OF PHILOSOPHY
at
DEPARTMENT OF PHYSICS AND PHYSICAL OCEANOGRAPHY
MEMORIAL UNIVERSITY OF NEWFOUNDLAND
ST JOHN'S, NEWFOUNDLAND

MAY 2000

# Abstract

A new laser illuminated underwater video system has been developed for simultaneously imaging sediment suspension and monitoring bedforms under waves in the nearshore. The system consists of a video camera and diode laser–generated light plane which illuminates suspended material in section and profiles the bed where it intersects thc bottom. The system was deployed in the field along with acoustic devices for measurement of nearbed flow velocities and independent bedform observation at Queensland Beach, Nova Scotia.

Observations were made in 3 to 4 m water depth of linear transition ripple geometry and migration using the laser–video system and acoustic scanning sensors during both the growth and decay phases of an autumn storm event. Linear transition ripples are long crested, low steepness bedforms in the anorbital ripple class. The transition ripples occurred under relatively high energy waves, just below the flatbed threshold, and had wavelengths of $8.5 \pm 0.5$ cm and heights of $0.3 \pm 0.1$ cm. The maximum observed migration rate was 0.7 cm/min. Migration was offshore during storm growth, and onshore during storm decay. The observed ripple migration rates were highly correlated with nearbed wave orbital velocity skewness ($r^2 > 0.7$).

During storm growth, the incident wave spectrum was bimodal and the orbital velocity skewness was negative. During storm decay, the wave spectrum was unimodal and the velocity skewness was positive. Bispectral analysis shows that the main contribution to negative velocity skewness during storm growth arose from a difference interaction between the two principal components (sea and swell) of the bimodal wave spectrum. Positive velocity skewness during storm decay was due to self–self interaction of the narrowband swell. These observations are shown to be consistent with a second–order wave theory.

These observations support a skewness, or $u^3$, dependence of transition ripple migration on nearbed orbital velocity in a field setting and provide a demonstration of storm modulated off– and on–shore directed ripple migration, thus suggesting a mechanism for the reversible sediment transport cycle during storms.

# Acknowledgements

This work was funded by the Natural Science and Engineering Research Council of Canada and the U.S. Office of Naval Research Coastal Sciences program. Additional support was provided by graduate fellowships from Memorial University of Newfoundland. The field and laboratory experiments forming the basis of this thesis were group efforts involving people from both Memorial University of Newfoundland and Dalhousie University. They are, in no particular order: W. Paul, W. Judge, P. MacAulay, R. Craig, K. Bryan, L. Zedel, C. Pequinet, T. Bowen, J. Foley, B. Roberts, B. O'Donnell, R. Dittman and J. Watson, with special thanks particularly to Doug Wilson and Dave Hazen. The author gratefully acknowledges Steve Elgar, who supplied his bispectrum code for comparison, and along with Steve Henderson, was generally helpful with that analysis. Carolyn Smyth produced velocities from the raw CDP data, and Ian Clarke, surface elevation time series from the pencilbeam data. Constructive comments on the work were offered by supervisory committee members Brad de Young and Len Zedel and examination committee members Yakov Afanasyev and John de Bruyn (who was also an effective administrative expeditor). Bob Guza, the external examiner, provided insightful comments on the analysis leading to significant improvement of the thesis. Thank you for everything, Rick. Lastly, thank you to my supervisor Alex Hay, whose enthusiasm for this work seems to be boundless.

# Contents

# List of Tables

# List of Figures

# Notation

| | |
|---|---|
| $a$ | wave amplitude |
| $a_o$ | wave orbital semi–excursion |
| $a_{1/3}$ | significant wave orbital semi–excursion |
| $A$ | asymmetry |
| $A_b$ | percentage of waves breaking |
| $B$ | bispectrum |
| $c$ | wave phase speed |
| $c_u$, $c_v$ | camera optical centre $x$– and $y$–coordinates |
| $C_m$ | mobile layer reference concentration |
| $d_x$ | video image pixel aspect ratio scaling factor |
| $D$ | median grain diameter |
| $E[\,]$ | expectation value |
| $f$ | frequency |
| $f_w$ | wave friction factor |
| $f_N$ | Nyquist frequency |
| $F$ | complex Fourier coefficient |
| $g$ | acceleration due to gravity |
| $h$ | water depth |
| $H_b$ | wave breaking height |
| $H_{1/3}$ | significant wave height |
| $\Im\{\}$ | imaginary part |
| $K$ | Bagnold's $\mathcal{Q}/\mathcal{W}$ constant |
| $l$ | camera range calibration factor |
| $M_r$ | ripple migration velocity |
| $P$ | power spectrum |
| $P_b$ | particle–particle normal stress |
| $Q_r$ | bedform sediment transport rate |
| $Q$ | grain volume sediment transport rate per unit width |
| $\mathcal{Q}$ | immersed weight sediment transport rate per unit width |
| $r^2$ | correlation coefficient |
| $r1$–$r9$ | rotation matrix coefficients |
| $R$ | autocorrelation function |
| $R_i$ | video image radius from optical centre, undistorted |
| $R_i'$ | video image radius from optical centre, distorted |

| | |
|---|---|
| $\Delta R'$ | radial distortion lens correction |
| $Re_w$ | wave Reynolds number |
| $\Re\{\}$ | real part |
| $s$ | specific gravity |
| $S$ | skewness |
| $t_z$ | camera geometry factor |
| $T_p$ | wave period |
| $T_b$ | particle–particle shear stress |
| $u$ | nearbed orbital velocity (demeaned) |
| $u_m$ | mobile layer reference velocity |
| $u_s$ | streaming velocity |
| $u_*$ | wave boundary layer friction velocity |
| $u_1$, $u_2$ | Stokes expansion velocity coefficients |
| $Ur$ | Ursell number |
| $\mathcal{U}$ | mean nearbed velocity |
| $w_s$ | fall velocity of a sphere |
| $\mathcal{W}$ | rate of energy dissipation near the bed |
| $x_i$, $y_i$ | video image pixel $x$– and $y$–coordinates |
| $x_w$, $y_w$ | object plane world $x$– and $y$–coordinates |
| $\mathcal{A}_i$ | Wells' fundamental frequency coefficient |
| $\mathcal{B}_i$ | Wells' harmonic coefficient |
| $\mathcal{D}_{ij}$ | Wells' difference frequency coefficient |
| $\mathcal{S}_{ij}$ | Wells' sum frequency coefficient |
| $\mathcal{E}_{ij}$ | coefficient in Wells' calculation |
| $\mathcal{F}_{ij}$ | coefficient in Wells' calculation |
| $\mathcal{C}'_{gij}$ | coefficient in Wells' calculation |
| $\mathcal{C}_{gij}$ | coefficient in Wells' calculation |
| $\mathcal{D}'_{gij}$ | coefficient in Wells' calculation |
| $\mathcal{D}_{gij}$ | coefficient in Wells' calculation |
| $\beta$ | bicoherence |
| $\Gamma_1$, $\Gamma_2$ | terms in Wells' $u$ |
| $\delta$ | mobile layer thickness |
| $\epsilon$ | sediment porosity in the bed |
| $\zeta$ | sea surface elevation |
| $\eta_r$ | ripple height |
| $\phi$, $\psi$, $\theta$ | camera pitch, roll and yaw angles |
| $\theta_{2.5}$ | grain roughness Shields parameter |
| $\kappa_1$, $\kappa_2$ | camera lens correction factors |

| | |
|---|---|
| $\lambda_r$ | ripple wavelength |
| $\mu$ | dynamic viscosity of water |
| $\nu$ | kinematic viscosity of water |
| $\xi$ | power law dependence of velocity |
| $\rho$ | water density |
| $\rho_s$ | sediment density |
| $\tau$ | time lag |
| $\tau_b$ | bed shear stress |
| $\phi$ | velocity potential solution for the Laplace equation |
| $\phi_1, \phi_2$ | Stokes expansion velocity potential coefficients |
| $\psi'$ | sediment mobility number |
| $\omega$ | radian frequency |

"Pluralitas non est ponenda sine neccesitate."

"Plurality should not be posited without necessity."

William of Ockham (~1285–1349)

# Chapter 1

# Introduction

Large scale sand beach morphology is determined by sediment transport, which is forced at the fluid–sediment interface. Features of tens to thousands of meters in extent can originate in transport processes operating at centimeter scales. Generally accepted relationships between the local fluid forcing and resulting sediment transport are lacking, especially under the irregular waves typical of field conditions [Kraus and Horikawa, 1990]. Thus, the accurate prediction of many aspects of morphological evolution in the nearshore zone awaits better understanding of the smaller scale processes.

It has long been thought that wave orbital velocity skewness is fundamentally important to the direction and magnitude of net sediment transport. This idea has its physical basis in the difference between the maximum velocities during the forward and reverse flows over a wave period. Net movement of sediment under any oscillatory flow requires a difference between the amount of sediment mobilized during the opposing flows. The third moment of the velocity (unnormalized skewness) appears in transport models based either on energetics arguments [Bagnold, 1963; Bailard and Inman, 1981; Gallagher et al., 1998] or bottom stress [Meyer-Peter and Müller, 1948; Madsen and Grant, 1976]. Though these approaches represent a large fraction of the modeling effort, velocity exponents ranging between 3 and 7 have been suggested [Dyer and Soulsby, 1988]. There are very few reported observations of a direct link between nearbed wave orbital velocity skewness and

local sediment transport rate in the literature. Observations of this type would help to resolve the question of the wide variation in the velocity exponent used in sediment transport models.

Results are presented in this thesis which are based on field observations of bedforms which occurred during relatively energetic wave conditions. These measurements were made possible in part by a novel underwater laser–illuminated video system designed for measurement of bedforms and sediment suspension [Crawford and Hay, 1998]. The high resolution capability of the system allowed detailed ripple geometry measurements. Together with an acoustic bed profiling system and high quality velocity measurements, observations of ripple migration were obtained in conjunction with measurements of nearbed orbital velocities. The observations show both onshore and offshore migration of linear transition ripples at velocities which correlate to positive and negative orbital velocity skewness. The particular ripple type focused on in this study are low relief, long crested bedforms which exist in conditions of high energy flow and high sediment transport rate. It is proposed that these bedforms represent a diagnostic sediment transport indicator. As far as this author is aware, this is the first clear observation of a link between local wave orbital velocity skewness and a sediment transport indicator, in this case, bedform migration, spanning both onshore and offshore transport directions.

Establishment of an equilibrium beach profile requires a balance in the cross–shore direction between on and offshore components of sediment transport [Bowen, 1980]. The second–order flows most commonly thought of in relation to mass transport by waves, streaming velocity and wave drift, are in the direction of wave travel (onshore). Wave skewness in the nearshore is most commonly observed to be positive, which would also move sediment onshore. Mechanisms for transport of sediment in the offshore direction are less well understood. Offshore transport can be driven by offshore mean flows, such as undertow or rip currents which are sporadic, assisted by the beach slope (gravity). Observations of negatively skewed nearbed orbital velocities are few despite the theoretical basis provided by second–order theories such as by Wells [1967] and Longuet-Higgins and Stewart [1962]. The observations of offshore bedform migration presented in this

work demonstrate that negative skewness of the nearbed wave forcing can drive offshore sediment transport when the incident wave conditions are conducive.

The skewness of a time series quantity is a measure of the asymmetry of the distribution of the set of observations. In wave time series, nonzero skewness can arise through nonlinear processes, and so skewness becomes a measure of nonlinearity. Bispectral analysis is a technique well suited to identifying phase coupled weakly nonlinear interactions, which are an integral part of the nearshore wave forcing environment. The bispectrum has been used in this work to identify wave interactions leading to the observed velocity skewness and provides the basis for understanding the observed on– and offshore bedform migration in terms of second–order wave theory.

This introductory chapter continues with a review of previous work on bedform measurements and classification, with emphasis on nearshore field observations. A brief review of the use of underwater imaging in bedform and sediment dynamics measurements is then given, including a conceptual description of the video technique developed as part of this work. An overview of bedform migration observations follows. Discussion of nearshore wave forcing and a brief summary of the velocity dependence aspect of sediment transport modeling follow. An overview of bispectral analysis is then presented. The chapter closes with a brief summary of the organization of the remainder of the thesis.

## 1.1 A Brief History of Bedform Measurements

Bedforms can be observed in any situation where fluid flows over a movable granular bed. This includes deserts, gravel river beds, tidal mud flats, wind blown snow, and sand beaches. The ripples reported in this thesis were formed in nearshore sands by wave action. Oscillation ripples are different from those produced by unidirectional flow in having a more symmetric shape. As well, the migration direction of oscillation ripples under real ocean waves, as opposed to unidirectional flow, is governed by more complicated processes than first inspection might suggest. The following brief historical review of bedform measurements will focus on field observations, which have been relatively few

in comparison to the larger body of laboratory work on the subject.

In general, the motivation behind most early oscillation bedform studies was to create a ripple type versus flow parameter "phase diagram" in order, for example, to infer paleoenvironment from fossilized bedforms [Allen, 1982; Clifton and Dingler, 1984]. In recent decades, with attention turning toward understanding the dynamics of sediment transport, emphasis has been shifting to the study of bedforms in the context of boundary layer flow [Grant and Madsen, 1982; Conley and Inman, 1992; Hay et al., 1999]. This has been made possible by significant advances in applicable technology, both for measurement of the bedforms themselves and of the overlying flow field.

It is an indication of the shortage of reported field observations of oscillation ripples that despite technological advances, some of the most frequently cited studies remain the SCUBA diver observations of Inman [1957] and Miller and Komar [1980a]. These were obtained in relatively clear water, at depths of between 5.5 and 21 m [Inman, 1957] and between 9 and 33 m [Miller and Komar, 1980a]. Diver observations in the nearshore are limited by surf conditions and visibility and are inherently intrusive in a flowing fluid environment. Dingler and Inman [1977] point out that

> ... ripple heights are almost impossible to measure manually because the weight of the meter stick flattens the crests and because constant water motion from the waves disrupts the measurement ...

Diver observations are also reported by Clifton et al. [1971], Davidson-Arnott and Greenwood [1976], Sherman and Greenwood [1984] and more recently by Osborne and Vincent [1993]. Typically, divers measured ripple spacing or height by ruler (some made grease pencil marks), or visual estimation. Other techniques include measurement of ripple shape by pressing a greased comb–like device into the sand [Inman, 1957; Kawata et al., 1990] and photography [Inman, 1957] (to be discussed further in Section 1.3). Advances in the study of what is fundamentally a boundary layer phenomenon have required development of instrumentation that does not "disrupt" the area under observation and can be deployed in other than quiescent conditions.

The first widely cited quantitative bedform observations obtained using a suitably remote measurement method, in this case a track–mounted sonar altimeter, were obtained by Dingler [1974], and reported in Dingler and Inman [1977]. This set of observations appears to be one of the most frequently cited in the literature [a few examples are Miller and Komar, 1980a; Nielsen, 1981; Clifton and Dingler, 1984; Boyd et al., 1988; Wiberg and Harris, 1994]. Other track–mounted and fixed altimeter type sonar systems have subsequently been widely used [McLean, 1983; Greenwood et al., 1985; Hanes et al., 1988; Osborne and Vincent, 1993; Vincent and Osborne, 1993; Hay and Bowen, 1993; Gallagher et al., 1996].

In the past decade, the introduction of side–scan type sonar systems has revolutionized the field of nearshore bedform observations. It is now possible to remotely monitor bedform development over wide areas in real time through conditions entirely prohibitive to divers [Hay and Wilson, 1994; Thornton et al., 1998; Hay and Bowen, 2000; Traykovski et al., 1999].

The previous discussion has centred on acoustic techniques since most of the recent technical advances applicable to bedform measurements have been in this area. A notable exception is in the area of diode laser technology, which has made possible the structured lighting approach developed for the laser–video system described in this thesis.

## 1.2 Systems of Bedform Classification

The early work in oscillation bedform field observation and laboratory experiments has resulted in diagrams like that shown in Figure 1.1, from Clifton and Dingler [1984]. The data shown are a combination of field and laboratory observations from a number of investigators (see figure caption). The schematic diagram, Figure 1.1b, describes the division of ripples into various classifications according to the dependence of their wavelength on wave orbital diameter (the maximum horizontal excursion a particle following the wave orbital velocity would undergo through one wave cycle). For waves of a given period, orbital diameter is proportional to wave height. Over the range of small to medium waves,

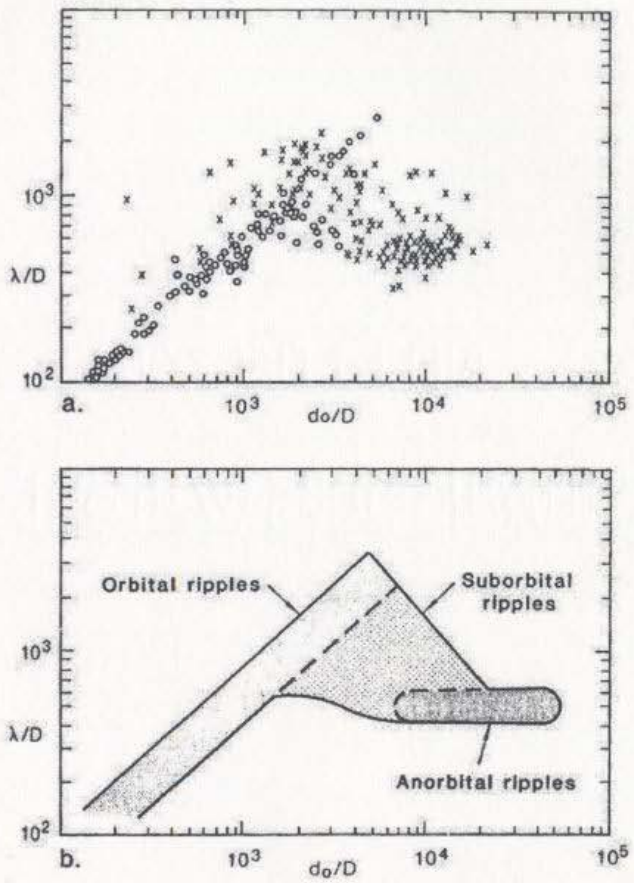


Figure 1.1: Ripple spacing $\lambda$ as a function of orbital diameter $d_o$, normalized by grain diameter $D$, from Clifton and Dingler [1984]. In (a), $\times$ indicate field data (Inman [1957], Dingler [1974], Miller and Komar [1980a], Dingler and Clifton [1984]) and $\circ$ show laboratory data (Carstens et al. [1969]; Mogridge and Kampuis [1973]; Miller and Komar [1980b]). (b) is a schematic representation of the data shown in (a) with three ripple types indicated.

ripple wavelength is proportional to orbital diameter (*orbital* ripples). Ripple wavelength shows little wave orbital diameter dependence under large waves (*anorbital* ripples). In the middle, between orbital and anorbital ripples, are *suborbital* ripples. The lower bound on the classification scheme is determined by the threshold of motion of sediment on the bed, below which any ripples present are left over from previous disturbance (*relict* ripples). Under very large waves, high flow velocities scour the bed of ripples (*flatbed*).

A complementary scheme divides ripples into *vortex* and *rolling grain* ripples [Bagnold, 1946; Sleath, 1984, Chapter 4]. Vortex ripples are maintained by flow separation at the ripple crest, which forms a vortex in the lee trough during each wave half–cycle. The vortex–generated backward flow on the lee side pushes sand toward the crest so that the ripple shape is peaked. Rolling grain ripples form when the flow does not separate at the crests. These ripples have a lower relief, more sinusoidal shape than vortex ripples. Historically, this bedform class has included both a low and high energy case [Sleath, 1976; Allen, 1979] — in vigorous flow almost strong enough to erase ripples altogether, ripple steepness can be decreased to a point where flow separation does not occur. In the work presented here, which deals with the higher flow energy case, ripples in this second regime have been differentiated from the lower energy case by calling them *transition* ripples, following Dingler and Inman [1977].

There are many field observations of ripple types that do not fit clearly into these schemes, since they do not include consideration of three–dimensional ripple types. *Cross* ripples [Clifton, 1976] have crests aligned obliquely to the dominant wave forcing direction and often have a bimodal ripple wavelength distribution (Hay and Wilson [1994] describe shorter wavelength vortex ripples with superimposed larger oblique crests in a diamond shaped pattern). These are observed under moderate to high energy flows. *Megaripples* are of larger scale, O(1 m), than the bedforms mentioned so far and occur in high energy conditions [Clifton, 1976; Hay and Wilson, 1994; Hay and Bowen, 2000]. They are often solitary features, generally lunate in shape and due to the large sediment volume they represent, can contribute significantly to sediment transport when migrating [Hay and Bowen, 2000].

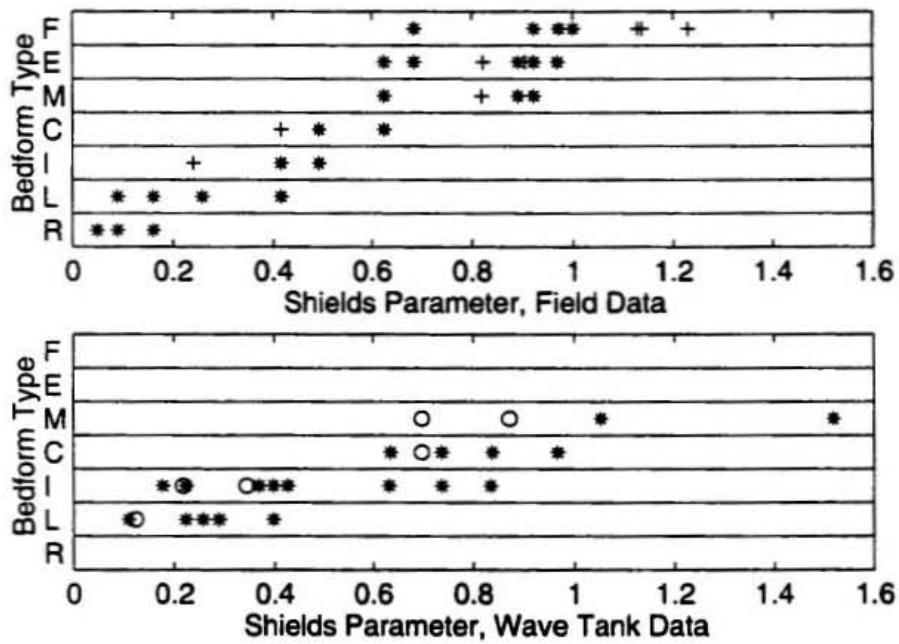


Figure 1.2: Bedform type as a function of Shields parameter for laboratory and field data. In the upper panel, $*$ and $+$ are from two storm events in the field data, and in the lower panel, $\circ$ and $*$ are from two different laboratory experiments. The ripple types are *R*elict, *L*inear, *I*rregular, *C*ross, *M*ega, *E*vanescent or *F*latbed (from [Wilson and Hay, 1995]).

Clifton [1976] originally proposed an hierarchy of bedforms as a function of distance offshore (water depth). Hay and Wilson [1994] showed that an equivalent progression can occur at one location as a function of time through a storm. A progression scheme of this type is perhaps the most useful classification system for bedforms observed in the field. Wilson and Hay [1995] present observations of ripple type as a function of increasing oscillatory flow energy from both field and laboratory experiments. Following Clifton [1976], ripple type was defined as *R*elict, *L*inear, *I*rregular, *C*ross, *M*ega, *E*vanescent or *F*latbed. Their results are shown in Figure 1.2, plotted against Shields parameter, $\theta_{2.5}$ given by

$$\theta_{2.5} = \frac{\tau_b}{(\rho_s - \rho)gD} \tag{1.1}$$

where $\tau_b$ is the bottom stress, $\rho_s$ and $\rho$ are the densities of sediment and water, $g$ is acceleration due to gravity, and $D$ is median sediment grain diameter (the subscript 2.5 refers to the roughness length of $2.5D$ used in calculating $\tau_b$, see Section 3.1). The Shields parameter can be thought of as the ratio of the horizontal force exerted on a particle by the shear stress and the force of gravity. The Shields parameter is often used to characterize oscillatory flows; for example, it is generally recognized that a Shields parameter of approximately 1 or greater is required for flatbed [Nielsen, 1981]. The evanescent ripples of Wilson and Hay [1995] ("short lived linear ripples observed intermittently by the sonar") are most likely anorbital and could very well be *transition* ripples — observations of bedforms of this type have led to the bulk of the results presented in this thesis (Chapter 3).

## 1.3 Underwater Imaging Techniques and Structured Lighting

Measurement of oscillation bedforms using video or photography is common in a laboratory setting [Bagnold, 1946; Carstens et al., 1969; Sleath, 1984; Yokokawa et al., 1995].

In the field, however, there are far fewer instances. Although these methods offer a non-intrusive measurement technique that is relatively uncomplicated and intuitively understandable, they are subject to obvious visibility limitations, particularly in the nearshore environment.

As early as 1957, Inman mentions photography of bedforms (some photographs are included in Inman's Technical Report), but the published results come from diver measurements (similarly in Clifton et al. [1971]). Inman [1957] briefly mentions use of underwater video. Several investigators report deployment of underwater cameras or video equipment for purposes of monitoring conditions at the measurement site [Hay and Bowen, 1993; Osborne and Vincent, 1993], but do not attempt quantitative use. An interesting early case of bedform measurements is by Sternberg [1967], who reported ripple migration velocities under tidal flow obtained using an underwater video camera directed downward at the bed. Ripple crests were traced from a television monitor at 5 minute intervals and the migration velocity determined from the integrated area between successive crest positions. Dyer [1980] reported observations of the frequency of sediment movement under tidal currents which were estimated visually from close–range underwater video footage of the bed. Boyd et al. [1988] used time lapse photo images to observe bedform type and migration under waves in 10.5 m water depth. Conley and Inman [1992] used video in the nearshore to obtain qualitative observations of sediment suspension in relation to fluid–granular boundary layer flow observations.

The observations summarized in the preceding paragraph were obtained under ambient lighting conditions. As previously mentioned, the primary limitation of video, in energetic conditions particularly, is visibility. Structured lighting is an effective method of increasing the video signal–to–noise ratio, extending the range of suitable visibility conditions. This technique can also simultaneously provide a means of determining position in the camera field of view, allowing quantitative geometric measurements to be made. Various lighting techniques have been used successfully for imaging floc particles and plankton in the deep ocean [for example, Honjo et al., 1984; Lenz et al., 1995; Ratmeyer and Wefer, 1996]. Lasers are a convenient light source and have been used underwater in a variety

of imaging applications, mostly associated with Remotely Operated Vehicle (ROV) vision systems. Laser spots at fixed points in the camera field of view have been used to obtain size estimates of benthic organisms [Tusting and Davis, 1992]. A photo–multiplier tube receiver synchronized to a rastered laser light point has been used to enhance ROV vision for underwater salvage operations [Kulp et al., 1993]. Fournier et al. [1993] report another ROV vision system utilizing a range–gated laser light source. The lasers used in these applications are argon–ion, He-Ne or diode pumped Nd:YAG lasers. The very recent developments in efficient, higher power diode lasers in a wide range of wavelengths will no doubt soon lead to an increase in their use over earlier laser technologies.

Though any of the previously mentioned techniques would be suitable for quantitative measurement of bedforms, there are *very* few instances in the literature of the use of structured lighting for bedform measurements. Wilkinson [1986] used a flood light and shadow bar to obtain ripple geometry measurements from photo images. Ripple wavelength and height were determined from the shadow cast by the bar, knowing the relative positions of the camera, light source and bar. A similar technique was used on the continental shelf by Li and Amos [1998].

The laser–video system to be described in this thesis was developed with the goal of obtaining time series of instantaneous two–dimensional images of structure in the suspended sediment field and simultaneous bed profiles over a length greater than a wave orbital diameter. The realization of this idea uses compact low–power diode lasers to produce an illuminated section which is viewed from the side by a small black–and–white CCD camera. The system is shown conceptually in Figure 1.3. Once the camera field of view is calibrated, position in the illuminated plane can be determined to millimeter accuracy. This represents very high resolution in comparison to typical MHz–frequency acoustic systems, for example, which can realize millimeter resolution in range, but for which the size of the "footprint" of the beam pattern leads to spatial averaging of the bottom return over several centimeters in the horizontal. In a slant orientation, the width of the beam pattern can be utilized to advantage, but ripple height information cannot be obtained, and the far sides of ripples can be in acoustic shadow. In the context of the

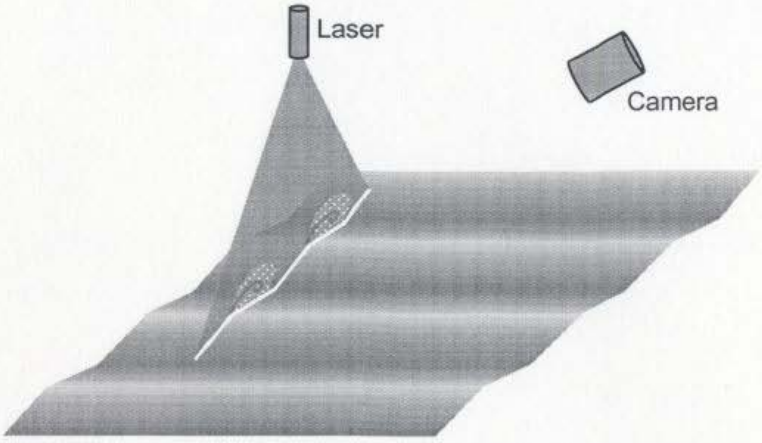


Figure 1.3: Cartoon of the laser–video imaging system concept. Ripples are profiled where the laser sheet intersects the bed and suspended material is also illuminated. A camera images the laser section from the side.

measurements to be presented in Chapter 3, the low relief ($< 0.5$ cm) of the observed transition ripples required the high spatial resolution of the laser–video system to obtain accurate measurements of ripple geometry.

## 1.4 Bedform Migration Observations

Bedforms appear to migrate as sediment is removed from one ripple slope and deposited on the other. Under oscillating flow, this requires a flow asymmetry for the same reason as it is required for sediment transport in general. Individual grains involved in the migration process may travel distances greater than a ripple wavelength between being mobilized and deposited. Bedform transport, defined by the volume of sediment contained in the migrating bedforms, can then occur through a combination of bedload and suspended load modes of sediment transport. There is no accepted relationship governing the relative contribution to bedform transport by both modes, though Bagnold [1941] argues that for large scale bedforms and possibly ripples, the migration rate is in proportion to the total sediment transport load.

Two relationships for bedform transport $Q_r$ as a function of ripple geometry and migration velocity have been proposed. Bagnold [1941] defined $Q_r$ as

$$Q_r = \eta_r M_r \rho_s (1 - \epsilon) \tag{1.2}$$

where $\eta_r$ is ripple height, $M_r$ is ripple migration velocity, $\rho_s$ is the sediment density and $\epsilon$ is the porosity of the bed. Allen [1970] defined

$$Q_r = \frac{1}{2} \eta_r M_r \rho_s (1 - \epsilon) . \tag{1.3}$$

These relationships differ by a factor of 2, reflecting the difference between including (for a ripple of roughly triangular profile displaced by a wavelength) the area swept by the advancing ripple face per time and the ripple volume per width per time. One perhaps defines a maximum, and the other an average [Amos et al., 1999].

A brief summary of some of the relevant observations of ripple migration reported in the literature follows. Sternberg [1967] made video measurements of ripple migration (as discussed in Section 1.3) and flow velocities in a tidal channel in 20 m water depth. Under unidirectional flow, he found

$$M_r = (1.45 \text{ to } 12.6) \times 10^{-10} u_{10}^5 \tag{1.4}$$

where $u_{10}$ is the 5–minute averaged horizontal velocity 10 cm above the bed. In the nearshore zone, Dingler and Inman [1977] found positive correlation between onshore ripple migration rate and Longuet-Higgins' [1957] nearbottom streaming velocity,

$$u_s = \frac{5(2a_o\omega)^2}{4c} , \tag{1.5}$$

where $a_o$ is the orbital semi–excursion, $\omega$ is the wave radian frequency and $c$ is the wave phase speed. $u_s$ depends on orbital velocity squared or flow energy since $a_o\omega \sim 2u_{\text{rms}}$. This predicts ripple migration only in the direction of wave propagation. Boyd et al. [1988] observed ripple migration in 10 m water depth off a sand beach. Their "type 1" ripples were most likely transition ripples, and were observed migrating in both on and offshore directions. They found no significant relationship between velocity skewness

and ripple migration velocity citing insensitivity and instability of the electromagnetic flow meters and possibly characteristics of the vertical structure of the nearbed flow field as possible reasons. They state that offshore migration of ripples was observed under the largest waves during two storms, when onshore directed streaming velocity would be strongest. Vincent and Osborne [1993] report observations of ripple migration on a macro–tidal beach. They looked for a relationship between ripple migration velocity and three dimensionless parameters: Shields parameter (see Equation 1.1), wave Reynolds number

$$Re_w = \frac{2u_{\max}a_o}{\nu} \tag{1.6}$$

and mobility number

$$\psi' = \frac{(2a_o\omega)^2}{(s-1)gD} \tag{1.7}$$

where $\nu$ is the kinematic viscosity of water and $s$ is the sediment specific gravity. $u_{\max}$ was defined as the average of the highest one–third of the maximum current speeds (or the significant velocity) in the shoreward half cycles of the waves only. Similar to $u_s$, the three parameters $\theta_{2.5}$, $Re_w$ and $\psi'$ are all representative of wave flow energy. They found no significant relationship between the observed migration velocity of "small" ripples and any of the three parameters. They observed transition ripples on at least one occasion, but do not separate ripple types beyond "large" and "small". Amos et al. [1999] observed ripples in combined wave–current flow conditions on the continental shelf. The ripples they observed were primarily current formed (unidirectional) and they found the migration velocity to be a function of the current component of the combined flow. Finally, Traykovski et al. [1999] observed migration of ripples in 12 m water depth. They observed predominantly onshore migration and found qualitative agreement between the cumulative integrals of $\overline{u^3}$ and ripple displacement.

To summarize, the observations of Sternberg [1967] and Amos et al. [1999] were under unidirectional or combined flows. Under waves alone, Dingler and Inman [1977] found correlation between ripple migration velocity and a measure of flow energy ($u_s$), while Vincent and Osborne [1993] found no correlation between ripple migration rate and any

of several similar flow energy parameters ($\theta_{2.5}$, $Re_w$ and $\psi'$). These results were biased toward the onshore ripple migration direction. Boyd et al. [1988] failed to find correlation between ripple migration and orbital velocity skewness (including observations of transition ripples), but cited probable inadequacy of the velocity measurements. The observations of Traykovski et al. [1999], similar to the observations to be reported here, support a relationship between velocity skewness and ripple migration, but are limited to the onshore migration direction.

It should be pointed out that the large majority of ripple migration observations were of ripple types other than transition ripples (with the exception of some of the observations of Boyd et al. [1988] and Vincent and Osborne [1993]). It is quite probable that the mechanisms involved in migration of vortex ripples, for example, are quite different than those involved in migration of transition ripples. These ripple types occur under different flow conditions and couple with significantly different boundary layer flows, necessitating separation of ripple types when looking for relationships between ripple migration and the fluid forcing. The fundamental requirement for an asymmetry in the oscillating flow, however, remains in any case.

## 1.5 Wave Orbital Velocity Forcing in the Nearshore

Nearshore dynamic processes are primarily forced by the incoming waves. Examples include longshore currents driven by non–normally incident waves, undertow and rip currents, all of which can move sediment, ultimately determining beach morphology. The morphology in turn controls the large scale flows, making the large scale system intrinsically nonlinear.

Waves in the nearshore undergo nonlinear evolution while shoaling over a sloping bottom. The general characteristics of the local wave forcing are usually given by bulk measures such as the peak spectral period, $T_p$, and root–mean–square surface elevation, $\zeta_{rms}$, or significant wave height, $H_{1/3}$ (the average height of the one third largest waves). As

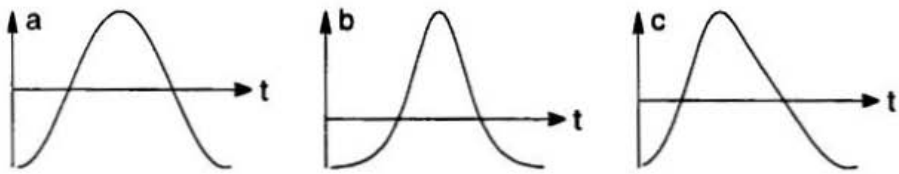


Figure 1.4: Example wave forms illustrating skewness and asymmetry. The $y$ axes could represent surface elevation or a component of wave orbital velocity and all have been demeaned. (a) A sinusoidal wave form contributes zero skewness and asymmetry to a time series. (b) A wave form showing positive skewness (peakedness) and zero asymmetry. (c) A wave form showing non–zero asymmetry.

shoaling progresses, waves become more peaked and lean toward shore. The manifestation of this nonlinear process in measured time series quantities can be described in terms of higher statistical moments, specifically wave skewness $S$ and asymmetry $A$. Skewness describes the departure from symmetry about zero of the distribution of the demeaned measurements. Mathematically, skewness of a time series $x(t)$ is determined from

$$S = \frac{E[x^3]}{E[x^2]^{3/2}} \tag{1.8}$$

where $E[\,]$ is the expectation value (see Equation 1.34) and $x$ has been demeaned. Asymmetry is the skewness of the Hilbert transform of the time series. The Hilbert transform phase shifts each Fourier component of the time series by $\pi/2$, so that the even and odd components are exchanged. Even functions have non–zero skewness and zero asymmetry, and odd functions have zero skewness and non–zero asymmetry (consider $E[\cos^3\theta]$ and $E[\sin^3\theta]$ in Equation 1.8). In terms of quantities that would typically be measured in the nearshore (surface elevation or orbital velocity, for example), Figure 1.4 shows examples of wave forms that would contribute non–zero skewness or asymmetry to a time series. A purely sinusoidal wave form, in the time series sense, has zero skewness and zero asymmetry. Waves with flattened troughs and peaked crests are positively skewed and waves that lean toward one side have non–zero asymmetry. As waves shoal they evolve from sinusoidal in deep water, increasing in skewness and asymmetry until they attain a shape exaggerated enough that they break.

In the nearshore, incident wave energy is distributed over a spectrum of frequencies.

Nonzero wave skewness arises as a result of nonlinear interaction between the frequency constituents of the wave forcing during the shoaling process. For narrowbanded waves, self–self interaction can lead to the development of harmonics and to positive skewness, as in the usual Stokes expansion. Hasselman et al. [1963] showed that a difference interaction between two wave trains of different frequency (as in a bimodal spectrum) gives negative skewness associated with the beat or wave group frequency response. In the presence of a broad band wave spectrum, simultaneous sum and difference frequency interactions are possible and the resulting wave skewness is the sum of the positive and negative contributions from all interactions. Elgar and Guza [1985a] presented clear examples of the evolution of bimodal, narrow and broad banded bottom pressure spectra (and the associated wave skewness and asymmetry) through these nonlinear interactions as waves shoal.

The most basic second–order theory describing ocean waves uses the Stokes expansion. Many of the observed second–order flows, for example, drift or mass transport velocity [Longuet-Higgins, 1957], can be derived following this approach. This comes from solving the (irrotational, inviscid) Laplace equation, with appropriate boundary conditions, for a linear first order potential, plus a perturbation (second–order) term,

$$\phi = \phi^{(1)} + \phi^{(2)} = \phi_1 \sin \omega t + \phi_2 \sin 2\omega t \tag{1.9}$$

where $\phi_1$ and $\phi_2$ are coefficients which depend on wave amplitude $a$, water depth $h$ and vertical position $z$. The horizontal velocity $u$ is given by

$$u = \frac{d\phi}{dx} = u_1 \cos \omega t + u_2 \cos 2\omega t \tag{1.10}$$

where

$$u_1 = a\omega \frac{\cosh k(h-z)}{\sinh kh} \quad , \tag{1.11}$$

$$u_2 = \frac{3}{4} a^2 k\omega \frac{\cosh 2k(h-z)}{\sinh^4 kh} \quad . \tag{1.12}$$

and $k$ is the wavenumber, $2\pi$/wavelength. In order that the expansion is valid, the perturbation term must be much smaller than the first order term, i.e.

$$\frac{\frac{3}{4}a^2k\omega/(kh)^4}{a\omega/kh} = \frac{3}{4}\frac{ak}{(kh)^3} \ll 1 \,. \tag{1.13}$$

The quantity $3ak/4(kh)^3$ is known as the Ursell number, $Ur$. The requirement that $Ur \ll 1$ means that wave amplitude and steepness are limited to small values as $kh$ becomes small in shallow water. The Stokes expansion description of $u$ yields a wave orbital velocity with positive skewness.

The significance to sediment transport of a skewed horizontal orbital velocity, is that physically, skewness represents a mismatch between the magnitudes and durations of the maximum forward and backward velocities over a wave cycle. If more sediment can be mobilized during one half wave cycle than the other, then this represents the potential for net transport of material. Under flow conditions near the threshold for sediment movement, it is possible for sediment to be in motion only during that part of the larger velocity wave phase when the critical value of shear stress is exceeded. In symmetric waves, though much material may be moving, the net transport will be zero. The shoaling of waves as they enter shallower water, however, precludes this hypothetical situation in the natural nearshore. One of the primary difficulties in sediment transport measurement is that the net quantity is the small difference between two sometimes large and generally uncertain quantities.

## 1.6 Orbital Velocity Dependence in Sediment Transport Models

It is not the purpose of this thesis to examine sediment transport processes or modeling in detail (there will be no computed transport results presented, for example). A brief description of some of the commonly cited cross–shore transport models will be given, however, to highlight, firstly, the importance of finding a $u^3$ (or skewness) dependence in the field, and then, the importance of determining the appropriate exponent in the velocity

dependence. The skewness and the cube of velocity are intimately related in that skewness is equal to the cube of the demeaned velocity normalized by the cube of the root–mean–squared velocity (Equation 1.8). In very general terms, the sediment transport models can be divided into those that are based on an energetics argument (following Bagnold [1963]) and those based on a bed stress argument (as in Madsen and Grant [1976]).

The energetics argument, as originally put forward by Bagnold [1963], follows the reasoning that the sediment transport rate $\mathcal{Q}$ is proportional to the rate of wave energy dissipation near the bottom $\mathcal{W}$, or

$$\mathcal{Q} = K\mathcal{W} \tag{1.14}$$

where $\mathcal{Q}$ is defined as the immersed weight transport rate of sediment per unit width of flow with units of mass/time$^3$, and $\mathcal{W}$ is the rate of energy dissipation near the bed, with the same units. $K$ is a dimensionless efficiency parameter which Bagnold separated into contributions from bedload and suspended load. The energy dissipation is due to bottom friction, so

$$\mathcal{W} = \tau_b u \tag{1.15}$$

where $\tau_b$ is the bed shear stress and $u$ is a representative orbital velocity outside the boundary layer. The bottom stress is given by

$$\tau_b \propto \rho u^2 \tag{1.16}$$

where $\rho$ is the water density. This gives the result

$$\mathcal{Q} \propto u^3 . \tag{1.17}$$

This basic model has subsequently been extended by Bailard and Inman [1981] to include time varying velocities, and also used, for example, in equilibrium beach profile modeling by Bowen [1980] and bar evolution by Gallagher et al. [1998].

An alternate line of reasoning, as originally proposed by Meyer-Peter and Müller [1948] for unidirectional flow, is based on the movement of material in response to the

applied bed shear stress. Using laboratory data, they looked for an empirical relation of the form

$$\mathcal{Q} \propto \tau_b^{\xi} \tag{1.18}$$

where $\mathcal{Q}$ is as defined above (units of mass/time$^3$). They found $\xi = 3/2$, i.e.

$$\mathcal{Q} \propto u^3 . \tag{1.19}$$

In oscillatory flow, Madsen and Grant [1976] found an empirical result for the volume transport rate, $Q(t)$, proportional to the third power of a time–varying Shields parameter

$$\theta(t) \propto \tau_b(t) = \frac{1}{2} f_w \rho |u(t)| u(t) . \tag{1.20}$$

Their result, in non–dimensional form, is

$$\frac{Q}{w_s D} \propto \left[ \frac{\tau_b(t)}{(\rho_s - \rho) g D} \right]^3 \tag{1.21}$$

where $w_s$ is the fall velocity of a sphere with diameter $D$. This gives

$$Q \propto |u(t)|^3 u(t)^3 . \tag{1.22}$$

Note however that in Equation 1.20, $\tau_b$ is a function of the wave friction factor $f_w$, which may also contain velocity dependence, as discussed further below. $Q$ has dimensions of length$^2$/time, and can be related to $\mathcal{Q}$ by

$$\mathcal{Q} = (\rho_s - \rho) g D Q . \tag{1.23}$$

Sleath [1994] developed a model for bedload transport in oscillatory flow from first principles which divides sediment transport into inertial and viscous flow regimes, following the work of Bagnold [1954]. Briefly summarizing, a mobile layer thickness $\delta$ is defined in terms of the concentration profile,

$$\delta = \frac{1}{C_m} \int_0^{\infty} C \, dz \tag{1.24}$$

where $C$ is sediment concentration and $C_m$ is the reference concentration at the stationary base of the mobile layer. The velocity and concentration profiles are assumed to be generalized forms in terms of the non–dimensional vertical coordinate $z' = z/\delta$. Based on the empirical results of Bagnold [1954], in the inertial regime, the particle–particle shear stress $T_b$ in the mobile layer is given by

$$T_b \propto \left(\frac{du}{dz}\right)^2 \tag{1.25}$$

which by scale arguments, gives

$$T_b \propto \left(\frac{u}{\delta}\right)^2 . \tag{1.26}$$

It is assumed that the tangential stress $T_b$ is proportional to the normal stress $P_b$ at the bottom of the mobile layer: $T_b = K_b P_b$. $P_b$ is taken to be equal to the vertical integral of the immersed weight of the sediment, and so $P_b \propto \delta C_m$. Thus, $T_b \propto K_b C_m \delta$. Assuming that at the bottom of the mobile layer $T_b = \tau_b$, the shear stress at the bed, then

$$\tau_b \propto \delta \tag{1.27}$$

which combined with Equation 1.26 gives

$$u \propto \delta^{3/2} . \tag{1.28}$$

The volume rate of sediment transport is given by

$$Q = \int_0^\infty u C \, dz \tag{1.29}$$

where $Q$ is defined previously. Combining Equations 1.28 and 1.29 and using a generalized form of the concentration profile gives

$$Q \propto \delta \int_0^\infty u C \, dz' \propto \delta^{5/2} \propto \tau_b^{5/2} \tag{1.30}$$

in the inertial flow regime. This is Sleath's central result which he shows to be consistent with available laboratory data. The $\tau^{5/2}$ dependence arises through the proportionality of the mobile layer thickness on bottom stress. The Bagnold relationship (Equation 1.25)

gives a velocity scale which has a $\delta^{3/2}$ dependence, with an additional factor of $\delta$ coming from the vertical integral in the transport. Returning to the original definition for $\tau_b$, Equation 1.16, this suggests a $u^5$ dependence of transport rate on velocity.

While Bagnold [1963] shows a $u^3$ dependence in the transport rate and Madsen and Grant [1976] show $u^6$, the Sleath [1994] model exhibits a $u^5$ dependence. The review of sediment transport modeling by Dyer and Soulsby [1988] states that the exponential dependence of $\tau_b$ in models found in the literature ranges from 3/2 to 7/2. Another more detailed summary of the range of velocity dependence is given by King and Seymour [1989]. They recast the variables used by the various authors as transport rate/wave energy dissipation $\mathcal{Q}/\mathcal{W}$ and find, among 7 models, the exponential dependence on Shields parameter ($\propto u^2$) varies between 0 and 3/2, giving $u$ an exponent between 0 and 6 (recalling that $\mathcal{W} \propto u^3$). In addition to showing different power law dependence, they find that the predictions for $\mathcal{Q}/\mathcal{W}$ by the 7 models at a Shields parameter value of 1, for example, span 2 orders of magnitude. A similar listing of models, with some overlap, is given by Horikawa [1988]. The majority in Horikawa's list have $u^3$ dependence, with some models showing $u^6$ and a few showing other exponents in the range 1 to 2.

A further consideration is the shear stress dependence on the wave friction factor $f_w$. This has been treated as a constant by some authors [Bagnold, 1963], however, it more often contains hidden velocity dependence. An example of this is in the commonly used empirical fit for $f_w$ by Swart [1974] (to the earlier semi–empirical relation by Jonsson [1966]) for rough turbulent flows over a flat bed with fixed grain roughness

$$f_w = \exp\left(5.213\left[\frac{2.5D}{a}\right]^{0.194} - 5.977\right) \tag{1.31}$$

where $D$ is the median grain diameter. This contains $u$ dependence in $a$, the orbital semi–excursion (see Section 1.4). This gives $f_w$ a weak dependence on averaged $u$ (an exponent of about $-0.3$ for a grain diameter of 175 $\mu$m and typical values of $a$). Apart from the $u$ dependence, there is large uncertainty in assigning an appropriate value to the roughness length ($2.5D$ in the above example), particularly in the case of oscillatory flow over bedforms. There is an extreme shortage of roughness measurements for movable beds in

oscillatory flow [Sleath, 1995].

In summary, existing sediment transport models exhibit dependence on a range of powers of wave orbital velocity, including $\langle u^3 \rangle$ which is related to velocity skewness. Higher order statistical moments such as skewness can be used to describe aspects of the behaviour of dynamical systems that arise through nonlinear processes. Bispectral analysis is a powerful tool used in the study of nonlinear interactions, as will be described in the following section.

## 1.7 Bispectral Analysis

As discussed in Section 1.5, wave shoaling and the associated evolution of wave skewness and asymmetry are fundamentally nonlinear processes. Higher order spectral analysis, more particularly bispectral analysis, allows identification of nonlinear interactions in time series. One of the first applications of this technique was to the study of waves by Hasselman et al. [1963]. Since then, it has been used extensively [Elgar and Guza, 1986; Herbers and Guza, 1994; Elgar et al., 1995; Doering and Bowen, 1995; Norheim et al., 1998].

If $u(t)$ describes a continuous stationary function of time which has been demeaned, then the spectrum is given by the Fourier integral transform

$$P'(\omega) = \frac{1}{2\pi} \int_{-\infty}^{+\infty} R'(\tau) e^{-i\omega\tau} d\tau \tag{1.32}$$

where the prime denotes a continuous quantity, and

$$R'(\tau) = E[u(t)u(t+\tau)] \tag{1.33}$$

is the autocorrelation of $u(t)$, $\tau$ is a time lag, and $E[\,]$ is the expectation value, defined by

$$E[x(t)] = \lim_{T\to\infty} \frac{1}{T} \int_{-T/2}^{T/2} x(t)\, dt = \langle x(t) \rangle \,. \tag{1.34}$$

For a stationary process, the expectation value and ensemble average $\langle \ldots \rangle$ are equivalent.

Similarly, the *bi*spectrum is defined as

$$B'(\omega_1, \omega_2) = \frac{1}{4\pi^2} \int \int_{-\infty}^{+\infty} S'(\tau_1, \tau_2) e^{-i\omega_1\tau_1 - i\omega_2\tau_2} \, d\tau_1 \, d\tau_2 \tag{1.35}$$

where

$$S'(\tau_1, \tau_2) = E[u(t)u(t+\tau_1)u(t+\tau_2)] \, . \tag{1.36}$$

is a two–dimensional autocorrelation function with time lags $\tau_1$ and $\tau_2$.

The inverse relations for $R'(\tau)$ and $S'(\tau_1, \tau_2)$ are

$$R'(\tau) = \int_{-\infty}^{+\infty} P'(\omega) e^{i\omega\tau} \, d\omega \tag{1.37}$$

and

$$S'(\tau_1, \tau_2) = \int \int_{-\infty}^{+\infty} B'(\omega_1, \omega_2) e^{i\omega_1\tau_1 + i\omega_2\tau_2} \, d\omega_1 \, d\omega_2 \, . \tag{1.38}$$

By setting $\tau$ equal to zero in Equations 1.32 and 1.37,

$$R'(0) = E[u(t)^2] = \int_{-\infty}^{+\infty} P'(\omega) \, d\omega \tag{1.39}$$

and equivalently, from Equations 1.35 and 1.38,

$$S'(0,0) = E[u(t)^3] = \frac{1}{4\pi^2} \int \int_{-\infty}^{+\infty} B'(\omega_1, \omega_2) \, d\omega_1 \, d\omega_2 \, . \tag{1.40}$$

Examining Equations 1.39 and 1.40, it can be seen that where $P'$ gives the spectrum of energy ($u^2$), $B'$ gives the (bi)spectrum of $u^3$. By integrating the power spectrum, the variance of the time series is recovered (Parseval's theorem). Integration of the bispectrum gives the third moment of the time series.

The convolution operation in Equation 1.33 is symmetric about $\tau = 0$, and therefore

$$P'(\omega) = P'(-\omega) \, . \tag{1.41}$$

Similarly, for the bispectrum,

$$\begin{aligned} B'(\omega_1, \omega_2) &= B'(\omega_2, \omega_1) \\ &= B'(\omega_1, -\omega_1 - \omega_2) \\ &= B'(-\omega_1 - \omega_2, \omega_1) \\ &= B'(\omega_2, -\omega_1 - \omega_2) \\ &= B'(-\omega_1 - \omega_2, \omega_2) \, . \end{aligned} \tag{1.42}$$

This means that the spectrum is described by the values in the frequency range $0 \leq \omega \leq \infty$ and the bispectrum is defined by its value in the octant $0 \leq \omega_1 \leq \infty$, $0 \leq \omega_2 \leq \omega_1$.

In the case of a discretely sampled time series, the power spectrum is determined from complex Fourier coefficients $F(f_i)$ by,

$$P(f_i) = E[F(f_i)F^*(f_i)] \tag{1.43}$$

and the bispectrum is calculated from

$$B(f_1, f_2) = E[F(f_1)F(f_2)F^*(f_1 + f_2)] \tag{1.44}$$

where $^*$ denotes the complex conjugate. The upper frequency limit is then determined by the Nyquist frequency so that $P$ is defined in the interval $0 \leq f_i \leq f_N$ and $B$ within the triangle in the $(f_1, f_2)$ plane with vertices (0, 0), $(f_{N/2}, f_{N/2})$ and $(f_N, 0)$.

The spectrum given by Equation 1.32 is an unambiguous description of the time series if the frequency components are at random phases, i.e. the process described by the time series is Gaussian. If, for example, there is dynamically unrelated energy occurring at the frequency of a harmonic, this cannot be separated using the power spectrum. The bispectrum, however, can be used to identify energy at frequencies that are the sum or difference of other energy containing frequencies. If the process is truly Gaussian, $B' \rightarrow 0$.

A result of Equation 1.40 is that the skewness of a discrete time series can be determined from

$$S = \frac{\sum_i \sum_j \Re\{B(f_i, f_j)\}}{E[u^2]^{3/2}} \tag{1.45}$$

where $\Re\{\}$ denotes the real part, taking care in the summations to account for the calculation region, which generally includes part of one octant only. The other third moment quantity mentioned in Section 1.5 is the wave asymmetry. This can be calculated from the bispectrum by

$$A = \frac{\sum_i \sum_j \Im\{B(f_i, f_j)\}}{E[u^2]^{3/2}} \tag{1.46}$$

where $\Im\{\}$ denotes the imaginary part.

The bispectrum is a complex quantity and can be cast as biamplitude and biphase. In this instance, a more convenient measure of the coupling between frequencies is the normalized magnitude of the bispectrum, or bicoherence, given by

$$\beta(f_1, f_2) = \frac{|B(f_1, f_2)|}{(E[|F(f_1)F(f_2)|^2]E[|F(f_1 + f_2)|^2])^{1/2}} \tag{1.47}$$

which has values between zero and one [Kim and Powers, 1979]. For this normalization, the 95% confidence limit for zero bicoherence is $\sqrt{6/\text{degrees of freedom}}$ [Elgar and Guza, 1988]. The bicoherence is independent of wave amplitude.

There are differing opinions on which of several methods of bicoherence normalization is appropriate [Elgar and Guza, 1988; Henderson and Bowen, 2000]. The normalization to be used here is one of the more common found in the earlier literature, though it exhibits frequency resolution dependence. For the purposes of the analysis presented in Chapter 3, where the relative contributions by frequency pairs are considered (at the same resolution), this well characterized method suffices.

The results of the orbital velocity bispectral analysis presented in Chapter 3 are in the form of bicoherence and $\Re\{B\}$ colour contour plots in the ($f_1$, $f_2$) plane. Only one octant of the plane needs to be shown, since this is a complete description due to the symmetry relations (Equation 1.42). Significant peaks in bicoherence identify two frequencies of the three in an interacting triad contributing significant energy to the time series. In the case of a self–self (harmonic) interaction, two of the three frequencies are the same, which shows as a peak located on the $f_1 = f_2$ line. Significant bicoherence at frequency pairs in the ($f_1$, $f_2$) plane may indicate a sum or difference interaction, since the condition is only that the three frequencies involved satisfy $|f_3| = |f_1 \pm f_2|$. In general, peaks in bicoherence are usually accompanied by peaks in $|\Re\{B\}|$, but the converse is not necessarily true. $\Re\{B\}$ can have positive or negative values — a positive (negative) peak indicates an interaction between frequencies contributing positive (negative) skewness to the overall integrated skewness of the time series.

## 1.8 Organization of the Thesis

This thesis is presented in four chapters and an appendix. Following this introductory chapter, description is given in Chapter 2 of the laser–video system which was outlined conceptually in Section 1.3, with description of the camera calibration procedure, as well as operational details of the laboratory and field deployments. Observations obtained from the field deployment and results of their analysis are presented in Chapter 3. This includes presentation of ripple geometry and migration velocity measurements and analysis of the wave forcing with comparison to second–order and linear wave theories. The thesis is summarized in Chapter 4. Appendix A contains discussion of the mathematical formulation of the second–order wave theory results presented in Chapter 3. Appendix B contains expansion on the orbital velocity dependence of the observed ripple migration velocity.

# Chapter 2

# Experiment Design and Deployments

The following chapter describes the design of the laser–video imaging system, the video field–of–view calibration procedure, the bed profile finding algorithm and a test profile case, and the instrument configuration during two deployments: at the National Research Council (NRC) Wave Research Flume and in the field at Queensland Beach, Nova Scotia. Finally, a few sample images from the two deployments are presented, showing instantaneous two–dimensional structure in the suspended sediment field and the simultaneous bed profile.

## 2.1 Laser–video System Design and Specifications

The wet end of the laser–video system consists of two basic parts: the diode lasers, which provide the structured lighting, and the imaging camera. These components were selected for compact size, modest cabling and power requirements, and economy. A camera and two lasers (one without its pressure case) are shown in Figure 2.1. On the dry end, the data are recorded using standard S–VHS video equipment. The following section describes the wet end components in more detail.

The diode lasers operated in the visible red range at 685 nm wavelength (Power Technology Inc., PM series). Each laser was fitted with line–generating optics that produced a fan–shaped beam of light of about 70° by less than 1/2°. The optical power output of

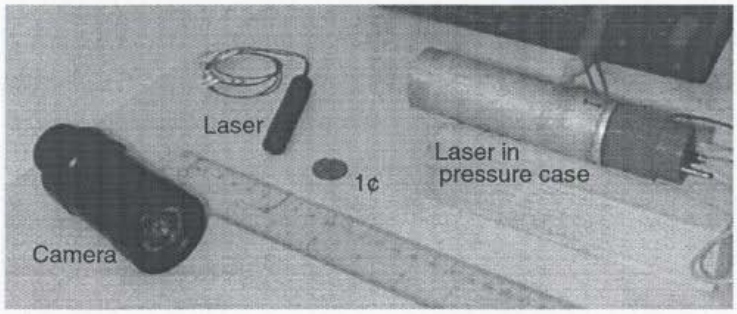


Figure 2.1: Photograph of the camera and two lasers, one with pressure case and one without. A penny is included for scale.

each of the two lasers used in the NRC experiment was 16.5 mW, and two additional lasers used at Queensland Beach, about 55 mW. Each was housed in a cylindrical pressure case approximately 3 cm in diameter by 10 cm long (pictured in Figure 2.1) with a glass window at one end. There was a thermal conductor (copper collar) between the diode laser and the inside of the pressure case, as diode laser lifetime can be limited by overheating. In deployment, pairs of lasers were mounted so that the light beams overlapped to extend the illuminated area. The light transmission length was short enough (less than 4 m at the longest) that the higher absorption coefficient for red light in water than, for example, blue–green light was not a limitation.

The laser illuminated section was imaged using a wide–angle, black–and–white underwater video camera (DeepSea Power and Light, Micro–SeaCam 1050). The camera housing is 5 cm in diameter by 10 cm long with a field of view of 77° (vertical) by 98° (horizontal). During the experiment at NRC, lights were turned off when video data were collected, and in the field, data collection was limited to twilight and nighttime hours. During the field deployment, the cameras were fitted with red filters to exclude some background light, but even with the filters, the laser light was not detectable against daytime light levels.

In retrospect, there are some considerations regarding the combination of laser wattage and sensitivity of the camera CCD array. At the time the system was designed, the highest

power diode lasers available in that model series were used. Subsequently, power outputs have increased. Higher laser wattage to obtain bed profiles during the day would require a secondary laser system for daytime use since the strongest light reflection from the bed during clear water nighttime operation sometimes saturated the CCD detector. In this case, a higher laser power output at night would not have been beneficial. In fact, the effect of light scattering from the sediment interface, making the bed profile line less distinct (discussed further in Section 2.3), was more evident in the case of the 55 mW lasers. In terms of imaging the suspended sediment, this saturation, if widespread enough across the CCD array, activates the automatic iris in the camera (a common self–defense feature in most solid–state cameras). This reduces the amount of light received potentially to the point where it is no longer possible to discriminate the much lower intensity illumination of the suspended sediment. More power is not necessarily a good thing for either bed profile or suspension imaging.

An asset of the laser–video system is its small independent parts that can be mounted among other instruments without interfering or adding significant bulk to the total instrument array. The diode laser cases and cameras were mounted using shaped PVC blocks, hose clamps and U–bolts (the instrument frames are described in Section 2.4). Each pair of lasers was powered with 5 VDC 120 mA and the camera, 15 VDC 110 mA, by single strands of a multi–element cable. A single RG58U coaxial element returned video data to shore. These constitute relatively modest power and cabling requirements.

## 2.2 Field of View Calibration

A necessary first step in extracting meaningful position data from video images is calibration of the field of view. The image must be corrected for wide–angle lens distortion and perspective, and a conversion factor applied to recover world coordinates from the pixel locations. The following section describes a procedure which was developed that follows a combination of the techniques described by Nomura et al. [1992] and Holland et al. [1997].

The camera geometry and coordinate systems are shown in Figure 2.2. The point $P$ has world coordinates $(x_w, y_w)$ in the object plane. In the absence of wide–angle lens distortion, this point would be projected onto the image plane at point $R_i$ with discrete pixel coordinates $(u_i, v_i)$. Radial distortion by the camera optics moves the projected point to $R_i'$ with pixel coordinates $(u_i', v_i')$, where the primed notation indicates the lens distortion. The object plane corresponds in position to the laser–illuminated section and the image plane, to the camera CCD array. The point at which the optical axis crosses the image plane, $(c_u, c_v)$, is the centre of radial lens distortion and does not in general coincide with the centre of the image plane. In the diagram, the object plane is shown approximately parallel to the image plane. In reality, this is not often the case. The three angles $\phi$, $\theta$ and $\psi$ define the pitch, yaw and roll of the object plane relative to the image plane. Pixel coordinates $(u_i', v_i')$ refer to the array position in the 720 × 480 digitized buffer recovered by frame grabbing, which differs from the actual size of the CCD array (537 × 505 elements). The origin in pixel coordinates in a grabbed image is in the upper left corner, corresponding to a world coordinate position in the negative $x_w$, positive $y_w$ quadrant (the camera electronically inverts the picture to a normal orientation).

World coordinates are extracted from pixel coordinates through the following three–step procedure. First, pixel coordinates are aligned with the optical centre $(c_u, c_v)$ and a scale factor applied to the $x$–coordinate.

$$\begin{aligned} x_i' &= (u_i' - c_u)d_x \\ y_i' &= c_v - v_i' \end{aligned} \tag{2.1}$$

The scale factor $d_x$ results from the mismatch between the aspect ratio of the frame buffer (4/3) and that of individual pixels. For example, for a frame buffer of size 640 × 480 pixels, $d_x$ equals 1. Second, a radial correction is applied to compensate for the wide–angle lens:

$$R_i = R_i' - \Delta R' \tag{2.2}$$

where

$$\Delta R' = \kappa_1 R_i'^3 + \kappa_2 R_i' \tag{2.3}$$

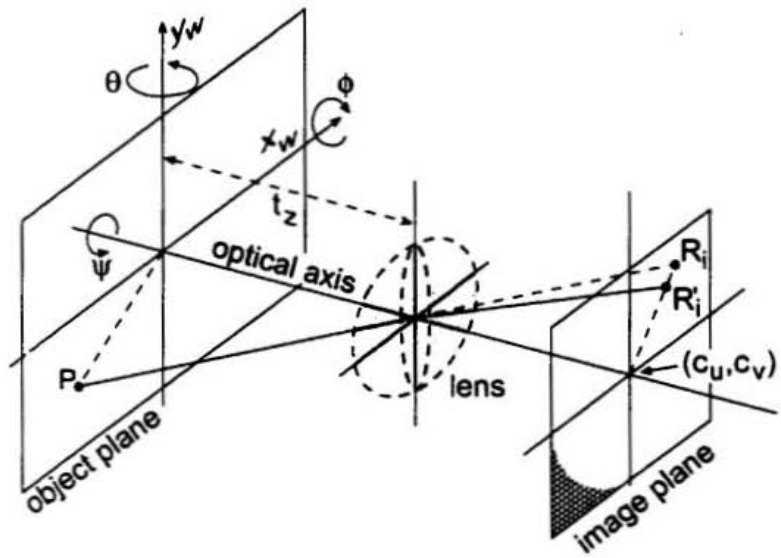


Figure 2.2: Camera calibration coordinate system definition. The point $P$, located in the object plane, is projected onto point $R'_i$ in the image plane. Radial distortion by the wide–angle lens is responsible for deflection of the projection from $R_i$ to $R'_i$.

and $R'_i = \sqrt{x_i'^2 + y_i'^2}$. Then,

$$\begin{aligned} x_i &= R_i \cos \alpha_i \\ y_i &= R_i \sin \alpha_i \end{aligned} \tag{2.4}$$

where

$$\alpha_i = \arctan \frac{y'_i}{x'_i} \tag{2.5}$$

and $\kappa_1$ and $\kappa_2$ are camera specific parameters discussed later in this section. Third, a thin–lens approximation is used in relating the undistorted frame buffer coordinates to world coordinates. The triangle including $R_i$, the optical centre $(c_u, c_v)$ and the point where the optical axis crosses the lens is geometrically similar to the triangle including that same point, $P$ and the projection of $P$ onto the optical axis, accounting for the pitch $\phi$, roll $\psi$

and yaw $\theta$ of the object plane. In matrix notation,

$$\frac{\begin{bmatrix} x_i \\ y_i \end{bmatrix}}{l} = \frac{\begin{bmatrix} r1 & r2 \\ r4 & r5 \end{bmatrix}\begin{bmatrix} x_w \\ y_w \end{bmatrix}}{\begin{bmatrix} r7 & r8 \end{bmatrix}\begin{bmatrix} x_w \\ y_w \end{bmatrix} + t_z} \tag{2.6}$$

where the rotation matrix coefficients are given by

$$\begin{bmatrix} r_1 & r_2 & r_3 \\ r_4 & r_5 & r_6 \\ r_7 & r_8 & r_9 \end{bmatrix} = \begin{bmatrix} \cos\psi\cos\theta & \cos\psi\sin\theta\sin\phi - \sin\psi\cos\phi & \cos\psi\sin\theta\cos\phi + \sin\psi\sin\phi \\ \sin\psi\cos\theta & \sin\psi\sin\theta\sin\phi + \cos\psi\cos\phi & \sin\psi\sin\theta\cos\phi - \cos\psi\sin\phi \\ -\sin\theta & \cos\theta\sin\phi & \cos\theta\cos\phi \end{bmatrix} \tag{2.7}$$

and $t_z$ is the distance along the optical axis between the lens and object plane. The variable $l$ represents the distance between the lens and the image plane in pixel units and is a fitted parameter. The matrix Equation 2.6 is solved for the world coordinates $x_w$ and $y_w$.

The quantities $c_u$, $c_v$, $\kappa_1$ and $\kappa_2$ were determined for each camera in the laboratory as follows. The reverse of the above procedure was applied to a least squares minimization of the difference between calculated and digitized grid point locations on a 55 cm by 50 cm grid (5 cm spacing, 132 points) placed at a known position relative to the camera, both submerged. Figure 2.3 shows the radial correction $\Delta R'$ (Equation 2.3) plotted against $R'_i$. The function $\Delta R'$ is shown as the solid line, and the symbols show the difference between digitized grid point locations and their world coordinates converted to pixel coordinates (calculated $R_i - R'_i$) for a laboratory calibration of camera 1. The difference between these plotted values and the function $\Delta R'$ is minimized to determine the camera parameters. The scatter in the plotted points, Figure 2.3b, shows that aside from a few outliers, the digitization error is less than the pixel resolution.

Subsequently, for each deployment, $l$ and the angles $\phi$ and $\theta$ were determined by a similar process after an on–site calibration using the same grid placed in the laser–illuminated plane. To reduce the number of minimization parameters, $\psi$ can be determined from the

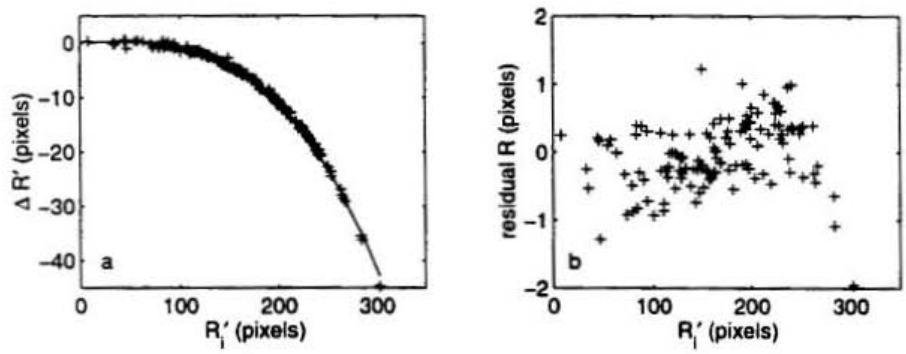


Figure 2.3: Camera lens radial correction factor as a function of uncorrected radius $R_i'$ for camera 1. (a) The solid line is the function $\Delta R'$ and the + symbols are the difference between uncorrected digitized grid point locations and 5 cm spaced world coordinate locations converted to pixel coordinates ($R - R'$) using the reverse of the calibration procedure. (b) Residual radial correction i.e. the scatter in the points plotted in (a).

Table 2.1: Laboratory determined calibration parameters for cameras used in the NRC and Queensland Beach experiments. $c_u$ and $c_v$ define the optical centre in the 720 by 480 pixel frame buffer. $d_x$ defines the pixel aspect ratio. $\kappa_1$ and $\kappa_2$ are radial lens distortion correction parameters.

| Cam. | $c_u$ (pxl) | $c_v$ (pxl) | $d_x$ | $\kappa_1$ | $\kappa_2$ |
|---|---|---|---|---|---|
| *# 1* | 320.1 | 237.8 | 0.889 | $-1.662\times10^{-6}$ | 0.0106 |
| *# 2* | 332.7 | 262.6 | 0.889 | $-1.620\times10^{-6}$ | 0.0173 |

mean bed slope if $\theta$ is small. Parameters determined for each of the two cameras used are shown in Tables 2.1 and 2.2.

Figure 2.4 illustrates an example of a captured frame used in the site–specific calibration procedure for the NRC experiment. Note the wide–angle lens distortion resulting in the "barrel" effect. The grid has been placed in the plane of the laser–illuminated section (the laser light sheet can be seen intersecting the investigator's thumb). The $\times$ symbols mark the digitized grid locations used in the minimization scheme to determine the site–specific camera calibration parameters. Other instruments labeled in the video image can

Table 2.2: Site–specific calibration parameters for the NRC and Queensland Beach (QB) experiments. $l$ is a fitted parameter, $t_z$ is the measured distance from the camera to the object plane and $\phi$, $\theta$ and $\psi$ define the pitch, yaw and roll of the object plane relative to the image plane.

| | Cam. | $l$ (pxl) | $t_z$ (cm) | $\phi$ | $\theta$ | $\psi$ |
|---|---|---|---|---|---|---|
| NRC | *# 1* | 479.4 | 66.6 | -18.7° | 0.2° | 0.0° |
| QB | *# 1* | 406.2 | 88.0 | -5.6° | -0.3° | -1.0° |
| | *# 2* | 449.0 | 94.3 | -12.8° | 9.9° | 6.9° |

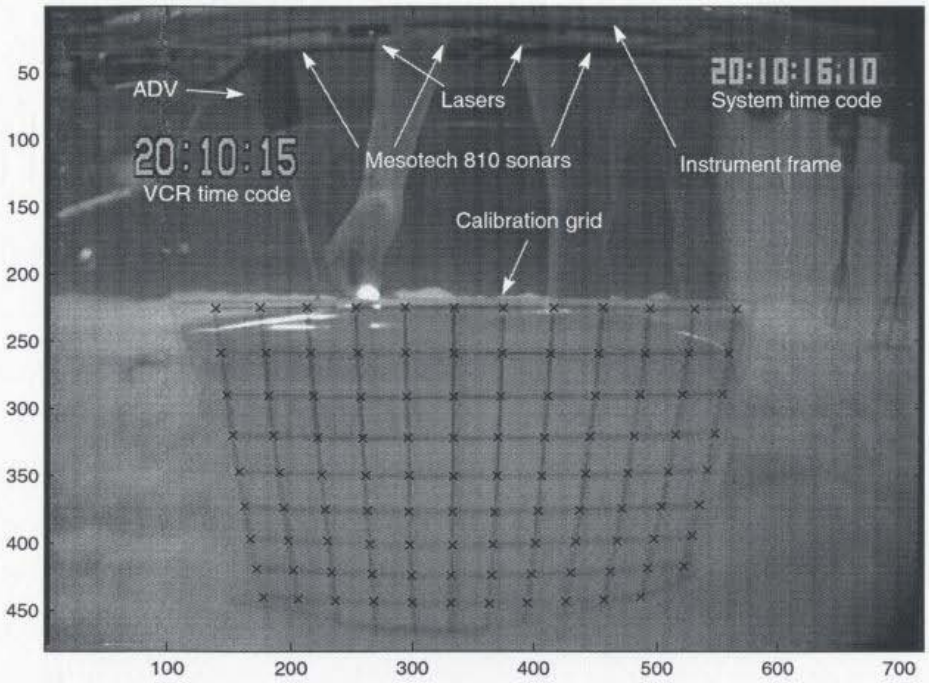


Figure 2.4: Sample video image used in the NRC experiment site–specific calibration. The image pixel coordinates, with the origin in the upper left, are shown on the axes. The $\times$ symbols show the digitized grid locations used in the fit for determining the site–specific camera calibration parameters.

be compared with later discussion of the NRC deployment (Section 2.4.1, Figure 2.6). For the Queensland Beach field site–specific calibration, a SCUBA diver positioned the grid in the illuminated plane.

The world coordinate size of a pixel in the grabbed video frame depends on the radial position of that pixel from the optical centre and the range to the camera. In the NRC experiment video data, the size of a pixel near the centre of the frame is 1.2 mm by 1.4 mm and a pixel in the lower left corner, farthest from the camera, is 2.7 mm by 3.6 mm. In images from the Queensland Beach experiment, where two cameras were used, for the offshore looking camera a centre pixel is 1.9 mm by 2.1 mm, and at the corner, 3.5 mm by 3.8 mm. For the alongshore looking camera, pixels are 1.5 mm by 2.2 mm at the centre and 3.2 mm by 4.0 mm in the corner. The world coordinate position is assigned at the centre of a pixel.

## 2.3 Bed Profile Finding

The algorithm for determining the position of the bed in the video images is based on the fact that it is the brightest object in view. Though the width of the incident laser beam on the bed was about 2 mm, scattering by grains on the sand surface led to broadening of the line seen in the video image. Sediment in motion on the bed increased this effect. The position of the bed in the images is determined by finding the middle of this wavy stripe by a simple method which will be described in this section, with results from a test case.

The image conditioning necessary for determination of the bottom profile was minimal. A one or two pixel horizontal wander in the position of the image in the grabbed frame buffer was occasionally found and corrected by locating the coordinates of the colons in the VCR time stamp (by 2-D correlation to a standard colon image) and shifting the image in the frame buffer array accordingly. The images were then masked to exclude the areas outside that surrounding the laser line, including leeway for large bedforms. For each column ($u_i'$) of the frame buffer array, the pixel $y$–coordinates of the log intensity values greater than 70% of the maximum value in that column were passed to the next step. If

there were 3 or more points fitting this criterion, these pixel–log intensity points were then interpolated onto a regular 1/10 pixel spaced grid using a cubic interpolation. The pixel position of the maximum value of the fitted log intensity curve, at sub–pixel resolution, was taken as the bed elevation ($v_i'$). After the intensity peak location in each column in the unmasked area of the frame buffer has been determined, world coordinates ($x_w$, $y_w$) of the bed profile are then determined from these ($u_i'$, $v_i'$) pixel coordinates by the method described in Section 2.2.

In conditions of good visibility, one frame can be sufficient to determine the bed profile. In cases where a significant amount of sediment is in suspension such that parts of the laser line are intermittently shadowed or obscured, the profile can be pieced together by combining the parts of consecutive images containing the strongest bottom signal. This technique can also extend the length of the usable profile when visibility is very poor.

The world coordinate calibration procedure and the bed profile finding algorithm were tested with a known bed geometry. An artificial rippled surface 90 cm long was made from plywood with triangular ripples ranging in trough–to–trough length from 10 to 20 cm and in height, from 1 to 5 cm. The profile was illuminated by a laser line and a grid calibration was performed. The video determined ripple dimensions are shown in Figures 2.5. The average deviation of the calculated dimensions (height and length) from the actual measurements is 2 mm for this test case.

The test case serves as a check on the calibration and bottom finding procedures with the following reservation. For each deployment, the site specific geometry and calibration determine the measurement resolution and potential for deviation from the true ripple profile. The test case was set up purposefully to be representative of the geometry of the deployments ($t_z$ about 1 m, $\phi$, $\psi$ and $\theta$ nonzero). Some of the deviation seen in the test case results is due to the calibration, some due to the profile finding, and some due to uncertainty in locating the ripple crests and troughs in the found profile. It is not possible from this type of test to determine the relative contribution by each of these sources of error. The consistently low estimates of ripple length and trend in height indicate a potential (small) error in determination of one of the angles (most likely $\theta$). In the laboratory and

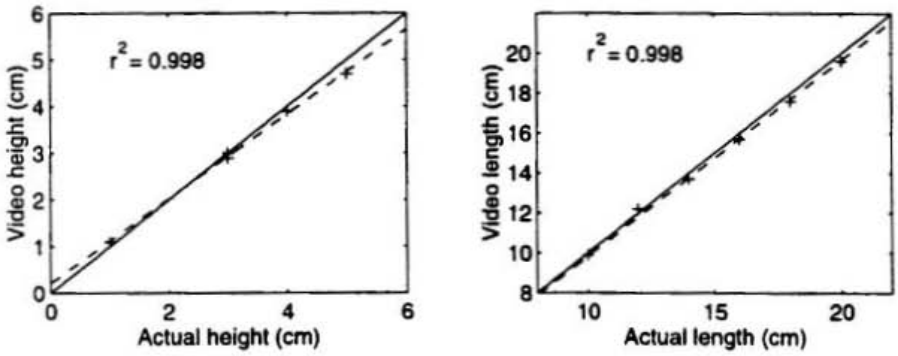


Figure 2.5: Bed profile finding algorithm test ripple results. a) Ripple height finding and b) ripple length finding. Solid lines show the one–to–one line and dashed lines are linear regressions, with $r^2$ values as given.

field data, based on the observed broadening of the illuminated laser line by scattering on the bed surface, it is estimated that in any particular observation the profile finding and peak and trough location uncertainties represent a larger potential for deviation than the calibration.

It should be noted that O(1 mm) horizontal and vertical resolution over a length of 1 m is very high in comparison to other bedform measurement techniques. As mentioned in Section 1.3, acoustic techniques can offer millimeter range resolution, but typically there is some degree of spatial averaging due to the finite size of the beampattern "foot print" (of the order of centimeters in size), determined by the beampattern divergence.

## 2.4 Deployments

The laser–video system was deployed twice in 1995 in collaborative experiments with Dalhousie University. The first laboratory experiment acted partly as a testing phase, though a quantity of good quality data was obtained. The subsequent field deployment took advantage of a few improvements to the system suggested by the laboratory experience. The following sections describe the deployment sites and the instrument configurations used in each instance.

### 2.4.1 National Research Council, Ottawa

The advantages of working in a controlled laboratory setting are particularly appreciated when testing new techniques or equipment. This section describes the experimental setup at the NRC Wave Research Flume where it was possible to easily access the equipment throughout the deployment (as evidenced by the presence of the investigator in the image in Figure 2.4), as well as offering complete control of the wave forcing environment.

The instruments were mounted on a 3 m section of antenna mast, triangular in cross-section, placed with one side as the base and fixed to cross–members bolted to the sides of the wave flume. A side view of the NRC experiment set–up is shown in Figure 2.6a, which can be compared with the video image shown in Figure 2.4. The NRC Wave Research Flume is 97 m long by 2 m wide by 3 m deep and was filled to a depth of 1.5 m during the experiment. The instruments were placed above a 10 m long, 10 cm deep, bed of sand ($D_{50}$ = 186 $\mu$m) located next to a viewing window approximately 2/3 of the way down the flume from the wave paddle. The laser beams were oriented vertically with the wide dimension parallel to the axis of the flume. The camera was located on a separate support member — its position is better shown in the plan view, Figure 2.6b. Other instruments deployed included three Mesotech 810 acoustic concentration profilers, a pair of Acoustic Doppler profilers [Zedel et al., 1996], a Sontek Acoustic Doppler Velocimeter (ADV), wide and narrowbeam scanning sonars [Hay and Wilson, 1994], capacitive wave gauges, and other current meters and video equipment belonging to collaborators from Dalhousie University. Laser–video data were synchronized with experiment time by including a system–wide time code in the frames using a Horita VG50 Time Code Generator.

Within the limits imposed by mechanics and shallow water wave theory, the NRC Wave Research Flume facility offered extensive control of the wave forcing. Waves were generated by a hydraulically actuated piston and absorbed by a 17 m long grid of metal mesh. Series of regular 3 and 3.5 second period waves of increasing height from 20 to 70 cm were run, as well as artificial "groups" (cosine tapered minute long regular wave trains), and JONSWAP spectrum runs at increasing significant wave heights (30 to 50 cm).

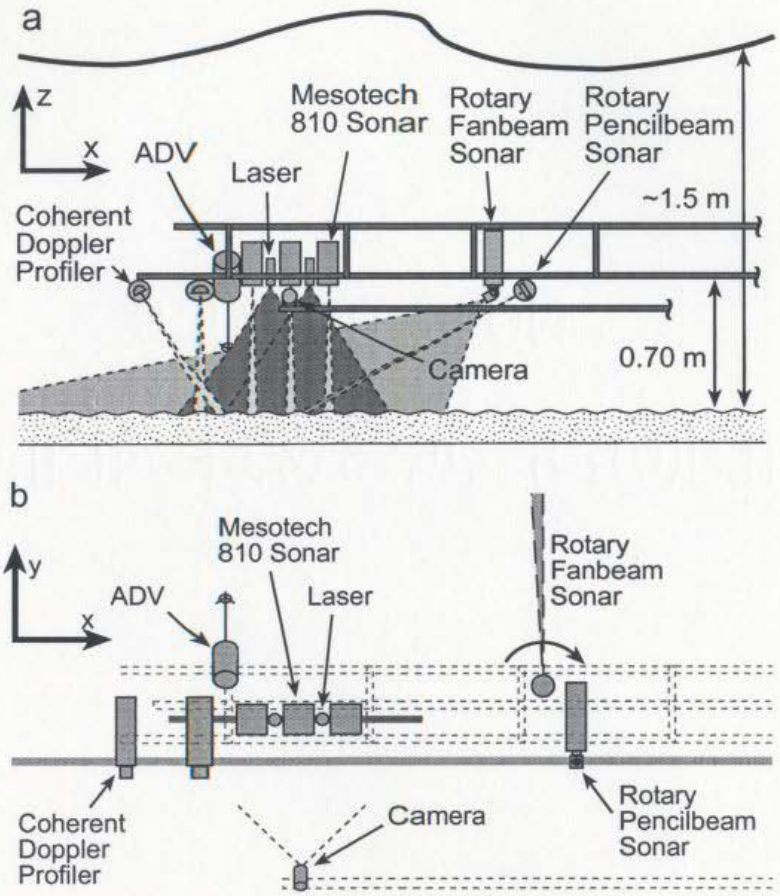


Figure 2.6: Instrument array configuration at NRC, Ottawa, in side (a), and plan (b) views.

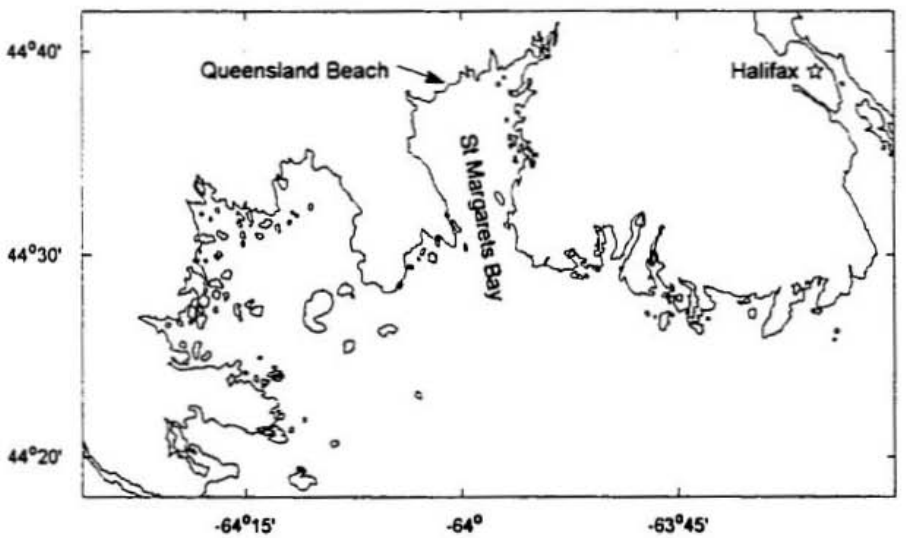


Figure 2.7: Map of south–central Nova Scotia showing St Margarets Bay and the Queensland Beach field site location in relation to Halifax. (Coastline downloaded from `http://crusty.er.usgs.gov/coast/getcoast.html`, World Vector Shoreline.)

### 2.4.2 Queensland Beach, Nova Scotia

In the fall of 1995, a joint field experiment was undertaken at Queensland Beach, Nova Scotia. This was also the site of a previous collaborative field experiment in 1987 [Vincent et al., 1991]. This section describes the site and details of the deployment there.

Queensland Beach is a pocket beach between rocky headlands and is oriented almost normal to wave energy coming in through the narrow mouth of St. Margarets Bay. The location of the beach opposite the mouth of the bay is indicated in Figures 2.7–2.9. The experiment $x$–axis, determined from surveyed instrument frame post positions, is oriented 12° west of true north, as shown in Figures 2.8 and 2.9. The dashed line in the figures is drawn perpendicular to the observed ripple crests, as discussed further in Chapter 3.

The mean beach profile from three surveys near the end of the 10 day deployment is shown in Figure 2.10. The instrument frame was located 60 m offshore of the mean water

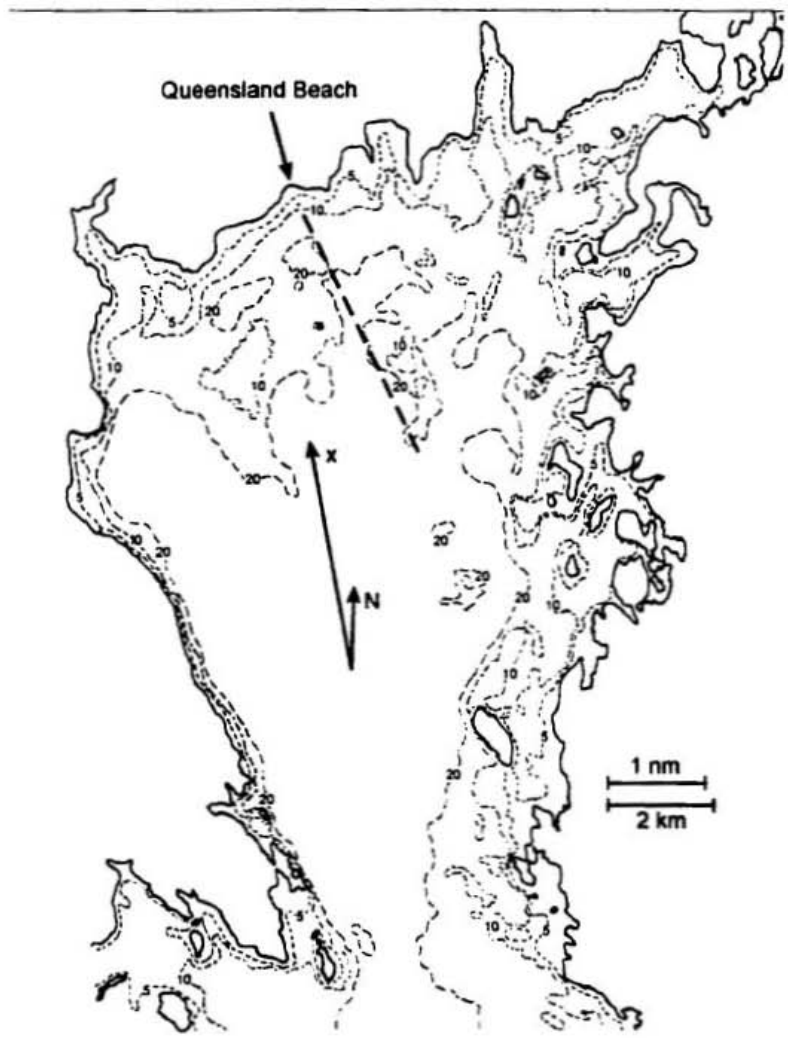


Figure 2.8: St Margarets Bay and the Queensland Beach field site. The 20, 10 and 5 fathom depth contours are shown. The experiment co–ordinate $x$–axis is shown, west of true North. The dashed line is perpendicular to the orientation of the ripple crests during the night of yearday 261, as determined from fanbeam sonar images. (Adapted from Canadian Hydrographic Service Chart #4386.)

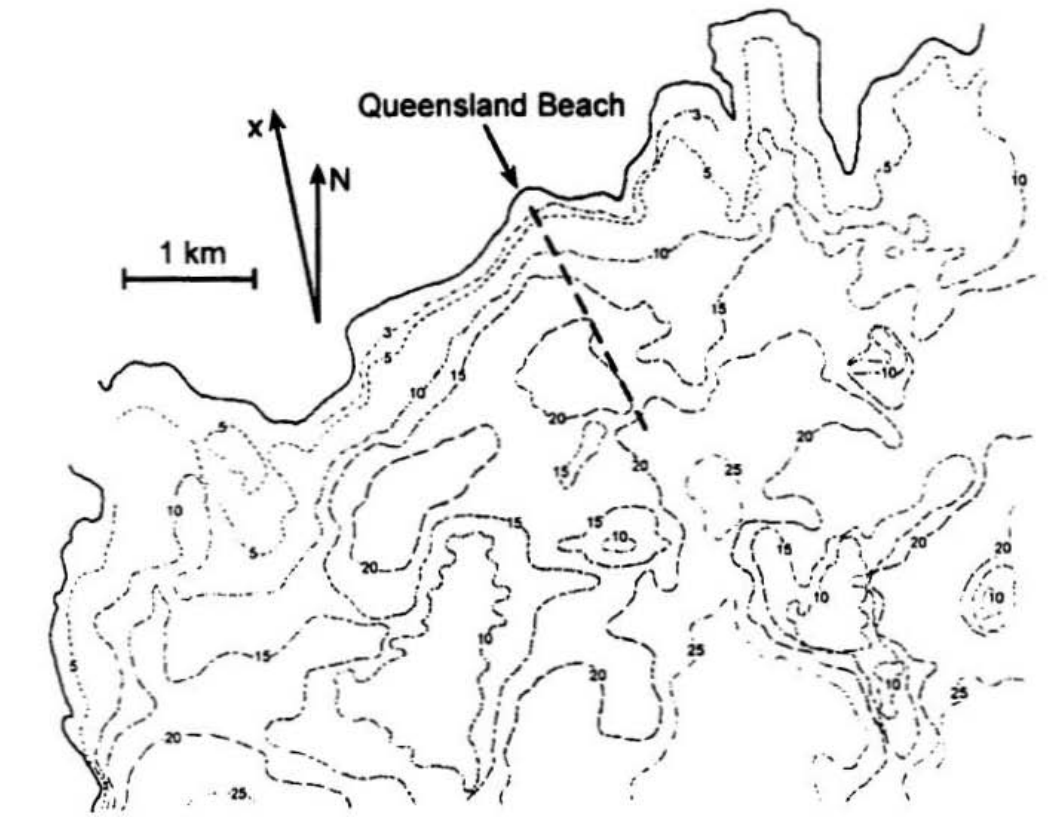


Figure 2.9: Detailed bathymetry of the area immediately surrounding Queensland Beach. The 25, 20, 15, 10, 5, and 3 fathom contours are labeled, as well as the experiment $x$–axis, and a perpendicular to the dominant ripple crest orientation on the night of yearday 261 (dashed line). (Adapted from Canadian Hydrographic Service Field Sheet #1595.)

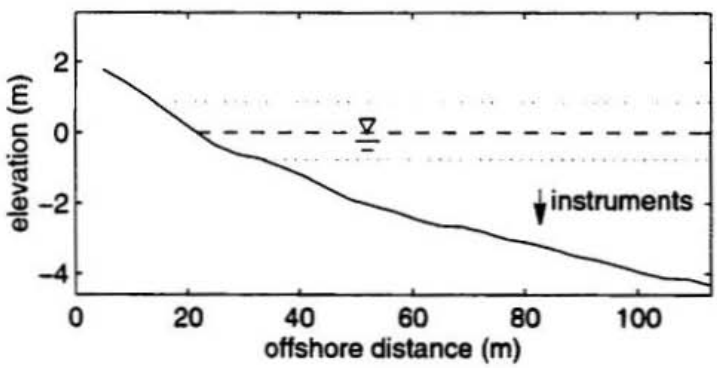


Figure 2.10: Mean beach profile at the time of deployment at Queensland Beach. The dashed line shows the mean water level and the dotted lines, the highest and lowest tides during the 10 day experiment.

line, where the mean water depth was 3.2 m, with maximum and minimum depths during the deployment of 4.1 and 2.4 m. The beach slope at that location was about 2°. Samples of the quartz sand collected at the site had a sieved median diameter of 175 $\mu$m.

The deployment configuration is shown in side and plan views in Figure 2.11. The instruments were mounted on a 3 m section of antenna mast cantilevered offshore from a rigid support frame (not shown in Figure 2.11). The legs of the support frame were jetted ~3 m into the sand bed, positioned in a 1.5 m by 2 m rectangle (long sides in the alongshore direction). The local bedform field was monitored to a radius of 5 m using a fanbeam rotary sidescan acoustic system [Hay and Wilson, 1994; Hay and Bowen, 2000]. A rotary pencilbeam acoustic system profiled bed elevation on a cross–shore line to a range of 5 m, as well as operating periodically at fixed slant angles (10° below horizontal in the offshore direction and vertically upward) with centimeter radial resolution [Hay and Bowen, 2000]. Flow measurements were made with a dual beam Coherent Doppler Profiler (CDP) system [Zedel and Hay, 1999]. Other instruments deployed include acoustic backscatter sonars, pressure sensors, optical backscatter sensors and electromagnetic current meters.

In this deployment, instead of being directed straight downward as they had been at NRC, the lasers were mounted obliquely to increase the horizontal extent of the laser light sheet. An alongshore laser line was added to the system with the aim of adding that

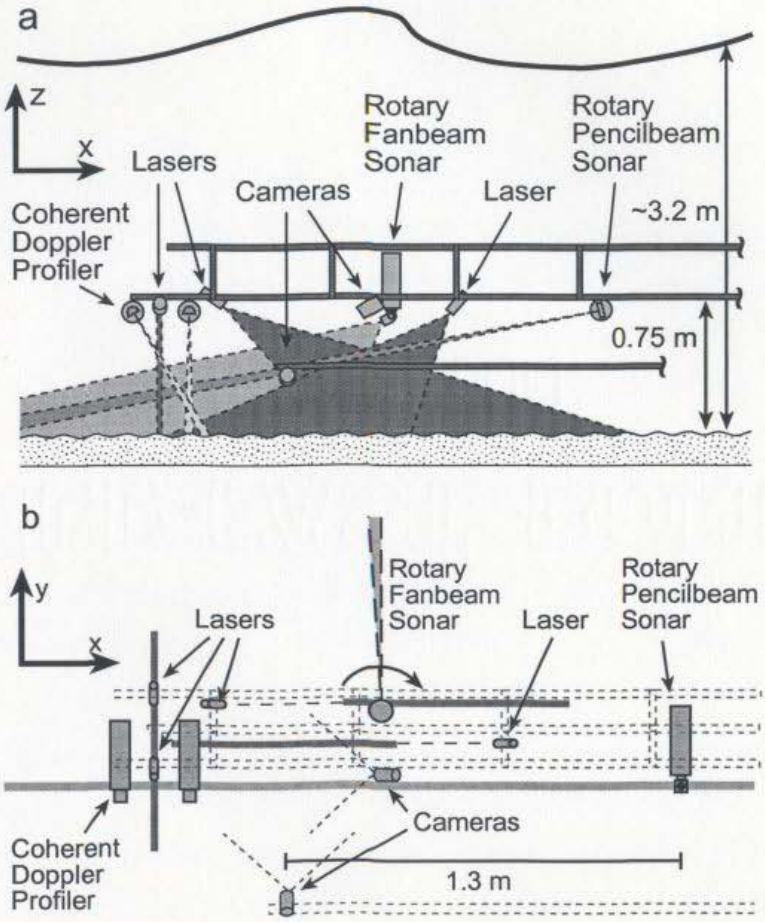


Figure 2.11: Side view (a) and plan view (b) of the instrument array configuration at Queensland Beach. In (b), the laser illuminated lines and the path that the pencilbeam followed along the bed are shown by the gray lines, and the frame outline is dashed. Experiment coordinates are shown with x positive onshore and z positive upward.

dimension to the observations of bedforms and suspension events (sample images from the offshore looking camera are presented in Section 2.6). As shown in Figure 2.11b, there were two shore–normal laser lines. The observations presented in Chapter 3 are from the single laser line closest to the alongshore looking camera.

## 2.5 Data Overview

A brief description of the various data types that have been used in this work is presented in this section. Since the results presented in Chapter 3 derive from the field observations, the following description will be oriented toward instruments relevant to that data set, though many of the same instruments were used in both deployments.

The acoustic data (pencilbeam and fanbeam sonars, CDP, etc.) were collected through a system of networked PC nodes which controlled data acquisition and storage, while maintaining a common time synchronization [Craig et al., 1995]. In the field, the acoustic systems operated on a half hour duty cycle through active wave conditions, and on a one hour cycle when wave energy was low. There were two approximately 8 minute CDP runs per half hour (sampling at a profile acquisition rate of ~30 Hz), one each of approximately 8 minute upward looking and slant pencilbeam runs (at a profile acquisition rate of ~8 Hz), one 5–scan rotary pencilbeam sonar run and one 5–scan rotary fanbeam run (360° rotation per scan). Some of these runs occurred simultaneously. All acoustic data were stored in a binary format as time–gated profiles of backscatter signal amplitude, converted to range–gated profiles using the speed of sound in sea water with 0.9 cm range resolution. The recovery of velocities from the raw CDP data is discussed in Zedel and Hay [1999]. In this work, only the velocity values at a point 20 cm above the bed in the CDP vertical velocity profiles have been used.

The laser–video system operated continuously during nighttime hours, from approximately 1900 to 0700 h local time. The video data were recorded in S–VHS format (400 horizontal lines per frame) at a time lapse rate equivalent to 6 hours per 120 minute tape (a frame rate of 10 Hz), or 12 hours per tape during very calm wave conditions (a frame

rate of 5 Hz). Frames were grabbed from tape for post–processing with a resolution of 720 by 480 pixels using a Digital Processing Systems Inc. Perception Video Recorder system. The post–processing and analysis (both of video images and acoustic data) were performed using Mathworks Matlab (versions 5.0 to 5.3) and the Image Processing Toolbox (version 2.1).

## 2.6 Sample Laser–Video Images

This section includes a few samples of the laser–video data from both the NRC and Queensland Beach experiments. These demonstrate the capabilities of the system for imaging the sediment in suspension and the bed profile.

The images shown in Figure 2.12 are typical examples from the NRC experiment video data recovered from tape with a basic level of post–processing. The images have been corrected for radial distortion and perspective, cropped to about 1/4 height, and are calibrated in centimeters. The gray scale has been reversed for better reproduction (in the raw data, the laser light is white against a black background).

These frames were recorded during a series of 3.5 second period monochromatic waves approximately 30 cm in height (recall the water depth was 1.5 m). The direction of wave travel is from left to right. The three images span 0.6 seconds immediately following the flow reversal. In the first image, the flow is static after the passage of a wave crest. In the second and third images, the flow is accelerating leftward under the following trough, shown by the $u$ velocity vector. The nearbed orbital velocity in the third frame is approximately 30 cm/s to the left, estimated from the motion of the suspended sediment cloud in the video footage.

The dominant feature in the images is the dark bed profile showing ripple features of varying lengths from approximately 10 to 20 cm. Overlayed in white is the bed profile line determined by the algorithm described in Section 2.3.

The suspension event associated with the ripple crest at the centre of the images is typical of events seen in lower energy conditions in both the wave flume and field data. This

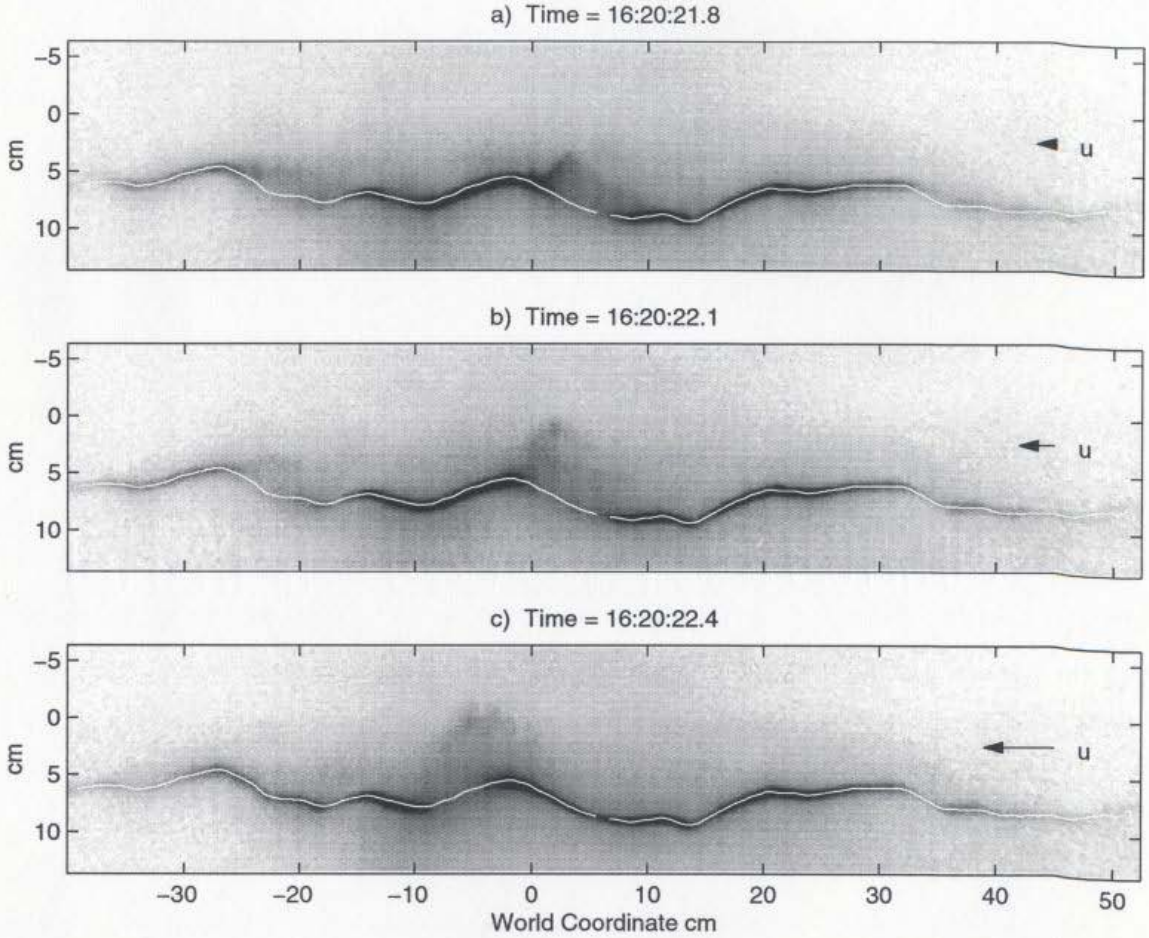


Figure 2.12: Three sample distortion–corrected images from the NRC experiment. The direction of wave travel is from left to right. The gray scale has been reversed. The three images are at 0.3 s intervals under 3.5 second regular waves, starting as flow is reversing to leftward, indicated by the velocity arrow labeled $u$. The white line shows the recovered bed profile. Axis units are world coordinate centimeters.

shows suspension of sand by flow interacting with the bedforms as described by Sleath [1982], and categorized as Bed Load–Suspended Load Intermediate mode transport using the Shibayama classification [Horikawa, 1988]. The vorticity of the sediment cloud (clockwise rotation persisting from its formation at the ripple crest during the preceding wave quarter period) is clearly visible in the video footage, though is not evident in the single frames. The range of intensity values included in the imaged suspended material is not large enough to infer concentration of sediment in suspension, however this information can be derived from the simultaneous acoustic backscatter data. It also appears that the acoustic devices can detect lower concentrations of suspended material than the laser–video system. Ultimately, the acoustic and video data can be combined.

An alongshore laser line and offshore–looking camera were added to the instrument array for the Queensland Beach deployment. Figure 2.13 shows a series of corrected images from that data set. As in Figure 2.12, the axes are in calibrated centimeters, the gray scale has been reversed and the images span a time of 0.6 s. The wave orbital velocity is directed away from the camera (offshore) during the decelerating half of the reverse flow phase. The video footage shows a small component of alongshore velocity directed toward the right (westward) during the time when these data were recorded. The lower background gray level in these images compared to those in Figure 2.12 is due to the lower level of ambient light.

The bed profile shown in white in the three frames was determined from a frame later in the same wave period when suspended material was not obscuring the bottom reflection, as it is in the first image. The bedforms at the time these images were recorded (determined from fanbeam scanning sonar images collected shortly before and after) were well–formed short–crested irregular ripples. The simultaneous cross–shore profile shows ripple lengths between 15 and 20 cm and heights of 1 to 2 cm.

The larger of the two suspension events pictured shows interesting structure. Its alongshore dimension is approximately 10 cm: this represents the first quantified field observation of the alongshore length scale of a sediment suspension event. The video footage shows clockwise rotation of the cloud of sediment as it is being carried offshore from its

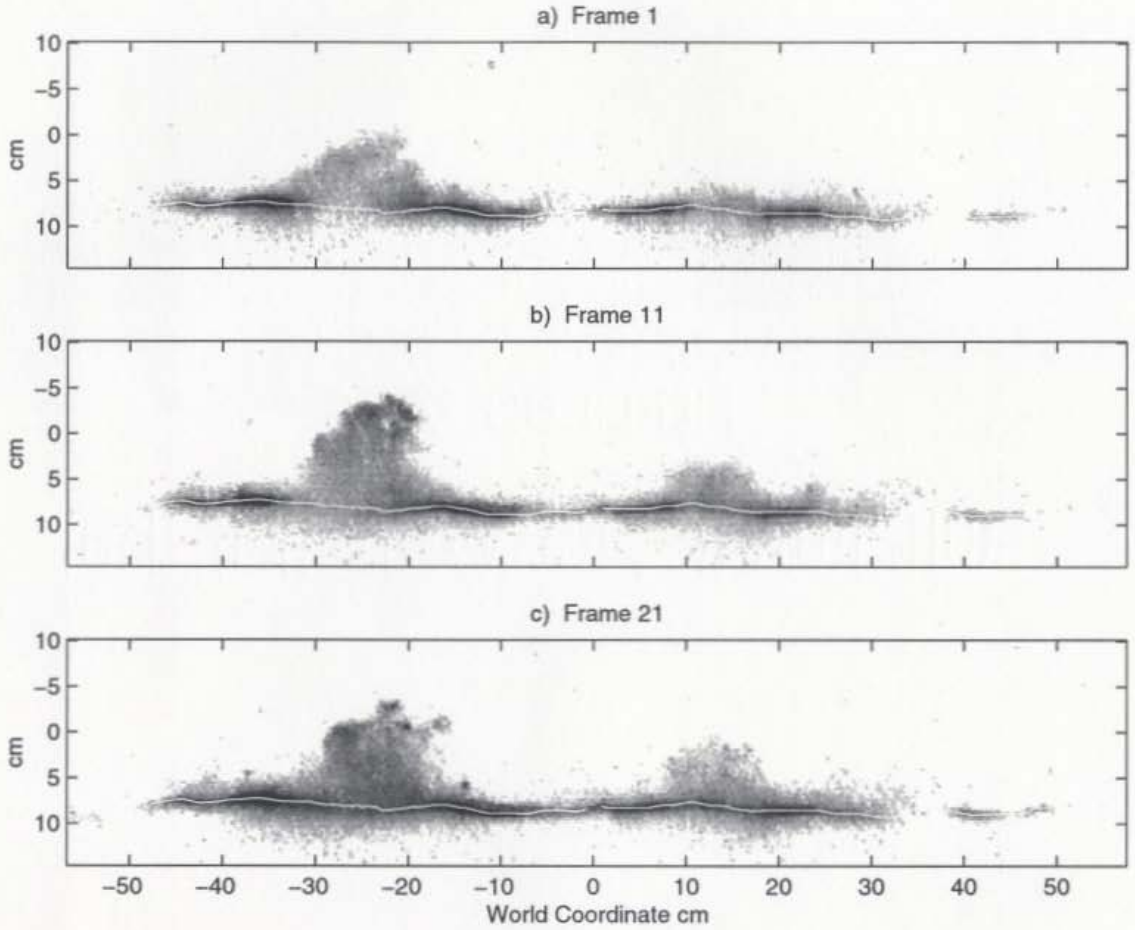


Figure 2.13: Three sample distortion–corrected images from the Queensland Beach field experiment. The camera is looking in the offshore direction. The gray scale has been reversed. The three images span 0.6 seconds while flow is decelerating, directed away from the camera (offshore). The white line shows the bed profile. Axis units are world coordinate centimeters.

point of origin, located onshore of the illuminated plane. The cross–shore extent of this cloud could be inferred by stacking successive images as it passes the illuminated section with the wave orbital velocity for comparison with the cross–shore scales determined from the orthogonal view.

These samples are taken from data collected while visibility conditions were optimal. Obviously, visibility in the field is highly variable. Of ten operational nights at Queensland Beach, visibility could be considered good to fair more than half of the time (limited most commonly by the presence of clouds of weed fragments). This was combined with favorable wave conditions (Shields parameter greater than 0.2) for portions of only two nights, giving in total, about 6 hours of laser–video data during other than quiescent conditions. The laser–video observations presented in Chapter 3 were collected during a 1.5 hour period on the first of those two nights.

# Chapter 3

# Results

The following chapter describes work based on field observations which were made during the Queensland Beach experiment. The emphasis is on a one–day storm event occurring on September 18 (yearday 261), 1995. A summary of the relevant wave conditions is given first, followed by presentation of ripple geometry and migration observations. It is shown that the observed linear transition ripples were anorbital type ripples and migrated offshore during the growth phase of the storm and onshore during storm decay. Further, it is shown that the observed rippie migration was correlated with the skewness of the nearbed orbital velocity. The orbital velocity forcing is then examined, in part using bispectral analysis. It is shown that the observed velocity skewness arises through nonlinear interaction between frequency components of the wave field. The observed orbital velocity forcing is shown to be comparable to predictions based on second–order, nonlinear wave interaction theory.

## 3.1 Overview of Wave Forcing Conditions, Yearday 261

This section describes the conditions through the storm event on yearday 261 which provided the wave forcing environment for the bedform observations reported later in this Chapter.

A summary of the storm history is given in Figure 3.1. The storm waves gained amplitude starting early in the day, peaking in significant wave height at about 8:00 GMT and

had subsided by 18:00 GMT (local time differed from GMT by $-3$ hours and all times are given in GMT from this point forward). The significant wave height $H_{1/3}$ and peak wave period $T_\zeta$ are shown in Figure 3.1a. Both were calculated from surface elevation ($\zeta$) time series extracted from upward looking pencilbeam sonar data — the significant wave height is four times the standard deviation of $\zeta$ [Thornton and Guza, 1983] and $T_\zeta$ is the surface elevation power spectral peak period. Figure 3.1b shows the dimensionless shear stress (grain roughness Shields parameter), given by

$$\theta_{2.5} = \frac{1}{2} f_w \frac{(a_o\omega)^2}{(s-1)gD}, \tag{3.1}$$

where

$$f_w = \exp\left(5.213\left[\frac{2.5D}{a_o}\right]^{0.194} - 5.977\right), \tag{3.2}$$

$D$ is the median grain diameter, $a_o = u_{\rm rms}T_p/\pi$ is the significant orbital semi–excursion, $T_p$ is the wave orbital velocity spectrum peak period, $\omega = 2\pi/T_p$ is the wave radian frequency, $s$ is the sediment specific gravity (2.65 for quartz) and $g$ is acceleration due to gravity. $f_w$ is the wave friction factor for rough turbulent oscillatory flow over a flat bed of fixed grains, as discussed previously in Section 1.6. The wave orbital velocity $u$ is determined from the demeaned 8–minute CDP records at of 20 cm height above the bed, and is positive onshore. Figure 3.1c shows the time history of the ripple types that were present in the local area as observed from the half hourly fanbeam sonar images [Hay et al., 1999]. The ripple types have been categorized as "I" for irregular, "X" for cross, "L" for linear transition, and "F" for flatbed.

The relevant features of this storm event were an initial growth of significant wave height, accompanied by a shift to longer peak wave period, and evolution of bedform type from irregular through cross and linear transition ripples to flatbed when wave height was maximal. This was followed by a decay in wave height and evolution of bedform type through cross and linear transition ripples back to irregular ripples. The time series of ripple type shows that two forms of ripples were often present at the same time. A lag is apparent in the progression of ripple types during the waning stages of the storm relative

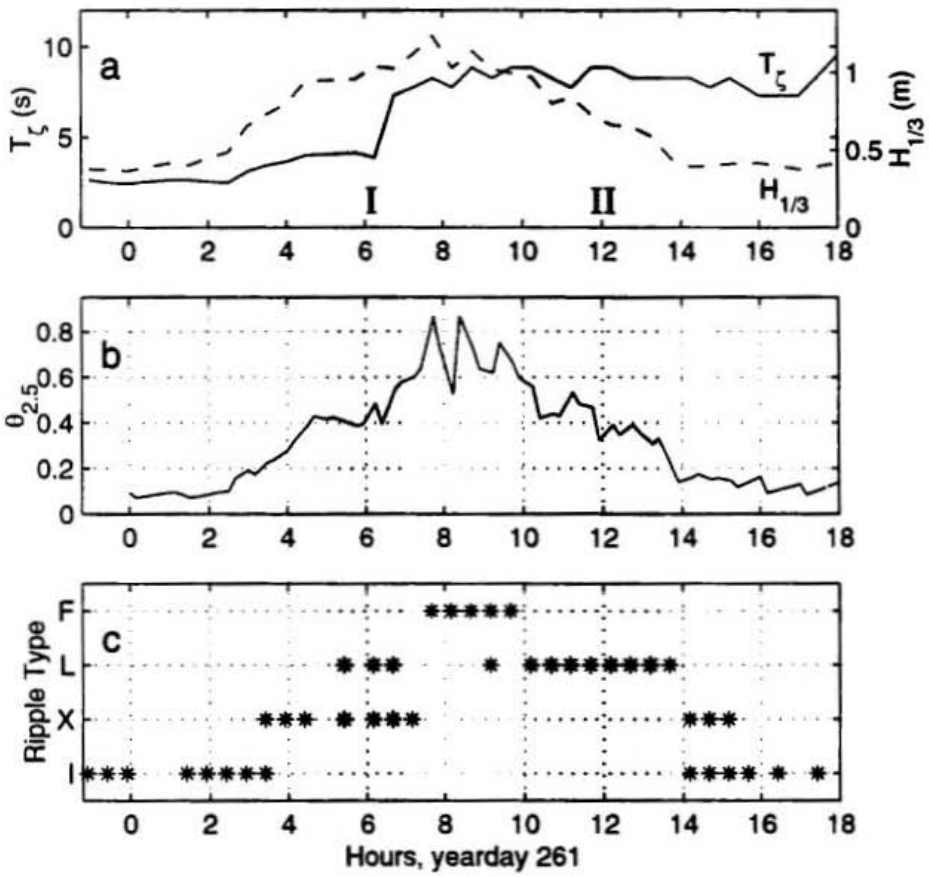


Figure 3.1: Time evolution of the storm event on yearday 261, 1995 (time in hours GMT). (a) The period of the surface elevation spectra peaks $T_\zeta$ (solid) and significant wave height $H_{1/3}$ (dashed); (b) dimensionless shear stress (grain roughness Shields parameter); (c) the ripple type present as observed from the fanbeam sonar images: I = irregular, X = cross, L = linear transition, F = flatbed. Intervals I and II are shaded gray (see text).

to the peak and decay in the wave forcing, which has also been observed elsewhere [Hay and Wilson, 1994].

Two time periods have been shaded gray in Figure 3.1 and have been labeled Intervals I and II for convenient reference. Transition ripples were present throughout both intervals for Shields parameter values between 0.3 and 0.5. Interval I falls during the growth phase of the storm event in the period before flatbed and Interval II is during the decay of the storm after flatbed. Two instances where linear transition ripples have been identified but have not been included in Intervals I or II were while the waves were near the peak height and near the end of the storm at low Shields parameter when the ripples may be considered relict.

As waves shoal, the orbital velocity skewness increases as the waves become more peaked in profile. When the wave subsequently breaks, the skewness decreases sharply [Elgar and Guza, 1985b]. Simultaneously during shoaling, wave asymmetry evolves from close to zero in deep water toward large negative values. Inside the breaker zone, the dynamics of the flow are significantly more complex than outside, particularly in the behaviour of these higher–order quantities. Table 3.1 lists the observed percentage of breaking counted from the upward looking pencilbeam sonar records, along with the water depth $h$, peak surface elevation spectral period $T_\zeta$ and significant wave height $H_{1/3}$. The wave breaking height $H_b$ was calculated from $0.56H_o(L_o/H_o)^{0.2}$, where $L_o = gT_\zeta^2/2\pi$ and $H_o$ is the deep water significant wave height calculated from $H_{1/3}$ [Fredsøe and Deigaard, 1992]. $H_b$ represents the height that the largest waves required for breaking in the local water depth. Also shown is Thornton and Guza's [1983] breaking wave percentage $A_b$, given by

$$A_b = \left(\frac{H_{rms}}{\gamma h}\right)^4 \tag{3.3}$$

where $\gamma$ is 0.44 and $H_{rms} = H_{1/3}/\sqrt{2}$ [Thornton and Guza, 1989].

To interpret the values presented in Table 3.1, consider that if the significant wave height, $H_{1/3}$, was equal to the wave breaking height, $H_b$, then the percentage of waves observed to be breaking should be approximately 33%. The observed percentage of waves

Table 3.1: Wave breaking observations from upward looking pencilbeam sonar records. $h$ is the water depth, $T_\zeta$ is the surface elevation spectral peak period and $H_{1/3} = 4\zeta_{rms}$ is the significant wave height. $H_b$, wave breaking height, is calculated from $H_{1/3}$. $A_b$ is the percentage of waves breaking calculated using Equation 3.3.

| time (GMT) | $h$ (m) | $T_\zeta$ (s) | $H_{1/3}$ (m) | $H_b$ (m) | $A_b$ (%) | obs. % |
|---|---|---|---|---|---|---|
| Interval I | | | | | | |
| 5:45 | 3.8 | 4.1 | 0.96 | 1.1 | 3 | 8 |
| 6:15 | 3.9 | 3.9 | 1.0 | 1.1 | 3 | 11 |
| 6:45 | 3.8 | 7.3 | 1.0 | 1.4 | 4 | 13 |
| Interval II | | | | | | |
| 10:15 | 3.4 | 8.9 | 0.97 | 1.2 | 5 | 23 |
| 10:45 | 3.2 | 8.3 | 0.80 | 1.1 | 3 | 0 |
| 11:15 | 3.1 | 7.7 | 0.84 | 1.2 | 4 | 0 |
| 11:45 | 3.1 | 8.9 | 0.73 | 1.1 | 2 | 0 |
| 12:15 | 3.0 | 8.9 | 0.66 | 1.0 | 2 | 0 |
| 12:45 | 2.9 | 8.3 | 0.65 | 0.9 | 2 | 0 |
| 13:15 | 2.9 | 8.3 | 0.59 | 0.8 | 1 | 1 |

breaking was always less than this value, consistent with $H_{1/3}$ being consistently less than $H_b$. During Interval I, some wave breaking was observed (about 10 %). Analysis to be presented in Section 3.4 shows that during Interval I, the wave spectra were bimodal with short period sea and long period swell peaks. In this case, significant wave height (calculated from surface elevation variance) is ill–defined. In instances where the sea and swell waves interfere constructively, for example, larger waves than either the swell or sea result. During Interval II, with the exception of the 10:15 GMT run, no waves were breaking. The upward looking pencil beam record at 10:15 GMT contains a few very large breaking events which injected bubbles deep into the water column, persisting for many wave periods and making identification of subsequent breaking events uncertain. The predicted percentage $A_b$ does not compare well with the observations, being low during Interval I and high during Interval II. This is consistent with the similar poor comparison between $A_b$ and observed wave breaking reported by Lippmann et al. [1996]. The wave

breaking behaviour may have been modified by wind. The beach log notes moderate–to–strong winds backing from south to easterly over that day. The observed overall low percentage of waves breaking, however, shows that the measurement area is indeed outside the breaker zone, so that wave breaking is not a consideration.

## 3.2 Linear Transition Ripple Geometry

In this section, observations of linear transition ripples are presented which were obtained using three independent instruments; the fanbeam and pencilbeam sonars and the laser–video bed profiling system. The fanbeam sonar gave an overview of the bedform field in the area surrounding the site of the instrument frame, showing the degree of three–dimensionality, spatial extent and orientation of the bedforms. The laser–video system gave local high–resolution bed profiles allowing detailed measurement of bedform geometry and migration. The pencilbeam sonar profiles provided verification of the ripple migration and wavelength observations made during the growth phase of the storm, as well as measurements during the decay phase of the storm when daylight prevented use of the laser–video system.

Figure 3.2 shows samples from two fanbeam sonar images collected at 6:10 and 11:10 GMT, during Intervals I and II respectively. Each is a plan view of the bedform field in a 4 m longshore × 2 m cross–shore area on the offshore side of the instrument frame. Linear transition ripples are evident in both images as long–crested, short O(10 cm) wavelength features. It is possible to follow a single ripple crest across the entire 4 m extent of the lower image. Bifurcations were present along some of the ripple crests. The upper image, from Interval I, shows that linear transition ripples coexisted with longer wavelength cross ripples (see Figure 3.1c). The orientation of the transition ripple crests was inclined at about 15° to the $y$–axis of the experiment coordinate system, as shown in the maps, Figures 2.8 and 2.9. These images show that the transition ripple wavelength and crest length were similar during both the growth and decay phases of the storm.

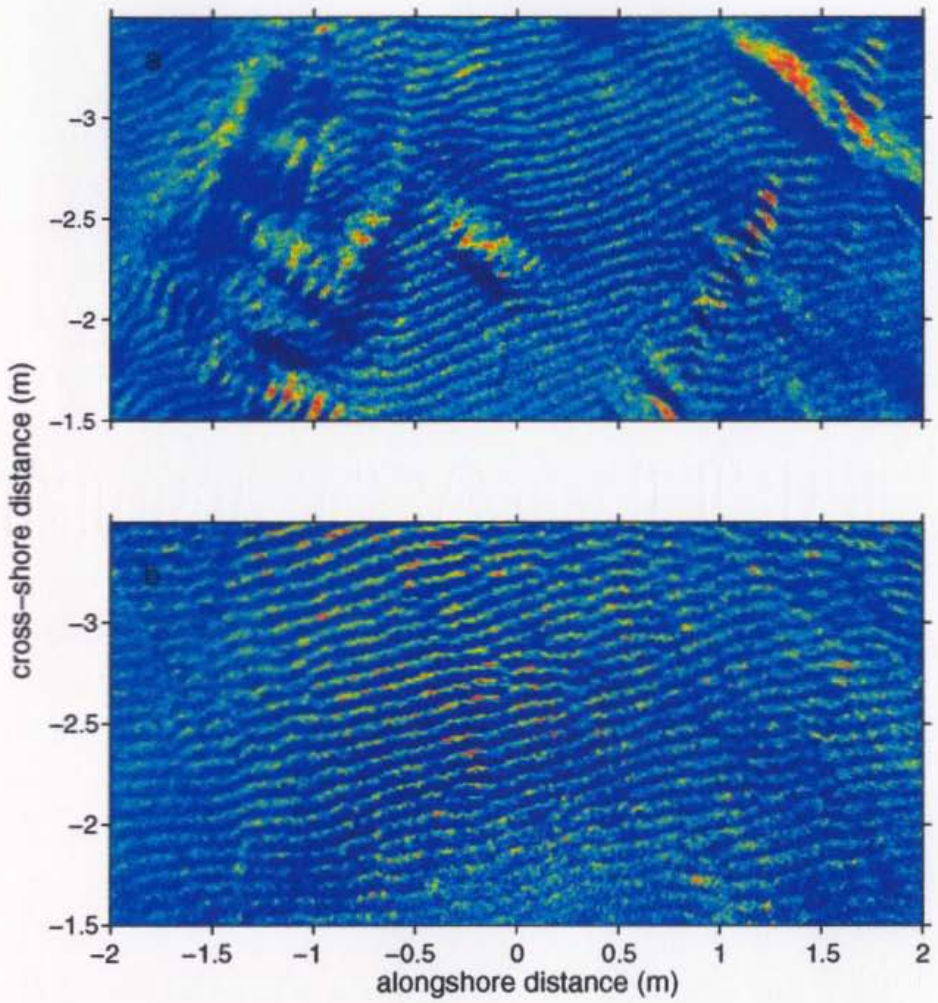


Figure 3.2: Fanbeam scanning sonar images of linear transition ripples collected at 6:10 GMT during Interval I (top), and 11:10 GMT during Interval II (bottom). Offshore is toward the top of the images and distance is measured along the bed from the instrument.

Figures 3.3 and 3.4 both show time series of bed profiles over a 90–minute time interval, 5:00 to 6:30 GMT during Interval I, obtained using the laser–video system. The bed profiles were extracted from the raw video data as described in Section 2.3. In Figure 3.3, each profile is an average of 40 raw profiles from images grabbed from tape at 2 Hz. Figure 3.4 shows a stack of further averaged profiles (5 of the profiles in Figure 3.3 are averaged for each profile in Figure 3.4). The mean bed slope of about 2° (see Figure 2.10) has been removed. Dropouts in the laser–video bed profile data are due to the laser light reflected from the bed being obscured by material in suspension. This happened more frequently at the ends of the laser beam pattern where the light intensity was lower. The laser–video system was much more sensitive to turbidity than the acoustic sensors. At the end of this time series, prior to the transition to flatbed, the light signal from the bed was obscured entirely.

The linear transition ripples shown in Figures 3.3 and 3.4 are seen to migrate offshore throughout the duration of this time series. These ripples were not "ephemeral" — in fact, the bedform coming into view at the beginning of the time series persists for the entire record, long enough to migrate across the entire field of view. This is confirmed by the raw video footage, which shows the largest waves driving sheet–like flow which undulates over the low relief bedforms without planing off the ripple crests.

Detailed analysis of the geometry of these bedforms is made possible by the high spatial resolution of the laser–video bed profiles. Figure 3.5 shows the time evolution of the ripple wavelength $\lambda_r$ and height $\eta_r$ through the 1.5 hours shown in Figure 3.3. The skewness $S_r$ and asymmetry $A_r$ of the ripple profiles are also shown. For these calculations, the central 40 cm of each 20–second averaged profile was interpolated onto a regularly spaced horizontal axis (profiles containing drop–outs in this region were not included). Wavelength was found from the spatial lag corresponding to the first nonzero autocorrelation peak, and height from $2\sqrt{2}$ times the root mean square bed elevation. Ripple profile skewness and asymmetry (using the Hilbert transform method, see Section 1.5) were also calculated from the interpolated profiles. The time series of ripple statistics were broken into 8–minute time bins and averaged.

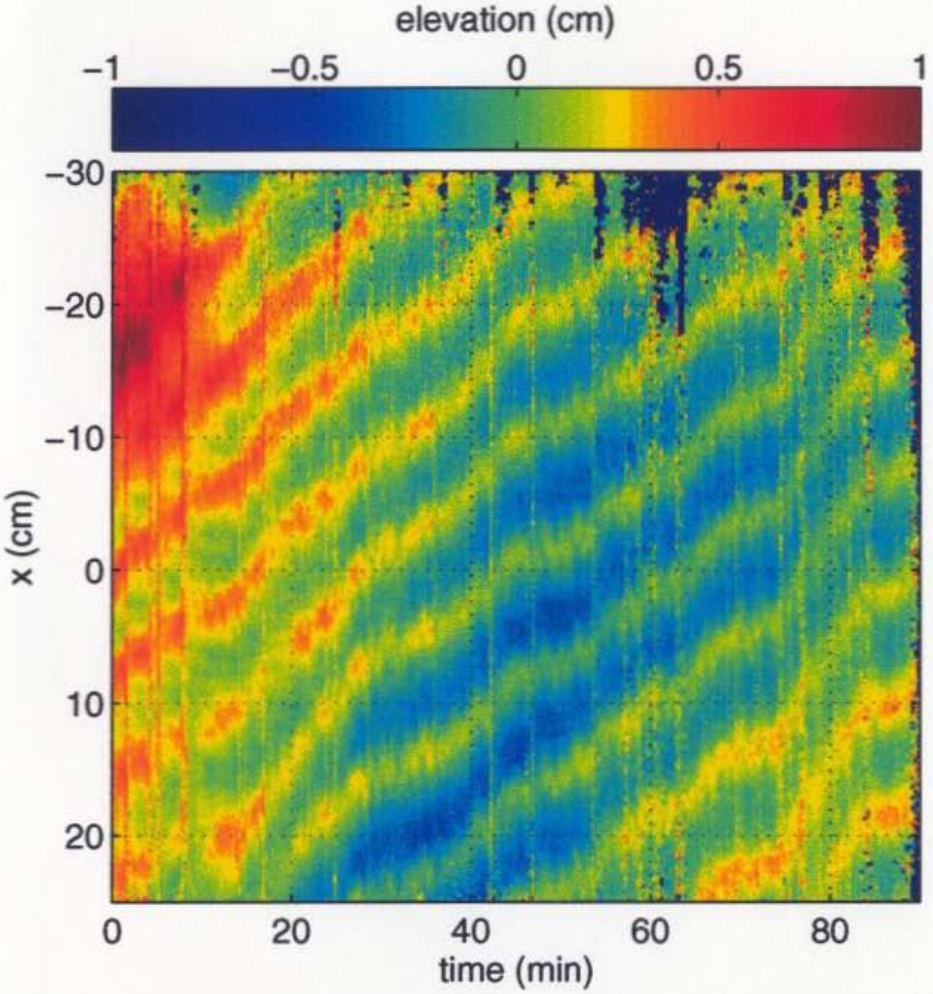


Figure 3.3: One and a half hour time series of bed elevation profiles obtained using the laser–video system during Interval I, starting at 5:00 GMT. The colour scale denotes elevation and offshore is toward the top. The laser–video profile origin is located approximately 25 cm seaward of the fanbeam origin.

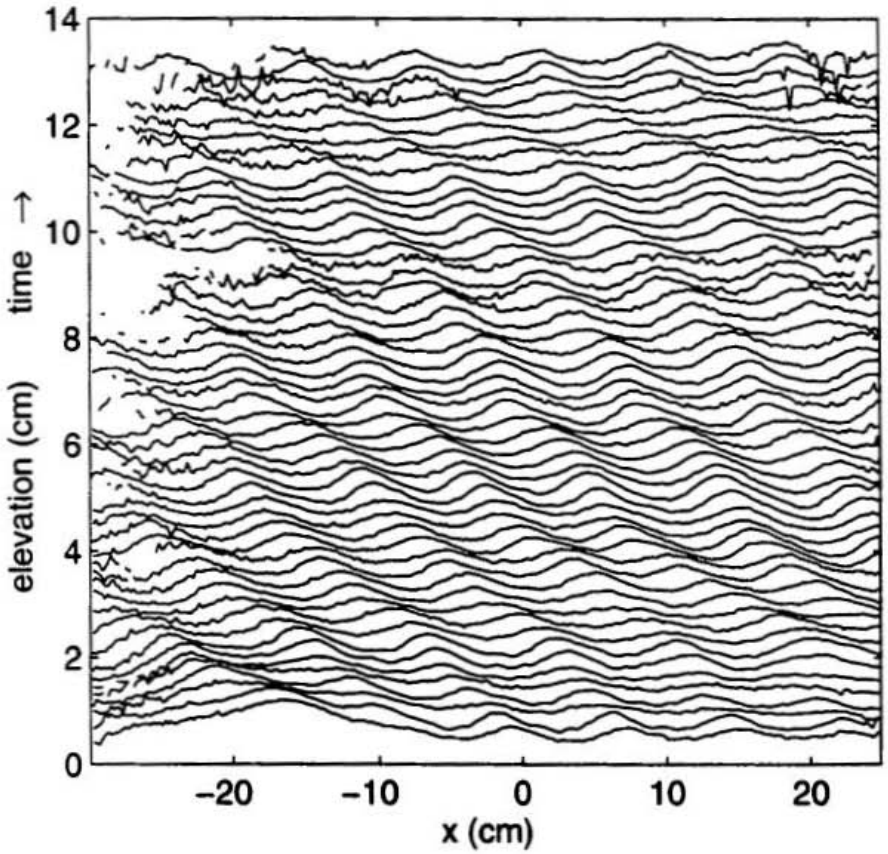


Figure 3.4: Further averaged bed elevation profiles obtained using the laser–video system during Interval I. Shown are 5–profile averages of the same time series as in Figure 3.3, offset by 0.25 cm each, with time progressing from bottom to top. $x$ is positive onshore.

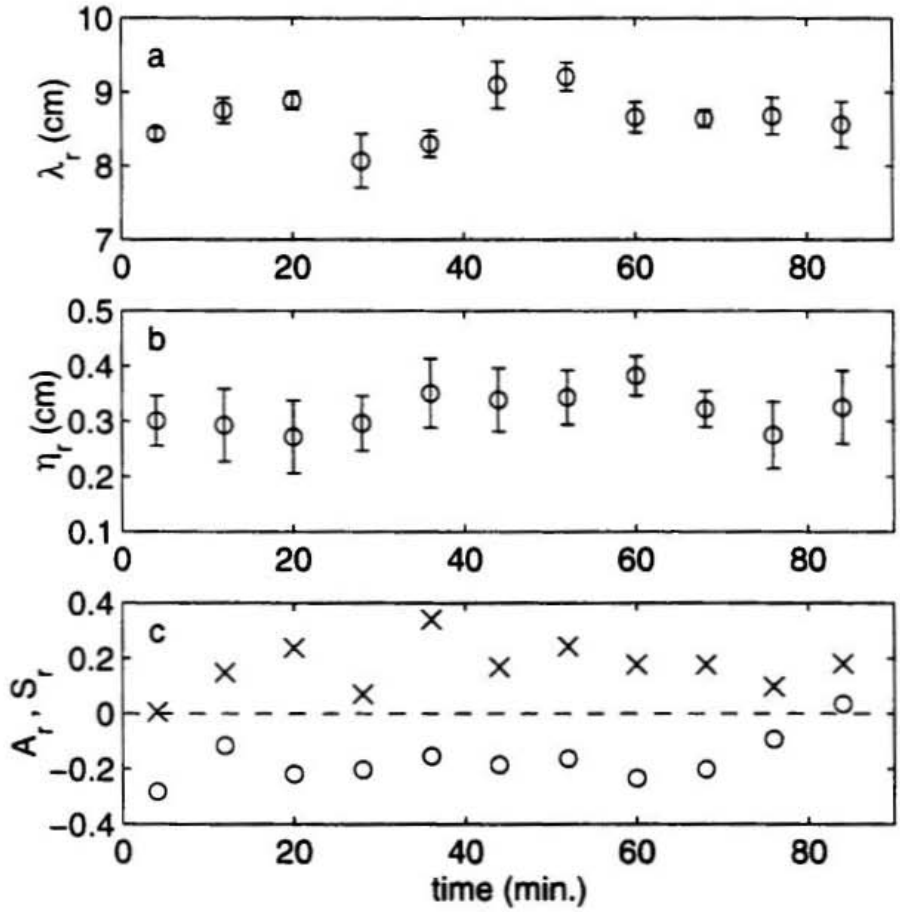


Figure 3.5: Ripple geometry over 1.5 hours during Interval I: (a) wavelength $\lambda_r$; (b) height $\eta_r$; (c) bedform profile skewness $S_r$ ($\times$) and asymmetry $A_r$ ($\circ$). Each point is an 8–minute average of quantities calculated from 20–second averaged profiles. The errorbars show plus or minus one standard deviation.

The variations in wavelength and height over the 1.5 hour period are small, with the mean wavelength being 8.5 cm ± 0.5 cm, and height, 3 mm ± 1 mm. This gives a steepness $\eta_r/\lambda_r$ of 0.04. Nielsen [1981] found $\eta_r/\lambda_r = 0.342 - 0.34\sqrt[4]{\theta_{2.5}}$ for field conditions, which for a Shields parameter of 0.4 (see Figure 3.1) predicts $\eta_r/\lambda_r = 0.07$ — higher than for these bedforms, though lying within the scatter of the observations that the empirical relation was based on [Nielsen, 1981, Figure 6]. The wave orbital diameter doubled over 1.5 hours from about 0.5 m to about 1 m with no significant change in ripple geometry. The ripple profile skewness and asymmetry show that the ripples are somewhat peaked in profile (positive $S_r$) and lean toward the offshore (negative $A_r$). Both of these properties can be verified by inspection of the profiles shown in Figure 3.4. The calculated asymmetry of the bedforms is sensitive to the bed slope, which has been removed. Clifton [1976] reported observations of ripple asymmetry as a function of $\Delta u_{1/3} = |u^+_{1/3}| - |u^-_{1/3}|$, the difference in the averaged one–third largest velocities during the forward and reverse flows, noting that asymmetric ripples generally migrate, and in the direction of their slip face. The low relief of these transition ripples indicates that the steeper face was not in fact a slip face and that the mode of migration may not have been by avalanching, however they were asymmetric in the direction of migration nonetheless.

Independent measurements of the bedforms were also obtained from the pencilbeam sonar operating at a fixed slant angle of 10° below horizontal, and directed offshore. Each image in Figure 3.6 is an 8–minute time series of acoustic intensity profiles. The acoustic backscatter from the ripple slopes facing the instrument appear as dark bands. The centre of the acoustic beampattern intersected the bed approximately 4.2 m along the bed from the instrument, which is at $(x,\ y) = (-3.2\text{ m}, -0.27\text{ m})$ in fanbeam coordinates (Figure 3.2), or 2.9 m offshore of the centre of the laser–video profile. Range along the bed is calculated from the instrument height above bottom, correcting for the slant angle and assuming a flat bed with a 2° offshore slope. The raw acoustic data were often saturated in intensity near the centre of the beampattern. The profiles shown are taken from the offshore shoulder of the beampattern and have been high–pass filtered to remove the long wavelength intensity modulation due to the beampattern itself.

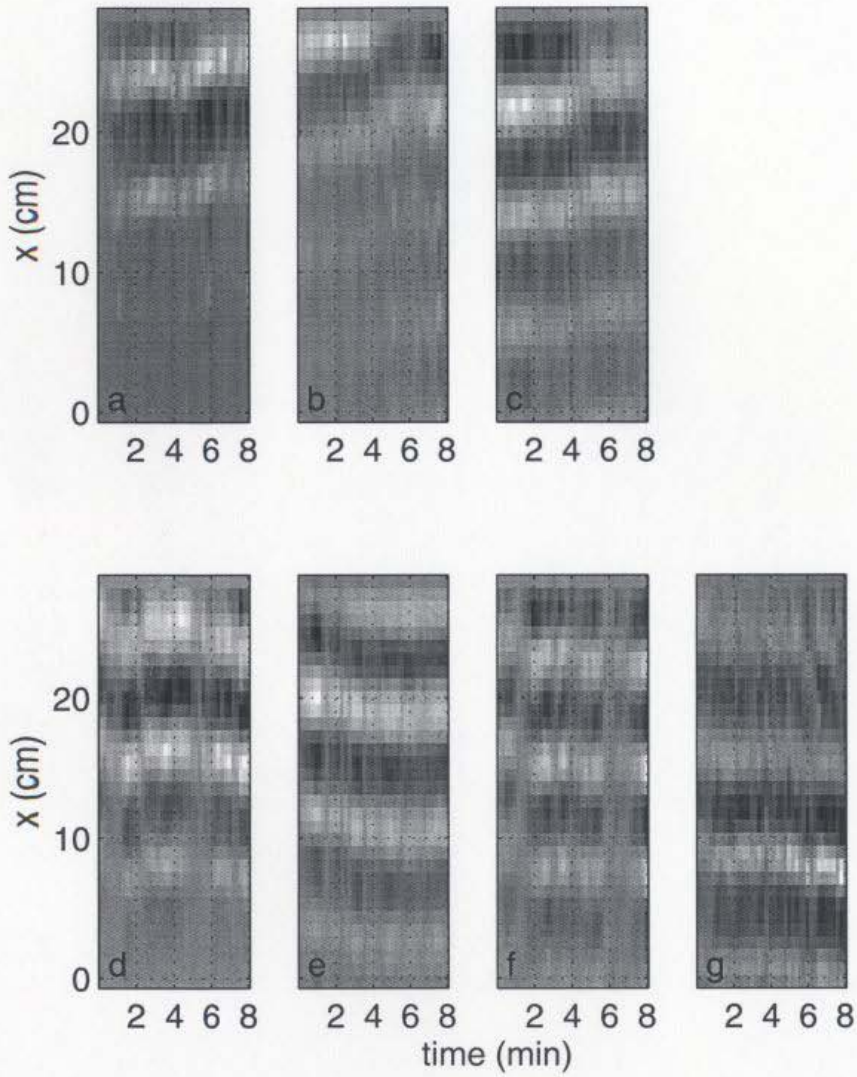


Figure 3.6: 8–minute slant pencilbeam sonar runs starting at 5:10, 5:55, 6:25 GMT (a, b, and c), during the growth phase of the storm (Interval I), and 11:25, 11:55, 12:25 and 12:55 GMT (d, e, f, and g), toward the end of the decay of the storm (Interval II). Offshore is toward the top of the images. Note offshore ripple migration in images a–c, and onshore migration in images d–g. The 22 minute gap between pencilbeam runs makes the identification of particular ripple crests in successive images uncertain.

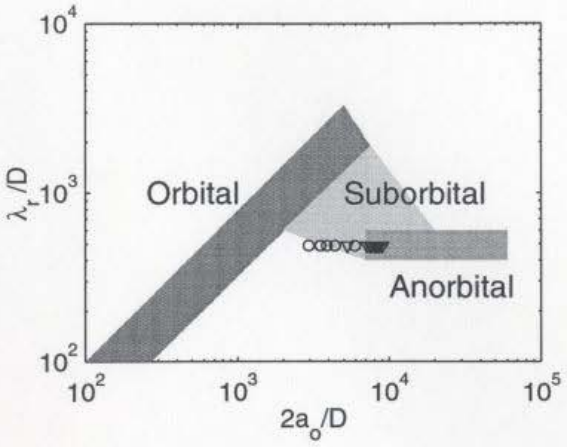


Figure 3.7: The position of the observed linear transition ripples in orbital diameter–ripple wavelength space, nondimensionalized by grain diameter. Symbols indicate observations from Interval I (○) and from Interval II (▽).

The first three images in Figure 3.6 were recorded during the growth phase of the storm (Interval I), and the last four, during storm decay (Interval II). It can be seen that ripple migration was offshore during the growth of the storm, consistent with Figure 3.3, and onshore during Interval II as the storm subsided. While migration was offshore, the onshore ripple faces (dark bands) appear to have been wider than while they were migrating onshore toward the instrument. This is consistent with asymmetry of the ripple profile in the direction of migration, as already seen from the laser–video data during Interval I.

Comparison can be made between the laser–video profile time series and the slant pencilbeam acoustic data. Ripple wavelengths calculated from the pencilbeam sonar bed profiles, by the same method as for the laser–video profiles, average to 8.5 cm in both Intervals I and II. This is further confirmed by the fanbeam sonar images. The ripple profile is only occasionally indistinct in the pencilbeam sonar data (gray vertical bands) when suspended material is of sufficient concentration to obscure the bed. In the case of image f, the ripples may have been erased by the flow. Both sets of measurements indicate, however, that in general the ripples persist for much longer than a wave period time scale.

The observed lack of dependence of ripple wavelength on wave orbital diameter, and

large orbital diameter–to–ripple wavelength ratio (5 to 10) are defining features of anorbital ripples [Clifton and Dingler, 1984]. Figure 3.7 diagrams ripple type in terms of ripple wavelength and wave orbital diameter, nondimensionalized by grain diameter. The shaded regions are adapted from Figure 1.1. The positions of the observed linear transition ripples in this parameter space are shown by the symbols, using the average ripple wavelength of 8.5 cm, the significant wave orbital diameter calculated from the CDP orbital velocities ($2a_{1/3} = 2u_{\rm rms}T_p/\pi$), and the median grain diameter, 175 $\mu$m. The larger orbital diameter cases lie within the anorbital ripple area of the diagram, while the lower orbital diameter cases fall in the suborbital range. Wiberg and Harris [1994] found anorbital ripple wavelength to depend on grain diameter as $\lambda_{\rm ano} = 535D$. They also found anorbital ripple height to be loosely dependent on wave orbital diameter, such that $\eta_{\rm ano} < 2a/100$. For a median grain diameter of 175 $\mu$m and orbital diameter of 1 m, these criteria yield $\lambda_{\rm ano} \approx$ 9 cm and $\eta_{\rm ano} < 1$ cm, consistent with the present ripple observations.

## 3.3 Transition Ripple Migration Velocities

Measurements of transition ripple migration velocity are presented in this section. The migration velocity during Interval I was determined from the laser–video profiles and from the slant pencilbeam sonar data, while during Interval II only pencilbeam sonar data are available.

The transition ripple migration velocity was calculated by the same method from both data sets — displacement was determined by finding the spatial lag of the peak correlation between successive 30–second mean bed profiles. The laser–video ripple migration velocity data were subsequently broken into 8–minute segments to match the length of the pencilbeam sonar time series. Figure 3.8 shows the 8–minute averaged migration velocities calculated by this method from both data sets, along with the nearbed orbital velocity skewness $S_u$, the mean nearbed flow velocity $\mathcal{U}$ and velocity asymmetry $A_u$. Intervals I and II are shaded. There are no migration velocity data for the period between 7:00 and

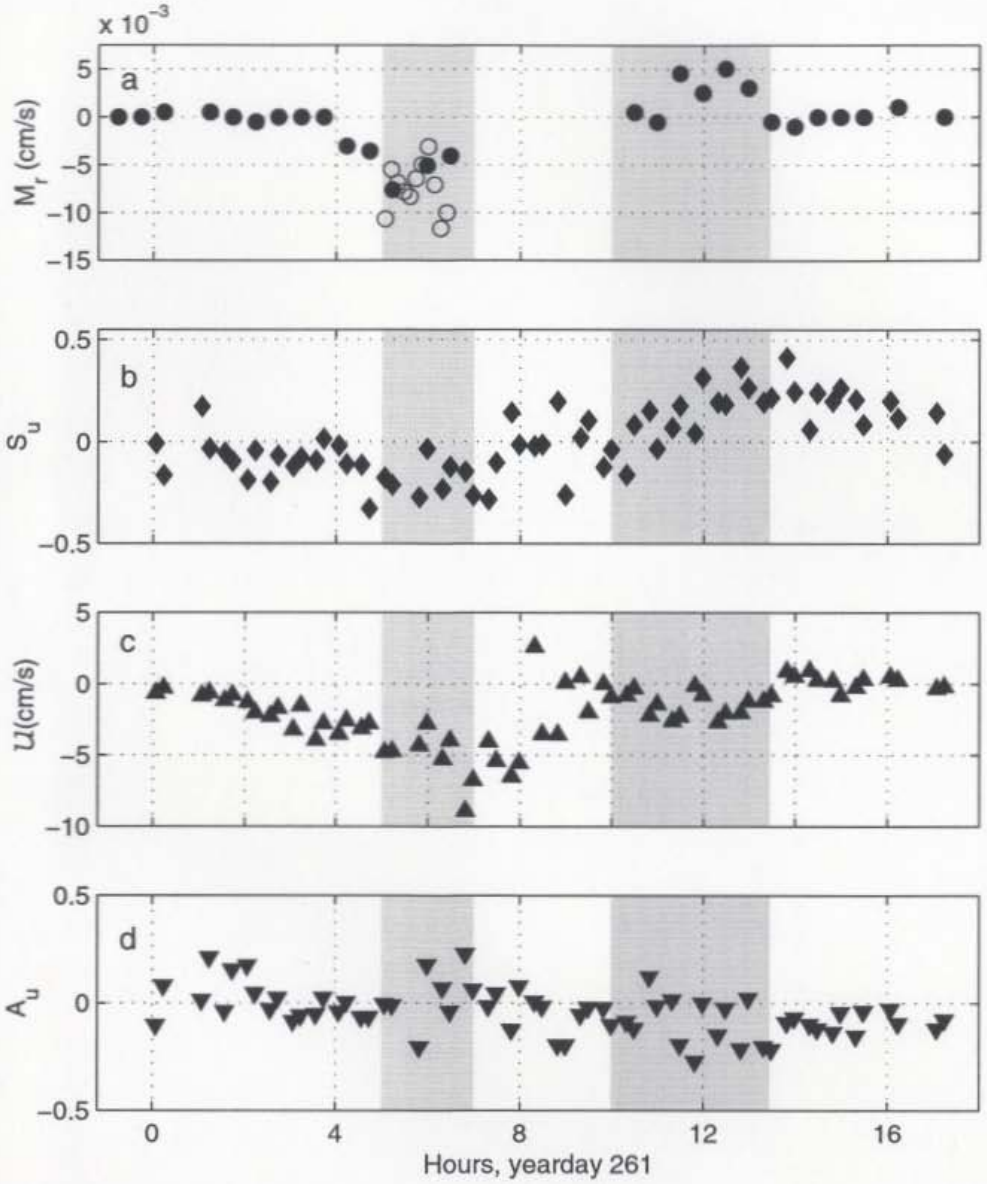


Figure 3.8: Ripple migration velocity and orbital velocity forcing conditions during the storm. (a) Ripple migration velocity $M_r$ determined from the pencilbeam sonar (•) and laser–video (○) data sets. (b) Nearbed orbital velocity skewness $S_u$. (c) Mean nearbed velocity $\mathcal{U}$. (d) Nearbed orbital velocity asymmetry $A_u$. All are averages over 8–minute time series. Intervals I and II, when linear transition ripples were observed, are shaded.

10:00 GMT during flatbed conditions. Between 10:00 and 11:00 GMT, bedform migration direction was switching between on and offshore over the 8–minute runs with net rates close to zero. These low migration velocities are distinct from low values at the beginning and end of the storm when the Shields parameter was small (Figure 3.1), and there was no coherent migration of the irregular ripple field.

During Interval I, ripple migration was offshore (negative). Near the middle of Interval II, ripple migration reversed to the onshore (positive) direction.

The maximum observed offshore migration rate was about 0.012 cm/s (0.7 cm/min) and the maximum onshore rate was about $5 \times 10^{-3}$ cm/s (0.3 cm/min). These values may be compared to those reported by Dingler and Inman [1977]: a maximum rate of 4.2 cm/min, in the onshore direction only.

Comparison of Figures 3.8a and b shows that the orbital velocity skewness was negative while ripple migration was in the offshore direction, and evolved to positive as ripple migration direction reversed to onshore. In fact, the correlation between transition ripple migration velocity and orbital velocity skewness or $u^3$ is better than 0.7, as shown in Figure 3.9. Ripple migration velocities and orbital velocity skewness measurements from Intervals I and II only are shown. The regression lines have a small negative offset in migration velocity for zero skewness or $u^3$. This negative offset is consistent with the small offshore mean nearbed flow velocity during both intervals (see Figure 3.8c): that is, the mean current would drive offshore migration even for zero skewness. This is discussed further in Appendix B, along with the correlation between ripple migration velocity and other higher powers of orbital velocity.

As discussed in Section 1.4, Dingler and Inman [1977] found positive correlation between ripple migration rate and Longuet-Higgins' [1957] nearbottom streaming velocity, $u_s = 5(a\omega)^2/4c$, where $c$ is the wave phase speed. This would predict ripple migration only in the direction of wave propagation, contrary to what was observed in Interval I. The observations reported here therefore imply a fundamental difference in the mechanism of ripple migration than that suggested by Dingler and Inman [1977].

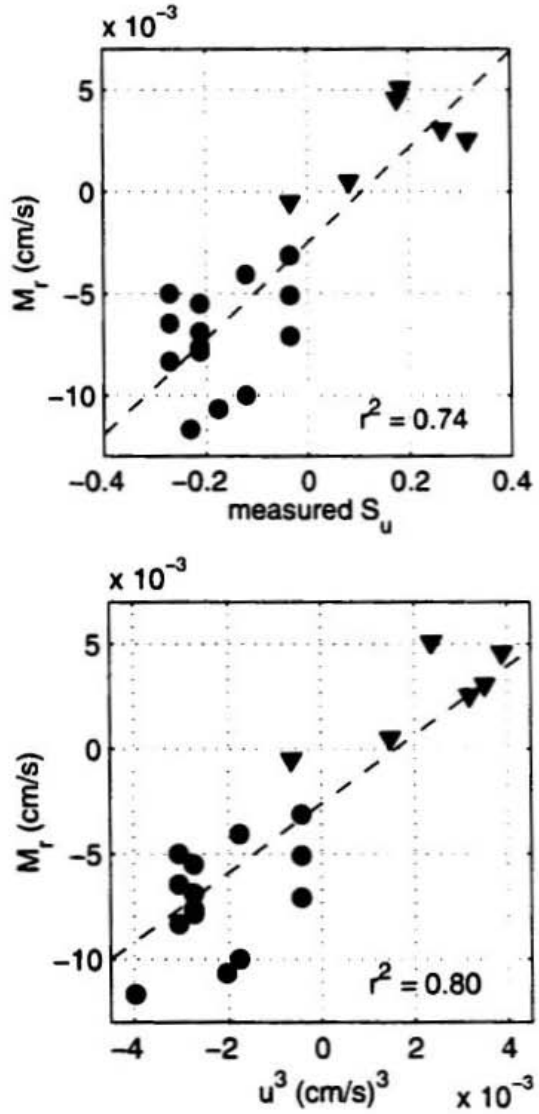


Figure 3.9: Transition ripple migration velocity $M_r$ plotted against orbital velocity skewness $S_u$ (a) and (demeaned) orbital velocity cubed $u^3$ (b) with linear regressions (dashed lines). The • symbols show migration velocities during Interval I, and the ▼ symbols, during Interval II.

## 3.4 Wave Orbital Velocity Spectra

A more detailed description of the wave orbital velocity forcing responsible for the observed bedform type and migration is presented in this section.

Figure 3.10 shows the wave orbital velocity power spectral density over the two intervals, calculated from the eight 8–minute CDP runs during Interval I, and from ten runs during Interval II. The CDP runs were low–pass filtered and resampled at 9.6 Hz (decimating to 4096 from 12000 samples) to roughly match the pencilbeam sample rate of 8 Hz for skewness calculations. For spectral analysis, the CDP records were then broken into 512 sample segments with 75% overlap and windowed with a Hanning window.

During Interval II, the orbital velocity spectra were essentially unimodal, while the spectra during Interval I were distinctly bimodal. It is also evident that the spectra remained quasi–stationary through the duration of Interval II, whereas there was a progressive strengthening of the lower frequency peak during Interval I. All 8 runs from Interval I were included in the following analysis, despite the apparent lack of stationarity compared to the orbital velocity spectra in Interval II. This was necessary in order to obtain the number of degrees of freedom required for significance of the bicoherence results to be presented later. All the velocity spectra from Interval I exhibit bimodality with similar peak frequencies, which will be demonstrated to be the feature of importance.

Ensemble–averaged spectra for the two intervals are shown in Figure 3.11, with the peaks relevant to the following discussion indicated by the arrows and labeled. The spectral density during Interval I is bimodal in the incident wave band, with peaks at 0.14 and 0.23 Hz ($f_I$ and $f_I'$). The Interval II spectrum exhibits a single dominant peak of lower frequency at 0.12 Hz ($f_{II}$), with a small shoulder at $2f_{II}$ (0.24 Hz). The spectra indicate evolution of the wave forcing from locally generated short period seas to longer period swell.

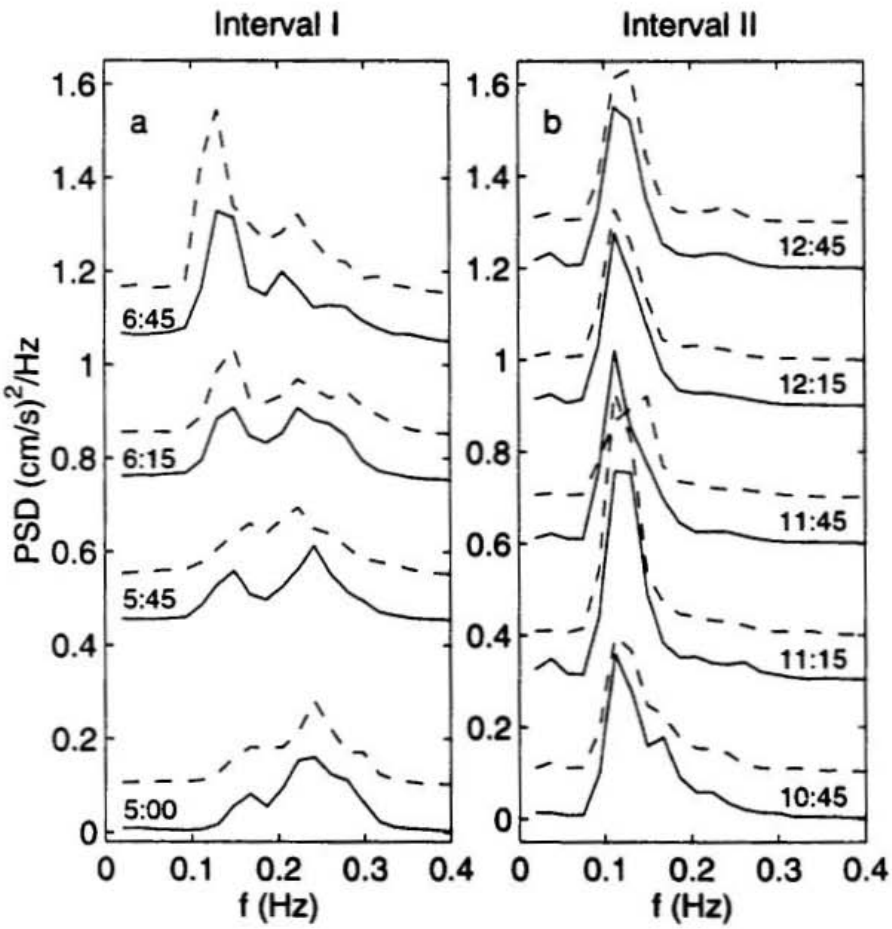


Figure 3.10: Power spectral densities of CDP measured nearbed orbital velocities during Interval I (a) and Interval II (b). The spectra in each pair (solid and dashed lines) come from 8–minute CDP runs started 10 minutes apart, labeled with the start time of the first. An offset proportional to the time from the first spectrum in each interval has been applied.

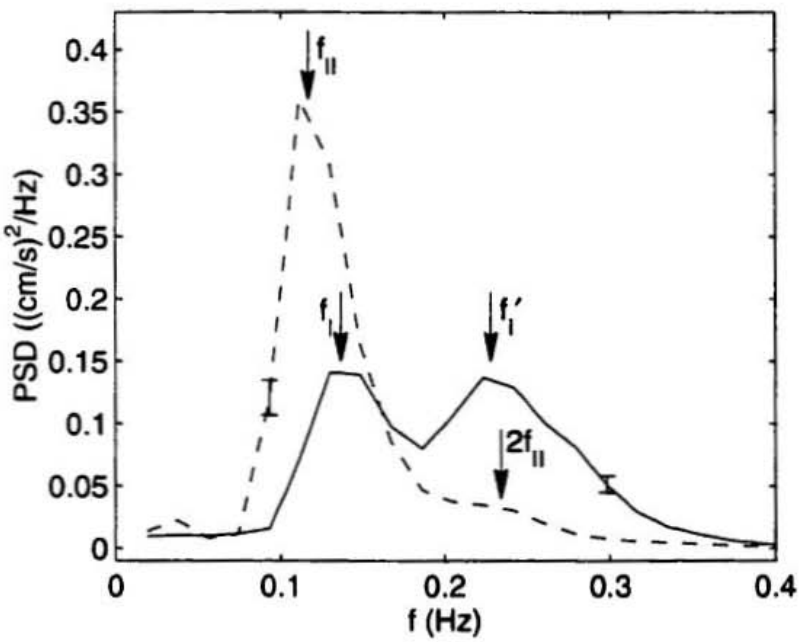


Figure 3.11: Ensemble averaged power spectral densities of nearbed orbital velocity during Interval I (solid) and Interval II (dashed). The 95% confidence limit is shown as an error bar with each curve (126 degrees of freedom for Interval I, 158 for Interval II). The spectral peaks are labeled $f_I$ and $f_I'$ for Interval I and $f_{II}$ for Interval II.

Table 3.2: Frequency pairs showing significant bicoherence at the 95% confidence level for Intervals I and II. The last column indicates the sign and magnitude of $\Re\{B\}$ at those frequencies.

| | $f_1$ (Hz) | $f_2$ (Hz) | $\Re\{B\}$ |
|---|---|---|---|
| Interval I | | | |
| Peak 1 | 0.23 ($f_I'$) | 0.23 ($f_I'$) | +0.01 |
| Peak 2 | 0.14 ($f_I$) | 0.09 ($f_I' - f_I$) | −0.06 |
| Peak 3 | 0.23 ($f_I'$) | 0.14 ($f_I$) | +0.03 |
| Interval II | | | |
| Peak 4 | 0.12 ($f_{II}$) | 0.12 ($f_{II}$) | +0.15 |
| Peak 5 | 0.24 ($2f_{II}$) | 0.12 ($f_{II}$) | 0 |

## 3.5 Origin of the Orbital Velocity Skewness — Bispectral Analysis

Skewness can be considered a measure of wave nonlinearity, since nonzero skewness arises in the wave form through nonlinear processes. This section contains further examination of the orbital velocity forcing using bispectral analysis. The mathematical forms for the bispectrum and bicoherence were presented in Section 1.7.

Figure 3.12 shows the orbital velocity bicoherence for the two intervals, at frequencies below 0.4 Hz. The lowest contour is the 95% confidence level. The frequency resolution, with 2–point merging in both frequency dimensions, is 0.037 Hz. Areas of significant bicoherence indicate frequency pairs ($f_1, f_2$) that are involved in either sum or difference interactions. The frequency locations of the significant bicoherence peaks are summarized in Table 3.2, with reference to frequencies labeled in Figure 3.11 (note that the bicoherence peak positions match the spectral peak positions to within the lower bicoherence frequency resolution). Three bicoherence peaks significant at the 95% confidence level are present in Interval I (Peaks 1, 2 and 3, Table 3.2) and two in Interval II (Peaks 4 and 5, Table 3.2).

Figure 3.13 shows the real part of the bispectrum of the orbital velocity for the two intervals. Significant nonzero $\Re\{B\}$ is limited to frequencies below 0.4 Hz. The real

part of the bispectrum is related to skewness by Equation 1.45. The sign of $\Re\{B\}$ at frequencies $(f_1, f_2)$ indicates the sign of the contribution to the overall skewness arising from the interaction involving those frequencies. The last column of Table 3.2 indicates the value of $\Re\{B\}$ at the frequencies of the bicoherence peaks.

During storm growth, the bimodal orbital velocity spectrum shows the development of a progressively more energetic lower frequency swell peak, with the higher energy peak shifting from the 0.23 Hz ($f_I'$) peak to the 0.14 Hz ($f_I$) peak (see Figure 3.10a). The real part of the bispectrum for Interval I (Figure 3.13a) is negative around Peak 2 (Table 3.2), while Peak 1 is a positive self–self interaction peak of lesser magnitude. Peak 3 has positive $\Re\{B\}$ showing a sum interaction between frequencies $f_I'$ and $f_I$, but has lower bicoherence. The large negative $\Re\{B\}$ Peak 2, and negative values at surrounding frequencies, lead to an overall negative integrated orbital velocity bispectrum (negative skewness). Peak 2 shows a difference interaction between frequencies $f_I$ and $f_I'$, the peak frequencies of the bimodal Interval I orbital velocity spectrum: $(f_1, f_2, f_1 + f_2) = (f_I, f_I' - f_I, f_I')$.

During storm decay, the dominant peak in the unimodal velocity spectrum is the swell peak which increased in energy through Interval I, and evolved to a lower frequency, 0.12 Hz ($f_{II}$) (see Figure 3.10b). The real part of the corresponding bispectrum shows a strong positive self–self interaction peak (Peak 4, Table 3.2). The harmonic, Peak 5, is associated with essentially zero $\Re\{B\}$. The small negative peak in $\Re\{B\}$ at $(f_1, f_2) = (f_{II}, 0.02$ Hz) has very low bicoherence. The orbital velocity skewness in Interval II is dominated by the large positive self–self interaction shown by Peak 4.

The positive skewness associated with naturally occurring waves can be understood as a self–self interaction. In shallower water, there is a near–resonant energy transfer to higher harmonics, as can be described by the usual Stokes expansion. This is seen spectrally as a train of harmonic peaks following the fundamental frequency peak, or a wide–spread broadening of the spectrum [Elgar and Guza, 1985b, 1986, present examples]. Since these harmonics are phase–locked to the primary forcing frequency, the result is a superposition of even harmonics in phase with the primary peak.

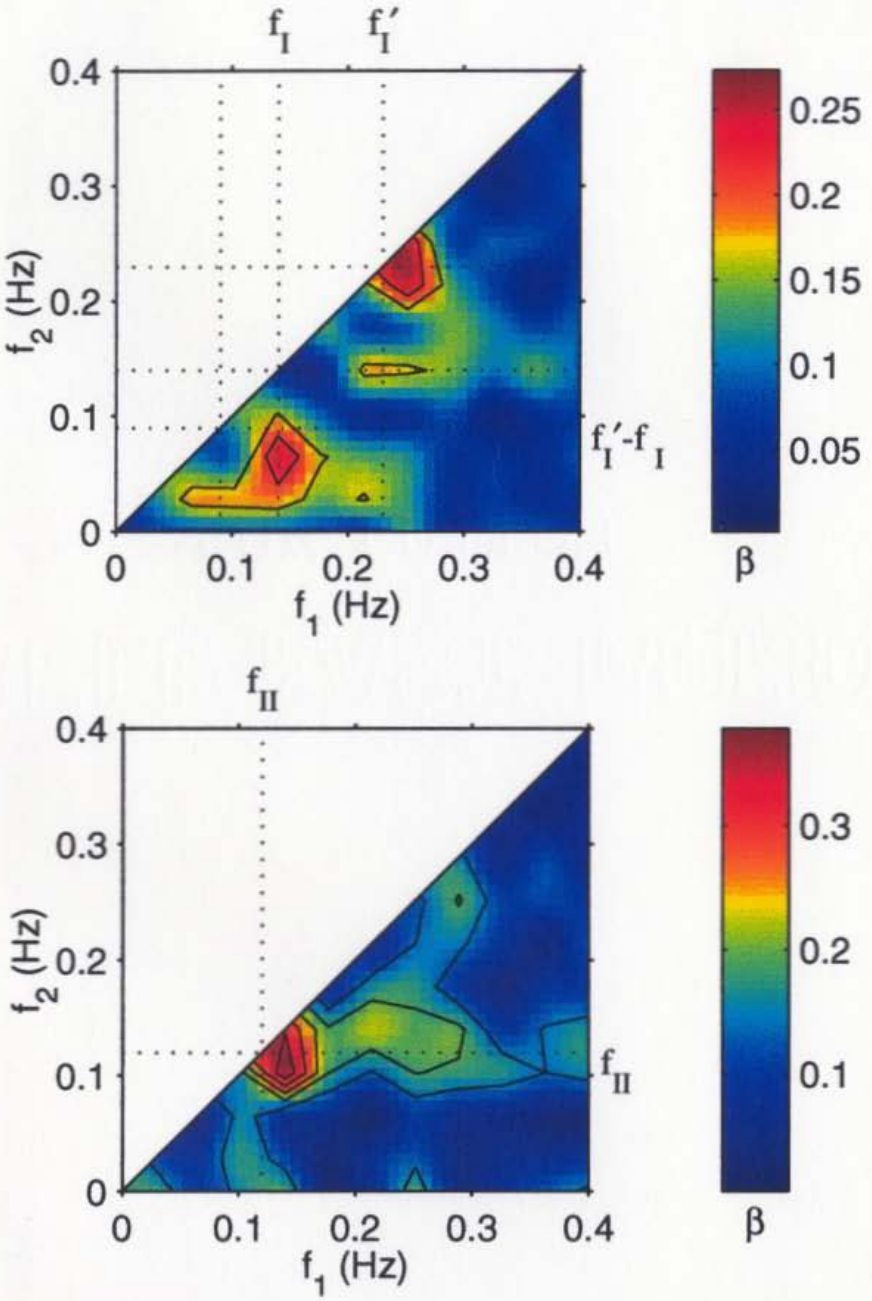


Figure 3.12: Bicoherence of nearbed orbital velocity during Interval I (a) and Interval II (b), with 256 degrees of freedom in (a) and 320 in (b). Successive contours are 0.05 apart. The lowest bicoherence contour is at the 95% confidence level. The colour scales are slightly different, as indicated by the colour bars on the right.

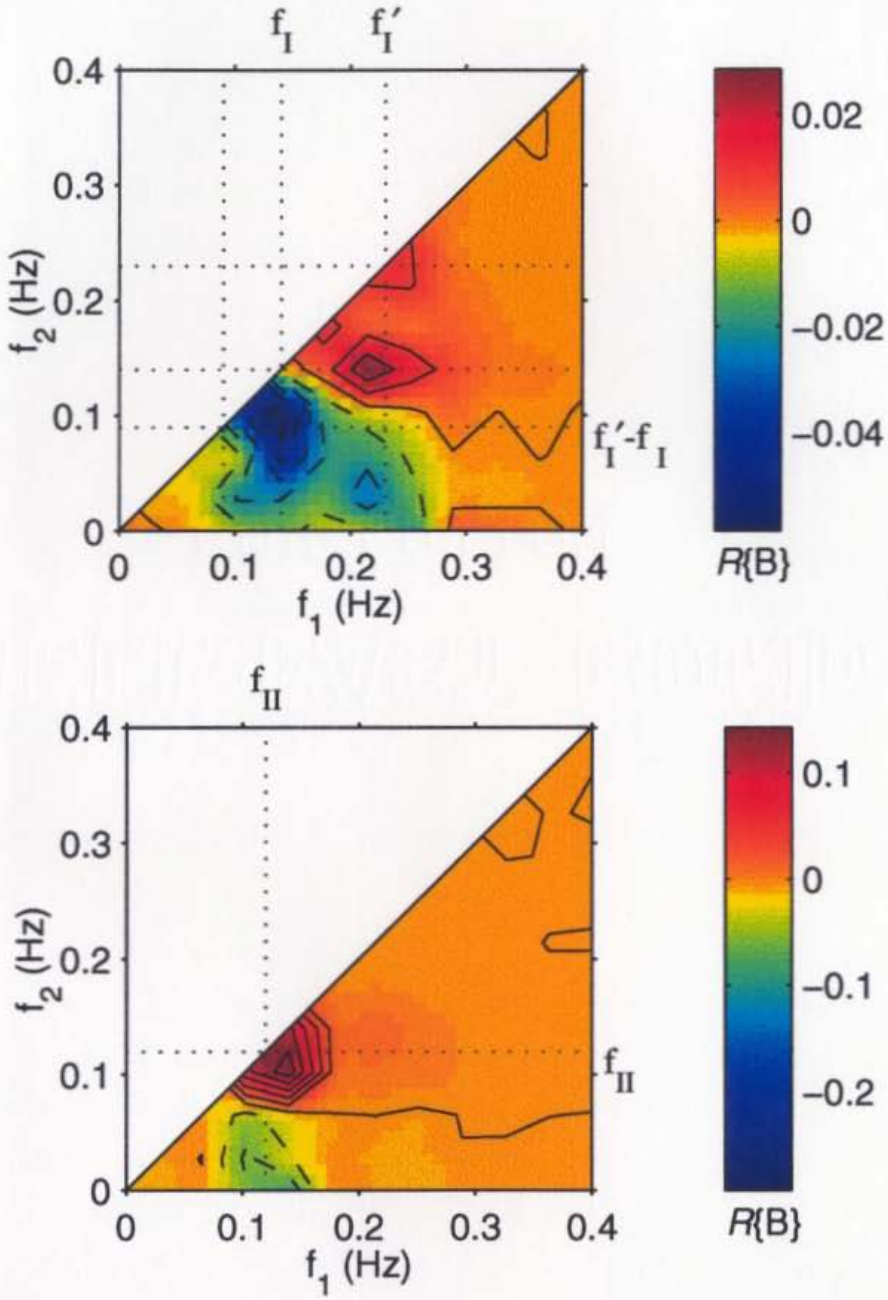


Figure 3.13: The real part of the bispectrum of the nearbed orbital velocity during Interval I (a) and Interval II (b). The dashed contours of $\Re\{B\}$ are negative values and solid are zero and positive, at intervals of 0.01 in (a) and 0.025 in (b). The colour scale has been set so the zero levels are equal in the two plots, but are scaled differently.

Physically, the effect on skewness of the difference frequency interaction can be understood through the following argument. The long wavelength difference frequency interaction has a group or bound wave response, driven by the gradient of the radiation stress [Longuet-Higgins and Stewart, 1962]. In terms of surface elevation, the bound wave is manifested as a depression of the mean surface elevation under the largest waves of the group. There is a corresponding lift under the smallest waves at the beginning and end of the group. A peaked wave (positively skewed otherwise) in the middle of the group rides on the depressed surface and can have negative skewness if there is sufficient negative offset due to the bound wave. The bound wave response is a second–order effect, though it may only require a small offset to reverse the sign of the wave skewness. In the case of naturally occurring waves, high frequency content of the surface elevation may lead to positive surface elevation skewness even in the presence of groups. Near the bed, however, the corresponding orbital velocities will have been, in effect, low–pass filtered by depth attenuation of the higher frequencies and can therefore exhibit negative skewness even if the surface elevation is positively skewed.

## 3.6 Comparison with Linear and Second–order Theories

This section contains discussion of the observed orbital velocity skewness. Comparison is made between the velocity skewness observations and skewness of velocities derived from surface elevation time series using frequency–dependent linear theory. Then the negative velocity skewness observed during Interval I is compared to predictions by a second–order wave interaction formulation described by Wells [1967], based on the work of Miche [1944] and Biésel [1952]. The positive velocity skewness observed during Interval II is compared to skewness of a Stokes representation of nearbed velocity.

Nearbed orbital velocity can be calculated from time series of surface elevation using frequency dependent linear depth attenuation. Thornton and Guza [1989] have shown that spectra of orbital velocity calculated from surface elevation measurements using this

method give good agreement with spectra of measured velocities for wind wave frequencies (0.05 and 0.3 Hz). Surface elevation was measured by the pencilbeam sonar, directed upward, in 8–minute runs. Spectral frequency components of each surface elevation time series were depth attenuated to 20 cm above the bed using linear theory and the full dispersion relation, and the velocity reconstructed by inverse Fourier transform. The skewness of the resulting time series was then computed. Figure 3.14 shows the comparison between measured and calculated orbital velocity skewness for both Intervals I and II. Though there is a bias toward higher computed velocity skewness and some degree of scatter ($r^2$ = 0.55), the points lie close to the 1:1 line, indicating that the linear theory prediction of the third moment of velocity (from $\zeta$) is roughly consistent with that of the CDP velocity measurements. This agreement suggests that, in the absence of nearbed measurements, linear theory can be used to estimate orbital velocity skewness from surface elevation time series. This is not entirely expected since, as has been demonstrated in Section 3.5, there are nonlinear contributions to the observed velocity spectra.

The skewness of the surface elevation itself is also shown in Figure 3.14. This is always positive: the high frequency components leading to positive skewness of the surface elevation are filtered out by depth attenuation in the calculated orbital velocity, as was described in the previous section. The ensemble–averaged surface elevation power spectral densities for the two time intervals are shown in Figure 3.15, calculated from three 8–minute upward looking pencilbeam sonar surface elevation time series in Interval I, and seven runs in Interval II. Comparing Figures 3.11 and 3.15, it can be seen that the surface elevation spectra show more high frequency content than the nearbed orbital velocity spectra. This is more evident in the Interval I case, where the high frequency shoulder of the higher frequency wind wave peak in the surface elevation spectrum has been lost in the corresponding nearbed velocity spectrum. The depth attenuation process acts as a low pass filter with a half–power point (in 3.8 m water depth) at a frequency of 0.25 Hz.

Over the duration of the storm event, the change in sign of wave orbital velocity skewness was associated with evolution of the wave forcing. Negative skewness, as seen in Interval I, can arise from interaction between waves through a mechanism such as

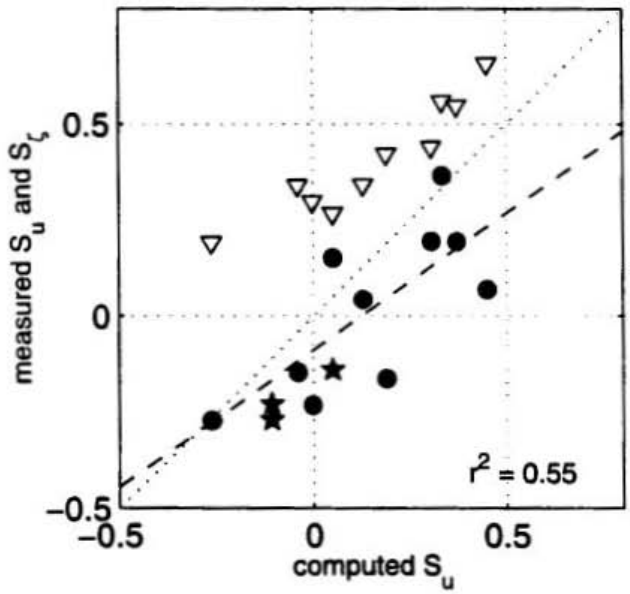


Figure 3.14: Comparison of measured velocity skewness with that of velocity calculated from surface elevation for both Intervals (•). Comparison with velocity skewness calculated by the MBW method, described in following text, is also shown (★). The ▽ symbols indicate the skewness of the measured surface elevation $S_\zeta$. The dashed line is a least squares linear regression to the • symbols (linear velocity calculation comparison).

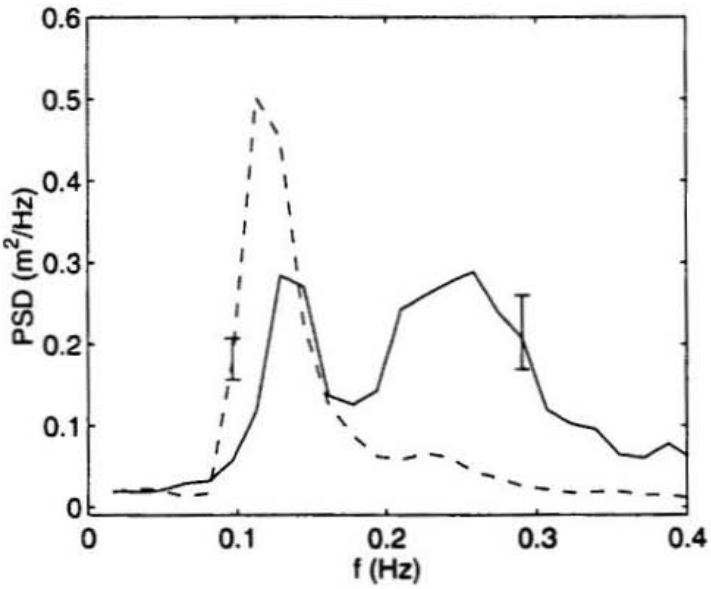


Figure 3.15: Ensemble averaged power spectral densities of surface elevation $\zeta$ measured by upward looking pencil beam sonar during Interval I (solid) and Interval II (dashed).

that described by Miche [1944] and Biésel [1952]. The orbital velocity, $u$, arising from two monochromatic colinear wave trains, including second–order interaction, is given by [Biésel, 1952; Miche, 1944]

$$u = \sum_{i=1}^{2} \{\mathcal{A}_i \cos \omega_i t + \mathcal{B}_i \cos 2\omega_i t\} + \mathcal{S}_{21} \cos[(\omega_2 + \omega_1)t] + \mathcal{D}_{21} \cos[(\omega_2 - \omega_1)t] \quad (3.4)$$

where $\mathcal{A}_i$ and $\mathcal{B}_i$ are the Stokes first and second–order coefficients and $\mathcal{S}_{21}$ and $\mathcal{D}_{21}$ are second–order sum and difference interaction coefficients. The coefficients are depth dependent functions of the amplitudes and frequencies of the two wave trains (see Appendix A for the full equations). Note that the velocity form of Hasselman et al.'s [1963] more general spectral representation can be shown to be equivalent to Equation 3.4 for the case of two co–linear discrete frequency wave trains. Wells [1967] derived the second and third

moments of $u$, based on Equation 3.4, given by

$$E[u^2] = \frac{1}{2}\sum_{i=1}^{2}(\mathcal{A}_i^2 + \mathcal{B}_i^2) + \frac{1}{2}(\mathcal{S}_{21}^2 + \mathcal{D}_{21}^2) \tag{3.5}$$

and

$$E[u^3] = \frac{3}{4}\sum_{i=1}^{2}\mathcal{A}_i^2\mathcal{B}_i + \frac{3}{2}(\mathcal{A}_2\mathcal{A}_1\mathcal{S}_{21} + \mathcal{A}_2\mathcal{A}_1\mathcal{D}_{21}) \tag{3.6}$$

Orbital velocity skewness is then given by Equation 1.8. This approach for calculation of nearbed velocity skewness will henceforth be referred to as the MBW method.

Second–order interaction leads to positive or negative orbital velocity skewness in the MBW formulation, depending on the balance between the positive terms ($\mathcal{A}_i$, the harmonic $\mathcal{B}_i$ term and the sum $\mathcal{S}_{21}$ term) and the negative difference $\mathcal{D}_{21}$ term. For a given pair of wave trains, skewness is a function of water depth, and height above the bottom (see Appendix A). Note that the mathematically simpler solution for two wave trains presented by Longuet-Higgins and Stewart [1962] is not appropriate here since that derivation requires that the two wave numbers (or frequencies) differ by only a small amount.

The velocity skewness at depth predicted by the MBW method was calculated from surface elevation quantities (wave amplitudes, wave numbers and frequencies) determined from the individual 8–minute spectra (ensemble–averaged spectra are shown in Figure 3.15). The velocity skewness was calculated for three times during Interval I when CDP and upward looking pencilbeam runs coincide, shown in Table 3.3. In each case, the wave amplitude, $a$, at each peak frequency was determined from twice the square–root of the integrated surface elevation power spectral density (including the peak value and one point to each side in the integration), i.e. the significant wave amplitude. The issue of the appropriate wave amplitude values to use is relevant since Interval I velocity skewness values can be calculated which agree very closely with the measurements (less than 2% difference) when twice the wave amplitudes shown Table 3.3 were used.

For validity of the second order perturbation representation of velocity (Equation 3.4), the ratios of the second order coefficients $\mathcal{B}_i$, $\mathcal{S}_{21}$ and $\mathcal{D}_{21}$ to the first order coefficient $\mathcal{A}_i$ (the Ursell numbers) must be small. These are listed in Table 3.3 for the pairs of waves at

Table 3.3: Comparison of the skewness of CDP measured orbital velocity and velocity skewness calculated using the MBW theory at three times during Interval I ($h$ = 3.8 m). Values determined from each of the two surface elevation spectra peaks are given for wave amplitude $a$ (in meters) and $kh$, with the primed notation referring to values for frequency $f_I'$. The Ursell numbers, $Ur$, are the ratios of the second order terms to the first order term for the two wave trains ($Ur = \mathcal{B}/\mathcal{A}$, $Ur_S = \mathcal{S}_{21}/\mathcal{A}$ and $Ur_D = \mathcal{D}_{21}/\mathcal{A}$).

| time | $S_{meas}$ | $S_{calc}$ | $a$ | $kh$ | $Ur$ | $Ur_S$ | $\lvert Ur_D \rvert$ |
|---|---|---|---|---|---|---|---|
| | | | $a'$ | $(kh)'$ | $Ur'$ | $Ur_S'$ | $\lvert Ur_D' \rvert$ |
| 5:45 | −0.27 | −0.11 | 0.16 | 0.60 | 0.07 | 0.10 | 0.24 |
| | | | 0.26 | 1.11 | 0.02 | 0.08 | 0.19 |
| 6:15 | −0.23 | −0.11 | 0.21 | 0.62 | 0.10 | 0.09 | 0.22 |
| | | | 0.26 | 1.25 | 0.02 | 0.10 | 0.25 |
| 6:45 | −0.14 | 0.05 | 0.28 | 0.53 | 0.17 | 0.13 | 0.24 |
| | | | 0.21 | 0.92 | 0.03 | 0.20 | 0.37 |

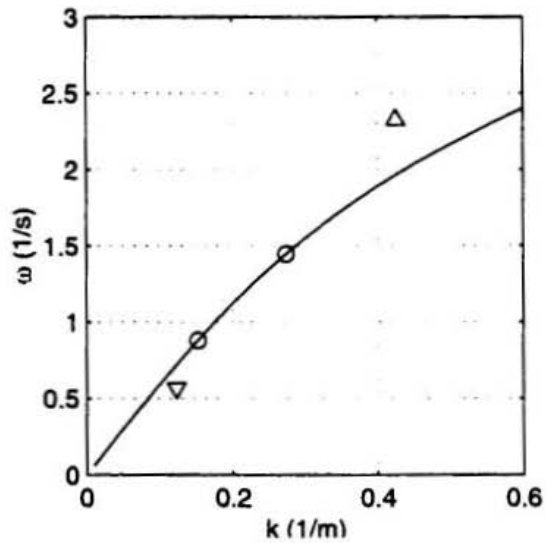


Figure 3.16: Position in $k$–$\omega$ space of the interacting and forced waves during Interval I. The bimodal spectra peak free waves are indicated by the ∘ symbols and △ and ▽ denote the sum and difference interaction waves. The line shows the dispersion relation curve.

frequencies $f_I$ and $f_I'$ at each of the three times. The values of $Ur_D$ are large. This indicates amplification of the difference frequency response in shallow water [Phillips, 1960]. The largest value, $Ur_D' \sim 0.4$, coincides with the poorest comparison between calculated and measured velocity skewness (in the sense that the sign is incorrectly predicted), indicating that this case is probably outside the range covered by the weakly nonlinear second order theory.

The values of $kh$ for the higher frequency ($f_I'$) waves are almost equal to or greater than 1 (Table 3.3), indicating that these waves are dispersive. Figure 3.16 illustrates the positioning of the sum and difference wave numbers and frequencies during Interval I, relative to the dispersion relation. Free waves at the peak frequencies of the bimodal spectrum, $f_I$ and $f_I'$, lie on the dispersion relation curve. The forced sum and difference interaction waves lie above and below the curve, assuming parallel wave vectors. That the forced waves lie off the dispersion curve implies that these interactions are non–resonant [Phillips, 1960; Herbers and Guza, 1991]. As Phillips pointed out, however, even though the difference interaction is non–resonant, the amplitude of the response is inversely proportional to the difference between its frequency and that of the free wave of the same wave number, i.e. a larger response is expected for a smaller displacement from the dispersion curve, as indicated here for the difference interaction as compared to the sum interaction.

During Interval II, the average orbital velocity skewness was positive, as shown in Table 3.4. An estimate of the velocity skewness for the case of a wave with a unimodal (monochromatic) frequency distribution can be made using the Stokes expansion relationship for $u$ (Equations 1.10–1.12). The results of this calculation, averaged over Interval II, are also shown in Table 3.4. The wave period was almost constant with an average value of 8.5 s and water depth decreased from 3.4 to 2.9 m over the time period. The amplitude, $a$, of the peak frequency waves was determined by the same method as described for Interval I. The question of choice of wave amplitude arises again here as in the Interval I case: the values of $a$ for each 8–minute run were about 30% smaller than the significant wave amplitudes given by $\sqrt{4\langle\zeta^2\rangle}$ (Table 3.1). Even using these smaller amplitudes, $\langle S_{Stokes}\rangle$ does not compare well with the observed velocity skewness. In this

Table 3.4: Comparison of ensemble–averaged CDP measured orbital velocity skewness and skewness calculated using a Stokes expansion for $u$ in Interval II. The ensemble–averaged wave amplitude $a$ (in meters), $kh$, and Ursell number are also shown.

| $\langle S_{meas} \rangle$ | $\langle S_{Stokes} \rangle$ | $\langle a \rangle$ | $\langle kh \rangle$ | $\langle Ur \rangle$ |
|---|---|---|---|---|
| 0.12 | 0.60 | 0.27 | 0.42 | 0.33 |

case, the Ursell number is not small ($> 0.3$) so that the Stokes expansion second order term is larger than a "perturbation" — this situation is outside the range of validity of this approach. A Boussinesq–type model [Elgar and Guza, 1986, e.g.], which can reproduce shoaling behaviours such as skewness and asymmetry evolution, is probably needed in this case.

Figure 3.17 shows the wave number frequency relationship between the primary ($f_{II}$) and harmonic during Interval II, relative to the dispersion relation. The self–self interaction leading to the harmonic is a sum interaction. The smaller displacement of the harmonic frequency from the free wave dispersion relation (compare Figure 3.16) implies a large sum interaction response during Interval II.

The variation of velocity skewness with distance above bottom can also be examined using both the MBW theory and velocities calculated from surface elevation measurements. The orbital velocity skewness observed near the bed during Interval I was negative while the surface elevation had positive skewness. Figure 3.18 illustrates the skewness calculated both from velocities derived from surface elevation time series by frequency–dependent depth attenuation using linear theory and by the MBW calculation, for the same wave periods and amplitudes as presented in Table 3.3.

The results shown in Figure 3.18 demonstrate that in this water depth, both calculation methods recover negative velocity skewness near the bed from positively skewed surface elevation time series. The two calculations show different forms of depth dependence, but both have a low level of depth dependence near the bed and cross from negative to positive values at comparable heights in these cases. The nearly constant skewness with height

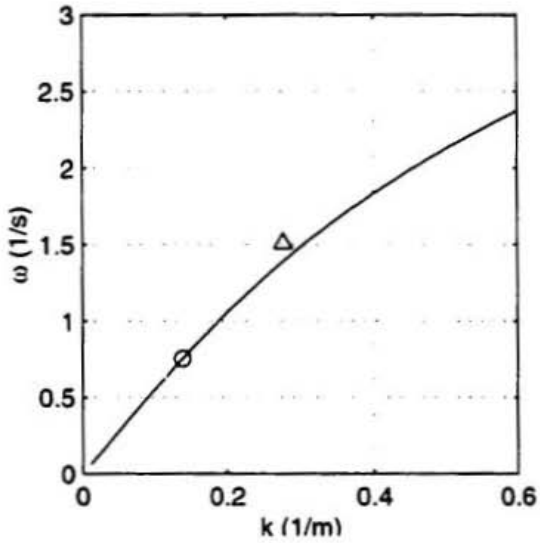


Figure 3.17: Position in $k$–$\omega$ space of the primary (○) and harmonic (△) waves during Interval II. The line is the dispersion relation curve calculated for the mean water depth of 3.2 m.

near the bed suggests that the nearbed measurement height is not a critical factor in velocity skewness measurement outside the boundary layer. With only a single measurement point, further comparison would be speculative. The very close agreement between the CDP measurement and the skewness of the depth attenuated velocity in the case shown in Figure 3.18a is coincidental, as can be verified by examining Figure 3.14.

## 3.7 Angle of Wave Incidence

The effects of non–normal wave incidence and, potentially of more relevance to wave interaction, directional spread in the incoming wave forcing [Elgar and Guza, 1985b; Herbers and Guza, 1994] have not been considered in this analysis. Figure 3.2 clearly shows the ripple crests were aligned about 15° from the $y$–axis of the measurements, in a direction roughly parallel to the large scale shoreline of the head of the bay (shown by the dashed lines in Figures 2.8 and 2.9). This means that the measurements of ripple wavelength and migration velocity, shown in Figures 3.5 and 3.8, are approximately 3% larger

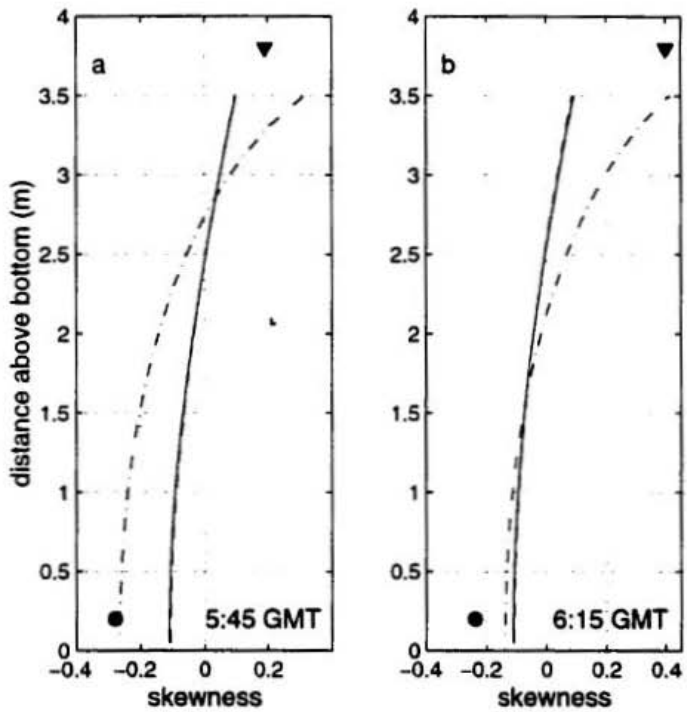


Figure 3.18: Calculated velocity skewness as a function of height above bottom: MBW calculated skewness (solid), and skewness of velocity calculated by depth attenuated linear theory (dash–dot) at 5:45 GMT (a) and 6:15 GMT (b). The CDP measured orbital velocity skewness (•) and surface elevation skewness (▼) are indicated.

than the actual crest–normal values. This is a sufficiently small difference that correction has not been made. If it is supposed that the ripple crests were oriented normal to the dominant wave incidence direction, then in this case, the measured horizontal orbital velocity component would be correspondingly smaller by 4% than in a ripple crest oriented coordinate system. The effect of an unresolved orthogonal velocity component has not been assessed, however, multiplication by a constant factor does not affect the skewness of $u$. The one–dimensional approach which has been taken here, despite these potential complications, appears to provide a reasonable explanation of the observations.

## 3.8 Summary and Discussion

Anorbital linear transition ripples have been observed during both the growth and decay phases of a storm event. High resolution bed profile measurements during storm growth show little variability in the ripple geometry despite a doubling in wave orbital diameter. Acoustic measurements (fanbeam and pencilbeam sonars) show the ripples had the same ripple wavelength during both storm phases.

The migration velocity of the linear transition ripples is shown to have reversed direction through the course of the storm, migrating offshore during storm growth and onshore during storm decay. The migration velocity is well correlated with the measured orbital velocity skewness and with the third power of velocity ($r^2 > 0.7$).

The observed orbital velocity skewness has been shown to originate in nonlinear interactions between frequency components of the wave forcing. Bispectral analysis shows that a difference interaction between the peak components of the bimodal velocity spectrum during storm growth led to the observed negative orbital velocity skewness. During storm decay, the velocity spectrum was dominated by a lower frequency swell peak, which through a self–self interaction, gave positive orbital velocity skewness.

The negative orbital velocity skewness observed during storm growth has been favorably compared with skewness predicted by the MBW second–order wave theory. A Stokes description of the nearbed orbital velocity does not contain enough wave shoaling physics

to accurately represent the positive skewness observed during storm decay.

Presuming that ripple migration is related to sediment transport, these results suggest a possible explanation for the commonly observed beach storm cycle. During a typical storm cycle, sediment is removed from the beach during the initial stages of the storm and replaced as the storm passes. The results above show that as a storm grew in intensity, locally–generated wind waves interacted with swell that came in with the storm. In the shoaling region of the beach, this bimodal wave energy spectrum led to negative skewness (and offshore migration) through sea–swell difference interactions. In contrast, as the storm waned, unimodal residual swell produced positive skewness (and onshore migration) through sum interactions. The transport direction in the shoaling region may not directly reflect the transport at the shoreline where the storm cycle is typically observed. It is also being presumed, therefore, that on an unbarred profile like Queensland Beach, the transport direction in the two areas is directly related.

In future experiments, it would be useful to measure the beach profile change at the shoreline in order to examine the cross–shore variation in sediment transport, and the directional wave spectrum offshore in order to resolve the dependence of wave–wave interactions on the angular spread of the incoming wave field.

# Chapter 4

# Conclusions

The two deployments of the laser–video system have demonstrated the effectiveness of the technique. High resolution bedform profiles have been successfully obtained in the field through a range of wave conditions almost up to the flatbed threshold. The sediment suspension imaging capability of the system has been verified, clearly showing the time and spatial scales and rotational motions of suspension events, as well as providing the first measurements of the alongshore length scales of suspended sediment clouds.

Field observations of linear transition ripples (low relief, long crested, anorbital bedforms) obtained using the laser–video system are part of a very comprehensive data set which also includes high quality nearbed velocity and scanning sonar bedform measurements. The transition ripples existed in moderately energetic flow conditions, for which sediment transport rates can be large. In light of the difficulty of obtaining good estimates of sediment transport, this set of observations provides valuable insight into sediment transport processes in the shoaling region under intermediate energy conditions.

The acoustic bedform measurements show that the wavelength and overall pattern of the transition ripples were similar during both the growth and decay of a storm event under a similar range of wave energies. The very high spatial resolution of the laser–video system allowed detailed observation of ripple shape. The mean transition ripple wavelength was $8.5 \pm 0.5$ cm and height, $0.3 \pm 0.1$ cm. During offshore migration, the ripple profiles were slightly positively skewed and pitched forward in the direction of migration.

The ripple migration rate was highly correlated with the skewness and third moment of the wave orbital velocity ($r^2 > 0.7$). Both onshore and offshore ripple migration was observed, with average rates of $-0.4$ cm/min offshore and 0.2 cm/min onshore. The average orbital velocity skewness was $-0.17$ (0.16) during offshore (onshore) ripple migration, and skewness and migration velocity were correlated for both cross–shore directions. A weak offshore mean flow velocity ($-3$ cm/s average) resulted in a small negative offset in ripple migration velocity. As far as the author is aware, these observations provide the first evidence of both onshore and offshore skewness–related ripple migration.

During storm growth, the wave power spectral density was bimodal and the bispectrum indicated a difference interaction between the sea and swell frequency waves, producing negative orbital velocity skewness. In contrast, during storm decay the orbital velocity had a single swell frequency spectral peak, and the bispectrum showed positive skewness arising through self–self interaction of the incident swell. The average negative orbital velocity skewness predicted by a finite–depth second–order wave interaction theory (Wells [1967], based on the two–frequency equations of Biésel [1952]) was $-0.10$, roughly consistent with the observations. A more complete wave description may be required to model the observed positive velocity skewness, which was overpredicted at 0.6. The range of validity of the second–order theory was exceeded in this case, as indicated by Ursell numbers greater than 0.3. Work is underway on implementation of the more general Hasselman et al. [1963] second–order theory which uses the full velocity spectrum.

In summary, therefore, the results presented in this thesis show that the direction of ripple migration in the wave shoaling region was either onshore or offshore depending on the sign of the nearbed wave orbital velocity skewness. Furthermore, the sign of the skewness was determined by nonlinear interactions between components of the wave field. In particular, sea–swell difference interactions produced negative skewness during storm growth, while swell–swell sum interactions produced positive skewness during storm decay. Presuming that ripple migration is related to sediment transport, these results suggest that skewness variation arising from sea–swell and swell–swell interactions is a possible mechanism for the commonly observed beach storm cycle.

# Bibliography


Allen, J. R. L. (1970). *Physical processes and sedimentation.* Unwin Univ. Books, London.

Allen, J. R. L. (1979). A model for the interpretation of wave ripple–marks using their wavelength, textural composition, and shape. *J. Geol. Soc. London*, 136:673–682.

Allen, J. R. L. (1982). *Sedimentary Structures Their Character and Physical Basis, Vols I and II.* Developments in Sedimentology 30A and B. Elsevier, New York.

Amos, C. L., Bowen, A. J., Huntley, D. A., Judge, J. T., and Li, M. Z. (1999). Ripple migration and sand transport under quasi–orthogonal combined flows in the Scotian Shelf. *J. Coastal Res.*, 15(1):1–14.

Bagnold, R. A. (1941). *The physics of blown sand and desert dunes.* Methuen and Co., Ltd., London.

Bagnold, R. A. (1946). Motion of waves in shallow water. Interaction between waves and sand bottoms. *Proc. Roy. Soc. London, A*, 187:1–18.

Bagnold, R. A. (1954). Experiments on a gravity–free dispersion of large solid spheres in a Newtonian fluid under shear. *Proc. Roy. Soc. London, A*, 225:49–63.

Bagnold, R. A. (1963). Beach and nearshore processes. In Hill, M. N., editor, *The Sea*, volume III, pages 507–553. Interscience, New York.

Bailard, J. A. and Inman, D. L. (1981). An energetics bedload model for a plane sloping beach: local transport. *J. Geophys. Res.*, 86(C3):2035–2043.

Biésel, F. (1952). Équations générals au second ordre de la houle irrégulaire. *Houille Blanche*, 3:372–376.

Bowen, A. J. (1980). Simple models of nearshore sedimentation; beach profiles and longshore bars. In McCann, S. B., editor, *The Coastline of Canada*, pages 1–11. Geological Survey of Canada.

Boyd, R., Forbes, D. L., and Heffler, D. E. (1988). Time–sequence observations of wave–formed sand ripples on an ocean shoreface. *Sedimentology*, 35:449–464.

Carstens, M. R., Nielson, F. M., and Altinbilek, H. D. (1969). Bed forms generated in the laboratory under an oscillatory flow: an analytical and experimental study. Technical Memo 28, U. S. Army Corps of Engineers, Coastal Engineering Research Center.

Clifton, H. E. (1976). Wave–formed sedimentary structures — a conceptual model. In Davis, Jr., R. A. and Ethington, R. L., editors, *Beach and Nearshore Sedimentation*, SEPM Special Pub. No. 24, pages 126–148. SEPM, Tulsa, OK.

Clifton, H. E. and Dingler, J. R. (1984). Wave–formed structures and paleoenvironmental reconstruction. *Mar. Geol.*, 60:165–198.

Clifton, H. E., Hunter, R. E., and Phillips, R. L. (1971). Depositional structures and processes in the non–barred high–energy nearshore. *J. Sed. Petrol.*, 41(3):651–670.

Conley, D. C. and Inman, D. L. (1992). Field observations of the fluid–granular boundary layer under near–breaking waves. *J. Geophys. Res.*, 97(C6):9631–9643.

Craig, R. G. A., Paul, W., and Hay, A. E. (1995). Networked acquisition system for multiple acoustic devices. In *Proc. 1995 Canadian Coastal Conf.*, volume 1, pages 153–170.

Crawford, A. M. and Hay, A. E. (1998). A simple system for laser–illuminated video imaging of sediment suspension and bed topography. *IEEE J. Ocean. Eng.*, 23(1):12–19.

Davidson-Arnott, R. G. D. and Greenwood, B. (1976). Facies relationships on a barred coast, Kouchibouguac Bay, New Brunswick, Canada. In Davis Jr., R. A. and Ethington, R. L., editors, *Beach and Nearshore Sedimentation*, SEPM Special Pub. No. 24, pages 149–168. SEPM, Tulsa, OK.

Dingler, J. R. (1974). *Wave formed ripples in nearshore sands*. PhD thesis, Univ. California, San Diego.

Dingler, J. R. and Clifton, H. E. (1984). Tidal–cycle changes in oscillation ripples on the inner part of an estuarine sand flat. *Mar. Geol.*, 60:219–233.

Dingler, J. R. and Inman, D. L. (1977). Wave–formed ripples in nearshore sands. In *Proc. 15th Coastal Eng. Conf., Vol. II*, pages 2109–2126. ASCE.

Doering, J. C. and Bowen, A. J. (1995). Parameterization of orbital velocity asymmetries of shoaling and breaking waves using bispectral analysis. *Coastal Eng.*, 26:15–33.

Dyer, K. R. (1980). Velocity profiles over a rippled bed and the threshold of movement of sand. *Est., Coastal and Mar. Sci.*, 10:181–199.

Dyer, K. R. and Soulsby, R. L. (1988). Sand transport on the continental shelf. *Ann. Rev. Fluid Mech.*, 20:295–324.

Elgar, S. and Guza, R. T. (1985a). Observations of bispectra of shoaling surface gravity waves. *J. Fluid Mech.*, 161:425–448.

Elgar, S. and Guza, R. T. (1985b). Shoaling gravity waves: comparisons between field observations, linear theory, and a nonlinear model. *J. Fluid Mech.*, 158:47–70.

Elgar, S. and Guza, R. T. (1986). Nonlinear model predictions of bispectra of shoaling surface gravity waves. *J. Fluid Mech.*, 167:1–18.

Elgar, S. and Guza, R. T. (1988). Statistics of bicoherence. *IEEE Trans. Acoust., Speech and Sig. Proc.*, 36(10):1667–1668.

Elgar, S., Herbers, T. H. C., Chandran, V., and Guza, R. T. (1995). Higher–order spectral analysis of nonlinear ocean surface gravity waves. *J. Geophys. Res.*, 100(C3):4977–4983.

Fournier, G. R., Bonnier, D., Forand, J. L., and Pace, P. W. (1993). Range–gated underwater laser imaging system. *Opt. Eng.*, 32(9):2185–2190.

Fredsøe, J. and Deigaard, R. (1992). *Mechanics of Coastal Sediment Transport*, volume 3 of *Advanced Series on Ocean Engineering*. World Scientific.

Gallagher, E. L., Boyd, W., Elgar, S., Guza, R. T., and Woodward, B. (1996). Performance of a sonar altimeter in the nearshore. *Mar. Geol.*, 133(3–4):241–248.

Gallagher, E. L., Elgar, S., and Guza, R. T. (1998). Observations of sand bar evolution on a natural beach. *J. Geophys. Res.*, 103(C2):3203–3215.

Grant, W. D. and Madsen, O. S. (1982). Movable bed roughness in unsteady oscillatory flow. *J. Geophys. Res.*, 87(C1):469–481.

Greenwood, B., Dingler, J. R., Sherman, D. J., Anima, R. J., and Bauer, B. (1985). Monitoring bedforms underwater using high resolution remote tracking sonars (HRRTS). In *Proc. 1985 Canadian Coastal Conf.*, pages 143–158.

Hanes, D. M., Vincent, C. E., Huntley, D. A., and Clarke, T. L. (1988). Acoustic measurements of suspended sand concentration in a wave–dominated nearshore environment. *Cont. Shelf Res.*, 6(4):585–596.

Hasselman, K., Munk, W., and MacDonald, G. (1963). Bispectra of ocean waves. In Rosenblatt, M., editor, *Time Series Analysis*, pages 125–139. John Wiley.

Hay, A. E. and Bowen, A. J. (1993). Spatially correlated depth changes in the nearshore zone during autumn storms. *J. Geophys. Res.*, 98(C7):12387–12404.

Hay, A. E. and Bowen, A. J. (2000). Alongshore migration of lunate megaripples during DUCK94: Part 1. *in press*.

Hay, A. E., Smyth, C., Zedel, L., and Mudge, T. (1999). On remotely probing the structure of the bottom boundary layer over an evolving seabed. In *Coastal Ocean Proc. Symp. Tech. Report*, pages 99–106, Woods Hole.

Hay, A. E. and Wilson, D. J. (1994). Rotary sidescan images of nearshore bedform evolution during a storm. *Mar. Geol.*, 119:57–65.

Henderson, S. and Bowen, A. J. (2000). Definition, interpretation and estimation of the bicoherence density. submitted to *J. Geophys. Res.*

Herbers, T. H. C. and Guza, R. T. (1991). Wind–wave nonlinearity observed at the sea floor. Part I: Forced–wave energy. *J. Phys. Ocean.*, 21:1740–1761.

Herbers, T. H. C. and Guza, R. T. (1994). Nonlinear wave interactions and high–frequency seafloor pressure. *J. Geophys. Res.*, 99(C5):10,035–10,048.

Holland, K. T., Holman, R. A., Lippmann, T. C., Stanley, J., and Plant, N. (1997). Practical use of video imagery in nearshore oceanographic field studies. *IEEE J. Ocean. Eng.*, 22(1):81–92.

Honjo, S., Doherty, K. W., Agrawal, Y. C., and Asper, V. L. (1984). Direct optical assessment of large amorphous aggregates (marine snow) in the deep ocean. *Deep–Sea Res.*, 31:67–76.

Horikawa, K., editor (1988). *Nearshore Dynamics and Coastal Processes*. University of Tokyo Press, Japan.

Inman, D. L. (1957). Wave–generated ripples in nearshore sands. Technical Memo 100, U. S. Army Corps of Engineers, Beach Erosion Board.

Jonsson, I. G. (1966). Wave boundary layers and friction factors. In *Proc. 10th Int. Conf. Coastal Eng.*, pages 127–148. ASCE.

Kawata, Y., Shirai, T., and Tsuchiya, Y. (1990). Field observations on sand ripples under rough sea state. In *Proc. 23th Conf. Coastal Eng.*, pages 2164–2174. ASCE.

Kim, Y. C. and Powers, E. J. (1979). Digital bispectral analysis and its applications to nonlinear wave interactions. *IEEE Trans. Plasma Sci.*, PS-7(2):120–131.

King, D. B. and Seymour, R. J. (1989). State of the art in oscillatory sediment transport models. In Seymour, R. J., editor, *Nearshore Sediment Transport*, pages 371–186. Plenum, New York.

Kraus, N. C. and Horikawa, K. (1990). Nearshore sediment transport. In Le Méhauté, B. and Hanes, D. M., editors, *The Sea*, volume 9, Part B, pages 775–813. John Wiley, New York.

Kulp, T. J., Garvis, D., Kennedy, R., Salmon, T., and Cooper, K. (1993). Development and testing of a synchronous–scanning underwater imaging system capable of rapid two–dimensional frame imaging. *Appl. Optics*, 32(19):3520–3530.

Lenz, J., Schnack, D., Petersen, D., Kreikemeier, J., Hermann, B., Mees, S., and Weiland, K. (1995). The ichthyoplankton recorder — a video recording–system for in–situ studies of small–scale plankton distribution patterns. *ICES J. Mar. Sci.*, 52(3–4):409–417.

Li, M. Z. and Amos, C. L. (1998). Predicting ripple geometry and bed roughness under combined waves and currents in a continental shelf environment. *Cont. Shelf Res.*, 18:941–970.

Lippmann, T. C., Thornton, E. B., and Reniers, A. J. H. M. (1996). Wave stress and longshore current on barred profiles. In *Proc. Coastal Dynamics '95*, pages 401–412, New York. ASCE.

Longuet-Higgins, M. S. (1957). The mechanics of the boundary–layer near the bottom in a progressive wave. In *Proc. 6th Int. Conf. Coastal Eng.*, pages 184–193. ASCE. Appendix to Russell, R. C. H. and Osorio, J. D. C.: An experimental investigation of drift profiles in a closed channel.

Longuet-Higgins, M. S. and Stewart, R. W. (1962). Radiation stress and mass transport on gravity waves, with application to 'surf beats'. *J. Fluid Mech.*, 13:481–504.

Madsen, O. S. and Grant, W. D. (1976). Quantitative description of sediment transport by waves. In *Proc. 15th Conf. Coastal Eng.*, pages 1093–1112. ASCE.

McLean, S. R. (1983). Turbulence and sediment transport measurements in a North Sea tidal inlet (The Jade). In Sunderman, J. and Lang, W., editors, *North Sea Dynamics*, pages 436–452. Springer–Verlag, Berlin.

Meyer-Peter, E. and Müller, R. (1948). Formulas for bed–load transport. In *Proc. 2nd Congr. Int. Assoc. Hyd. Res.*, volume 2, pages 39–64.

Miche, M. (1944). Movements ondulatoires de la mer en profondeur constante ou decroissante. *Ann. Ponts Chaussées*, 114:25–406.

Miller, M. C. and Komar, P. D. (1980a). A field investigation of the relationship between oscillation ripple spacing and the near–bottom water orbital motions. *J. Sed. Petrol.*, 50(1):183–191.

Miller, M. C. and Komar, P. D. (1980b). Oscillation sand ripples generated by laboratory apparatus. *J. Sed. Petrol.*, 50(1):173–182.

Mogridge, G. R. and Kamphuis, J. W. (1973). Experiments on bed form generation by wave action. In *Proc. 13th Coastal Eng. Conf., Vol. II*, pages 1123–1142. ASCE.

Nielsen, P. (1981). Dynamics and geometry of wave–generated ripples. *J. Geophys. Res.*, 86(C7):6467–6472.

Nomura, Y., Sagara, M., Naruse, H., and Ide, A. (1992). Simple calibration algorithm for high–distortion–lens camera. *IEEE Trans. Patt. Anal. Mach. Int.*, PAMI–14(11):1095–1099.

Norheim, C. A., Herbers, T. H. C., and Elgar, S. (1998). Nonlinear evolution of surface wave spectra on a beach. *J. Phys. Ocean.*, 28:1534–1551.

Osborne, P. D. and Vincent, C. E. (1993). Dynamics of large and small scale bedforms on a macrotidal shoreface under shoaling and breaking waves. *Mar. Geol.*, 115:207–226.

Phillips, O. M. (1960). On the dynamics of unsteady gravity waves of finite amplitude. Part 1. The elementary interactions. *J. Fluid Mech.*, 9:193–217.

Ratmeyer, V. and Wefer, G. (1996). A high–resolution camera system (ParCa) for imaging particles in the ocean: system design and results from profiles and a three–month deployment. *J. Mar. Res.*, 54:589–603.

Sherman, D. J. and Greenwood, B. (1984). Boundary roughness and bedforms in the surf zone. *Mar. Geol.*, 60:199–218.

Sleath, J. F. A. (1976). On rolling–grain ripples. *J. Hyd. Res.*, 14(1):69–81.

Sleath, J. F. A. (1982). The suspension of sand by waves. *J. Hyd. Res.*, 20(5):439–452.

Sleath, J. F. A. (1984). *Sea bed mechanics*. John Wiley and Sons, New York.

Sleath, J. F. A. (1994). Bed load transport in oscillatory flow. In Bélorgey, M., Rajaona, R. D., and Sleath, J. F. A., editors, *Sediment transport mechanisms in coastal environments and rivers, Euromech 310*, pages 93–106. World Scientific.

Sleath, J. F. A. (1995). Sediment transport by waves and currents. *J. Geophys. Res.*, 100(C6):10977–10986.

Sternberg, R. W. (1967). Measurements of sediment movement and ripple migration in a shallow marine environment. *Mar. Geol.*, 5:195–205.

Swart, D. H. (1974). Offshore sediment transport and equilibrium beach profiles. Technical Report Publ. No. 131, Delft Hyd. Lab.

Thornton, E. and Guza, R. T. (1983). Transformation of wave height distribution. *J. Geophys. Res.*, 88(C10):5925–5938.

Thornton, E. B. and Guza, R. T. (1989). Wind wave transformation. In Seymour, R. J., editor, *Nearshore Sediment Transport*, pages 137–171. Plenum.

Thornton, E. B., Swayne, J. L., and Dingler, J. R. (1998). Small–scale morphology across the surf zone. *Mar. Geol.*, 145:173–196.

Traykovski, P., Hay, A. E., Irish, J. D., and Lynch, J. F. (1999). Geometry, migration, and evolution of wave orbital ripples at LEO-15. *J. Geophys. Res.*, 104(C1):1505–1524.

Tusting, R. F. and Davis, D. L. (1992). Laser systems and structured illumination for quantitative undersea imaging. *Mar. Tech. Soc. J.*, 26(4):5–12.

Vincent, C. E., Hanes, D. M., and Bowen, A. J. (1991). Acoustic measurements of suspended sand on the shoreface and the control of concentration by bed roughness. *Mar. Geol.*, 96:1–18.

Vincent, C. E. and Osborne, P. D. (1993). Bedform dimensions and migration rates under shoaling and breaking waves. *Cont. Shelf Res.*, 13(11):1267–1280.

Wells, D. (1967). Beach equilibrium and second-order wave theory. *J. Geophys. Res.*, 72(2):497–504.

Wiberg, P. L. and Harris, C. K. (1994). Ripple geometry in wave–dominated environments. *J. Geophys. Res.*, 99(C1):775–789.

Wilkinson, R. H. (1986). Variation of roughness length of a mobile sand bed in a tidal flow. *Geo–Mar. Lett.*, 5:231–239.

Wilson, D. J. and Hay, A. E. (1995). High resolution sidescan sonar observations of small scale sand bedforms under waves: a comparison of field and laboratory measurements. In *Proc. 1995 Canadian Coastal Conf.*, volume 2, pages 875–890.

Yokokawa, M., Masuda, F., and Noritaka, E. (1995). Sand particle movement on migrating combined–flow ripples. *J. Sed. Res.*, A65(1):40–44.

Zedel, L. and Hay, A. E. (1999). A coherent doppler profiler for high–resolution particle velocimetry in the ocean: laboratory measurements of turbulence and particle flux. *J. Atmos. and Ocean. Tech.*, 16:1102–1117.

Zedel, L., Hay, A. E., Cabrera, R., and Lohrman, A. (1996). Performance of a single–beam pulse–to–pulse coherent doppler profiler. *IEEE J. Ocean. Eng.*, 21(3):290–297.

# Appendix A

# A Theory of Second–order Nonlinear Wave Interaction

The results of the bispectral analysis presented in Section 3.5 indicate that a difference interaction between wave trains at a pair of frequencies was responsible for the negative skewness of the nearbed orbital velocity observed during the growth phase of the storm (Interval I). In his 1967 paper, Wells gives an analytic form for the skewness of the orbital velocity arising from second–order interaction between a pair of wave trains, based on the work of Biésel [1952] and Miche [1944]. Biésel's equations, also appearing in Appendix 2 of Wells' paper, are given below.

The nearbed orbital velocity is given by

$$u = \sum_{i=1}^{N} \{\mathcal{A}_i \cos(k_i x - \omega_i t) + \mathcal{B}_i \cos 2(k_i x - \omega_i t)\}$$
$$+ \sum_{i=1}^{N} \sum_{j=1}^{i-1} \{\mathcal{S}_{ij} \cos[(k_i + k_j)x - (\omega_i + \omega_j)t] + \mathcal{D}_{ij} \cos[(k_i - k_j)x - (\omega_i - \omega_j)t]\} \quad \text{(A.1)}$$

where $\omega$ is the wave radian frequency, $k$ is the wave number and, in this case, $N$, the number of interacting wave trains, is 2. The coefficients are given by

$$\mathcal{A}_i = a_i \omega_i \frac{\cosh k_i(h - z)}{\sinh k_i h} . \quad \text{(A.2)}$$

$$\mathcal{B}_i = \frac{3}{4} a_i^2 \frac{k_i \omega_i \cosh 2k_i(h-z)}{\sinh^4 k_i h} , \tag{A.3}$$

$$\mathcal{S}_{ij} = \frac{a_i a_j}{2 \sinh k_i h \sinh k_j h} (k_i + k_j) \mathcal{E}_{ij} \cosh[(k_i + k_j)(h-z)] . \tag{A.4}$$

$$\mathcal{D}_{ij} = \frac{-a_i a_j}{2 \sinh k_i h \sinh k_j h} (k_i - k_j) \mathcal{F}_{ij} \cosh[(k_i - k_j)(h-z)] , \tag{A.5}$$

$$\mathcal{E}_{ij} = \frac{(\omega_i + \omega_j)(\omega_i^2 + \omega_i \omega_j + \omega_j^2) - \mathcal{C}'^2_{gij}(k_i \omega_i - k_j \omega_j)(k_i - k_j)}{(\omega_i + \omega_j)^2 \left[1 - \left(\frac{\mathcal{D}'_{gij}}{\mathcal{D}_{gij}}\right)^2\right]} \frac{\cosh(k_i - k_j)h}{\cosh(k_i + k_j)h} , \tag{A.6}$$

$$\mathcal{F}_{ij} = \frac{(\omega_i - \omega_j)(\omega_i^2 - \omega_i \omega_j + \omega_j^2) - \mathcal{D}'^2_{gij}(k_i \omega_i - k_j \omega_j)(k_i + k_j)}{(\omega_i - \omega_j)^2 \left[1 - \left(\frac{\mathcal{C}'_{gij}}{\mathcal{C}_{gij}}\right)^2\right]} \frac{\cosh(k_i + k_j)h}{\cosh(k_i - k_j)h} , \tag{A.7}$$

$$\mathcal{C}'_{gij} = \left[\frac{g}{k_i - k_j} \tanh(k_i - k_j)h\right]^{1/2} . \tag{A.8}$$

$$\mathcal{C}_{gij} = \frac{\omega_i - \omega_j}{k_i - k_j} , \tag{A.9}$$

$$\mathcal{D}'_{gij} = \left[\frac{g}{k_i + k_j} \tanh(k_i + k_j)h\right]^{1/2} . \tag{A.10}$$

$$\mathcal{D}_{gij} = \frac{\omega_i + \omega_j}{k_i + k_j} . \tag{A.11}$$

The coefficients $\mathcal{A}_i$ and $\mathcal{B}_i$ are the Stokes expansion coefficients, Equations 1.11 and 1.12. This expression for $u$, therefore, derives from considering, in addition to the harmonic

term, the higher–order sum ($\mathcal{S}_{ij}$) and difference ($\mathcal{D}_{ij}$) frequency terms. It is required that the full dispersion relation be used in relating $k$ and $\omega$, i.e.

$$\omega_i^2 = gk_i \tanh k_i h \ . \tag{A.12}$$

As Biésel [1952] noted, these equations are not suitable for use in very shallow water since the quantities $\mathcal{E}_{ij}$ and $\mathcal{F}_{ij}$ become unstable as the ratios $\mathcal{D}'_{gij}/\mathcal{D}_{gij}$ and $\mathcal{C}'_{gij}/\mathcal{C}_{gij}$ approach 1.

The orbital velocity skewness is then given by

$$S = \frac{E[u^3]}{E[u^2]^{3/2}} \tag{A.13}$$

where Wells [1967] derived the second and third moments of $u$ as

$$E[u^2] = \frac{1}{2}\sum_{i=1}^{N}(\mathcal{A}_i^2 + \mathcal{B}_i^2) + \frac{1}{2}\sum_{i=1}^{N}\sum_{j=1}^{i-1}(\mathcal{S}_{ij}^2 + \mathcal{D}_{ij}^2) \tag{A.14}$$

and

$$E[u^3] = \frac{3}{4}\sum_{i=1}^{N}\mathcal{A}_i^2\mathcal{B}_i + \frac{3}{2}\sum_{i=1}^{N}\sum_{j=1}^{i-1}(\mathcal{A}_i\mathcal{A}_j\mathcal{S}_{ij} + \mathcal{A}_i\mathcal{A}_j\mathcal{D}_{ij}) \ . \tag{A.15}$$

This approach for determining the nearbed velocity skewness has been referred to in the text (Chapter 3) as the MBW method.

A principal result reported by Wells [1967] is the suggestion of water depth dependence of the nearbed velocity skewness calculated for a pair of wave trains, with positive values near shore and negative values in deeper water. Note that the velocity skewness at a particular water depth is calculated as if the bottom were flat at that location, independent of bottom slope or wave shoaling behaviour. Figure A.1 illustrates the depth dependence of the skewness calculated by the MBW method for pairs of waves with the peak wave periods and amplitudes taken from surface elevation spectra at two times in Interval I (dashed lines). The 6:15 GMT run gave results similar to the 5:45 GMT run and is not shown. In shallow water, the curves terminate where the water depth reaches 0.8 times the wave height of the larger of the two input waves, a standard wave height breaking criterion [Fredsøe and Deigaard, 1992]. At the depth that the measurements were made (indicated

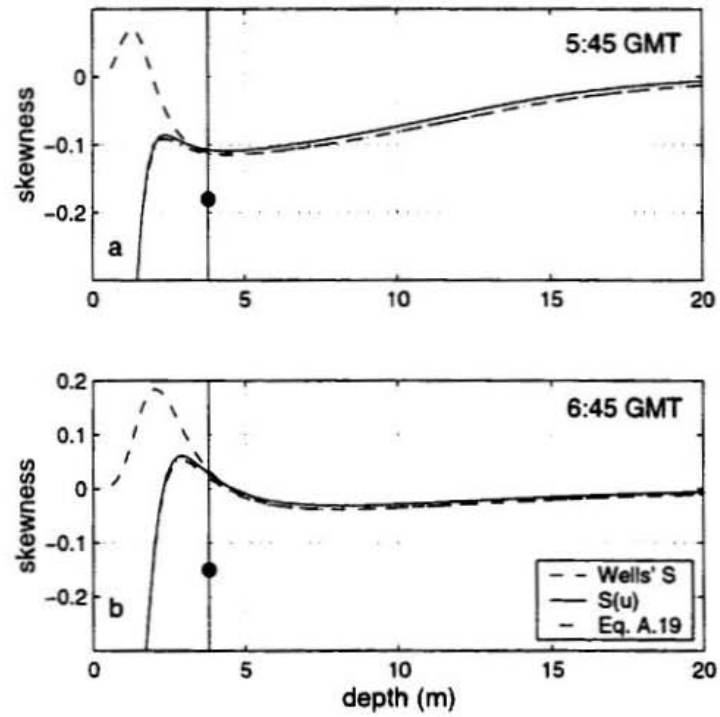


Figure A.1: Skewness as a function of depth calculated by the MBW method at 5:45 GMT (a) and at 6:45 GMT (b). The water depth at the instrument location is marked by a vertical line. The dashed lines show the skewness calculated from Equations A.14 and A.15. The solid lines show skewness of $u$ time series constructed using Equation A.1. The dash-dotted lines show the result of an adjustment to the MBW skewness calculation discussed in the text. The skewness of the CDP measured velocity at each time is indicated by the symbols (•).

by the vertical line), the skewness of the velocity measured by the CDP is also shown. The solid curve shows the skewness calculated directly from the velocity given by Equation A.1.

The dashed and solid curves in Figure A.1 show a marked divergence in shallow water, near the depth where measurements were made. The reason for this divergence was investigated by writing $u$ (Equation A.1) as

$$u = \Gamma_1 + \Gamma_2 \,. \tag{A.16}$$

where $\Gamma_1$ includes the $\mathcal{A}_i$ and $\mathcal{B}_i$ (Stokes) terms and $\Gamma_2$, the $\mathcal{S}_{ij}$ and $\mathcal{D}_{ij}$ terms. The third moment of $u$ is then given by

$$E[u^3] = \langle u^3 \rangle = \langle (\Gamma_1 + \Gamma_2)^3 \rangle \tag{A.17}$$

or as the sum of four terms

$$E[u^3] = \langle \Gamma_1^3 + 3\Gamma_1^2\Gamma_2 + 3\Gamma_1\Gamma_2^2 + \Gamma_2^3 \rangle \ . \tag{A.18}$$

In Wells' derivation, products of the higher–order coefficients $\mathcal{B}_i$, $\mathcal{S}_{ij}$ and $\mathcal{D}_{ij}$ are assumed to be small, which results in the $\Gamma_1\Gamma_2^2$ and $\Gamma_2^3$ terms (terms 3 and 4) being neglected. Terms 1 and 2 give Equation A.15.

Figure A.2 shows the four terms of Equation A.18 as functions of water depth for the same wave amplitudes and frequencies as in Figure A.1. It can be seen that the third term can have finite size in shallow water, while the fourth term remains appropriately small. Figure A.3 shows the Ursell numbers as a function of depth calculated for the two wave trains at each of the two times. The six Ursell numbers were defined in Section 3.6 in discussion relating to Table 3.3, where the values at the measurement depth are presented. The traditionally defined Ursell numbers ($Ur$ and $Ur'$) are still small at the point where the two skewness calculations diverge ($< 0.1$ in 3 of 4 cases shown), however the sum and difference coefficient Ursell numbers are larger. This points to the source of the divergence between the two skewness calculations.

The many terms of the full expansion for the third moment of $u$ were re–examined based on the results shown in Figure A.2. Two additional terms remain after time averaging which are non–vanishing for finite $Ur_S$ and $Ur_D$. Including these higher order terms, Equation A.15 with $N = 2$ becomes

$$E[u^3] = \frac{3}{4}\sum_{i=1}^{2} \mathcal{A}_i^2\mathcal{B}_i + \frac{3}{2}(\mathcal{A}_2\mathcal{A}_1\mathcal{S}_{21} + \mathcal{A}_2\mathcal{A}_1\mathcal{D}_{21}) + \frac{3}{2}(\mathcal{B}_1\mathcal{S}_{21}\mathcal{D}_{21} + \mathcal{B}_2\mathcal{S}_{21}\mathcal{D}_{21}) \ . \tag{A.19}$$

Note the ordering of the terms: $\frac{3}{4}O(a^4)$, $\frac{3}{2}O(a^4)$ and $\frac{3}{2}O(a^6)$. The dash–dotted lines in Figure A.1, calculated using Equations A.14 and A.19, indicate that these terms account for the difference between the two skewness calculations. The fact that these product terms

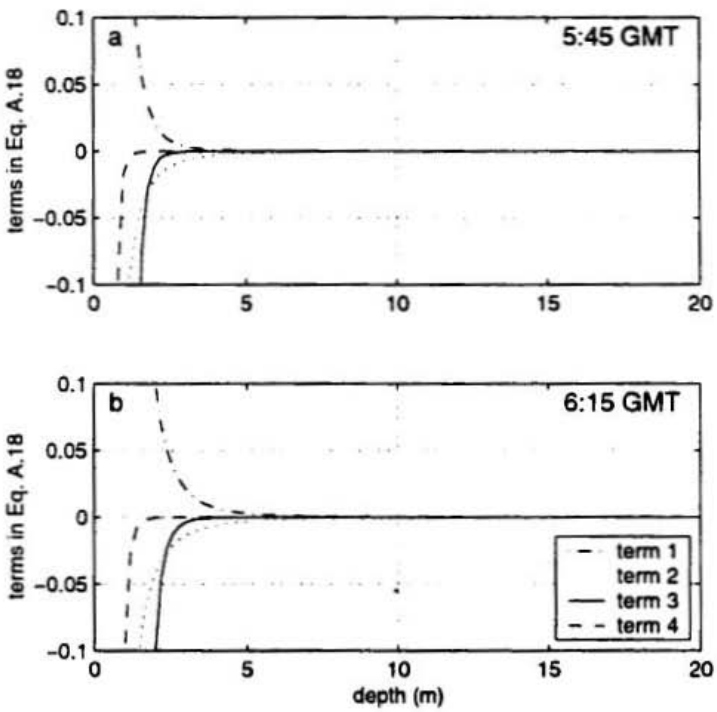


Figure A.2: The four terms of Equation A.18 for the wave heights and periods at 5:45 GMT (a) and 6:45 GMT (b).

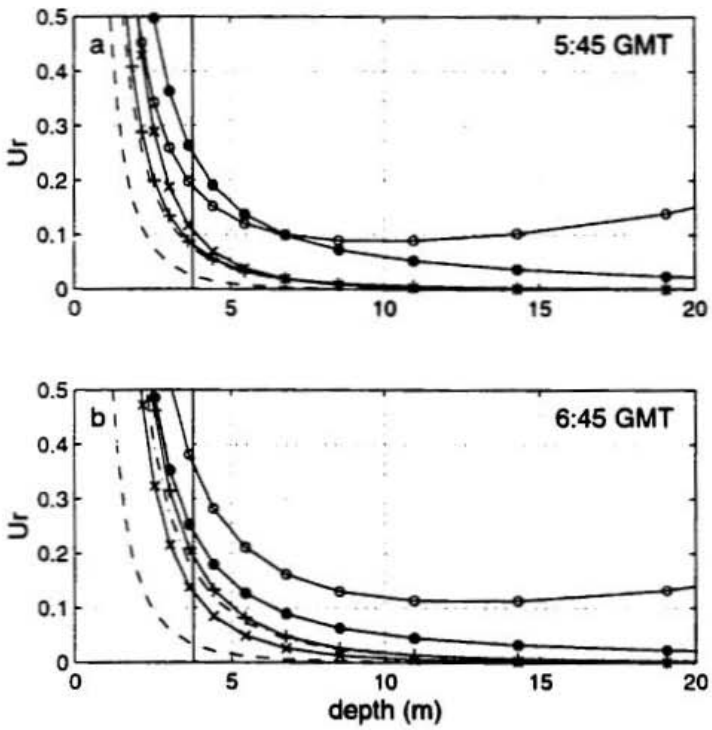


Figure A.3: Ursell numbers as a function of depth at 5:45 GMT (a) and 6:45 GMT (b), with line styles as follows: $Ur$ $-\cdot-$; $Ur'$ $--$; $Ur_S$ $-\times-$; $Ur'_S$ $-+-$; $|Ur_D|$ $-\circ-$; $|Ur'_D|$ $-\bullet-$.

can have finite size in very shallow water brings Wells' result of positive velocity skewness near shore into question. The results of the comparison of velocity skewness values shown in Table 3.3 are not invalidated by this, however, since the measurement depth fell (barely) in the region where these higher order terms remain small.

# Appendix B

# Velocity Dependence Considerations

It was stated in Section 3.3 that the observed ripple migration velocity was well correlated with the skewness of the nearbed orbital velocity, and to the cube of the orbital velocity, where the orbital velocity is the demeaned total velocity. The following discussion concerns correlation of ripple migration velocity to other higher powers of orbital velocity and implications of the non–zero mean velocity.

Figure B.1 shows regressions of the ripple migration velocity against a range of odd powers of the demeaned orbital velocity, $u^{\xi}$ where $\xi$ ranges from 3 to 7, and against velocity skewness. Ripple migration velocity was not significantly correlated with demeaned velocity squared ($r^2 < 0.1$). The results shown demonstrate that the observations also support dependence of ripple migration velocity on the fifth power of the nearbed velocity. This is not entirely surprising as $u^3$ and $u^5$ are themselves correlated ($r^2 > 0.9$). The correlation between ripple migration velocity and the seventh power of orbital velocity, however, is much poorer.

The nearbed velocity measured by the CDP was demeaned to determine the orbital velocity, that part of the total nearbed velocity due to the waves directly. If the total velocity, $u_{\text{total}} = \mathcal{U} + u$, is considered, the effect of the mean velocity $\mathcal{U}$ on quantities based on the time average of velocity cubed can be assessed by examining the cross term $3\mathcal{U}u^2$. Figure B.2 illustrates this quantity compared with $u^3$, and normalized by $E[u^2]^{3/2}$, compared with the skewness of $u$.

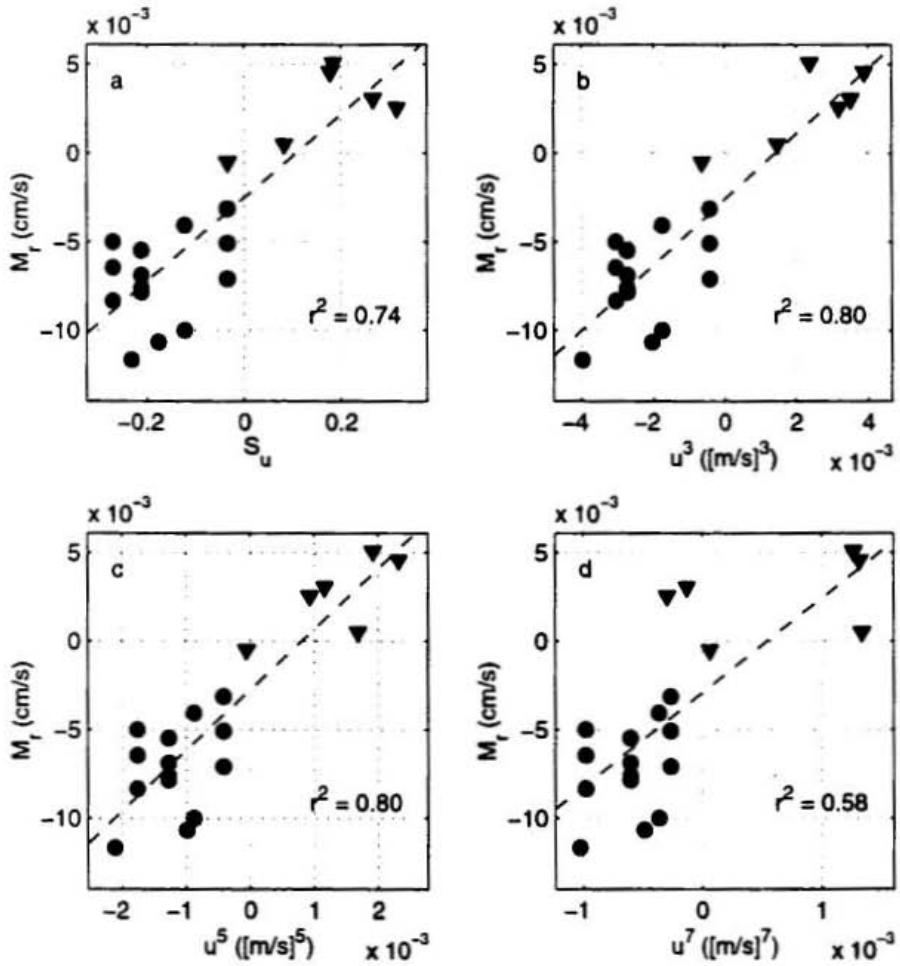


Figure B.1: Regressions of ripple migration velocity and a range of odd power orbital (demeaned) velocity quantities: skewness (a); velocity cubed (b); velocity to the fifth power (c) and velocity to the seventh power (d). Measurements during Interval I are shown by • symbols and during Interval II, by ▼ symbols.

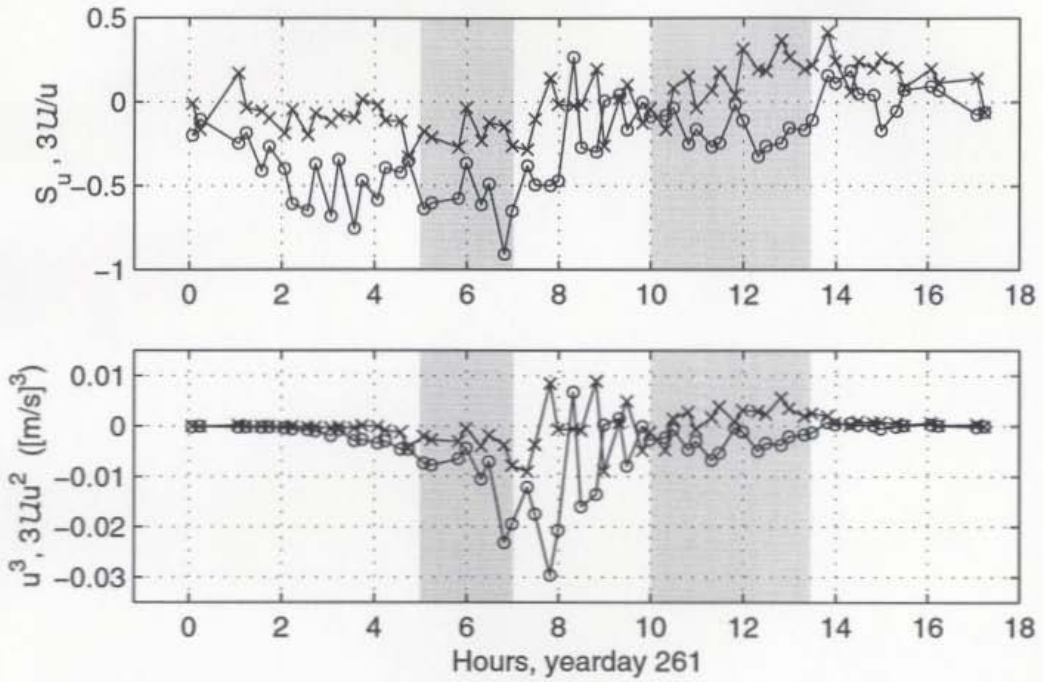


Figure B.2: Contribution of the mean velocity to $u^3_{\text{total}}$, in (a) normalized (–○–) and compared to the skewness of $u$ (–×–), and in (b) unnormalized (–○–), compared to $u^3$ (–×–). The time periods Intervals I and II are shaded gray.

The sense of the mean velocity cross term contribution to $u^3_{\text{total}}$ during both Intervals I and II is negative, or offshore, even during the time when ripples were migrating onshore in Interval II. The dynamical significance of this term may be in the negative offset in ripple migration velocity seen in all the regressions in Figure B.1. Including the mean velocity, i.e. regressing to $u^{\xi}_{\text{total}}$, does not significantly affect the correlation coefficients for the cases shown in Figure B.1, but reduces the migration velocity offset to near zero, as shown in Figure B.3. The negative mean nearbed velocity contribution in Interval II is not large enough to reverse the sign of the largest positive $u^{\xi}$ values.

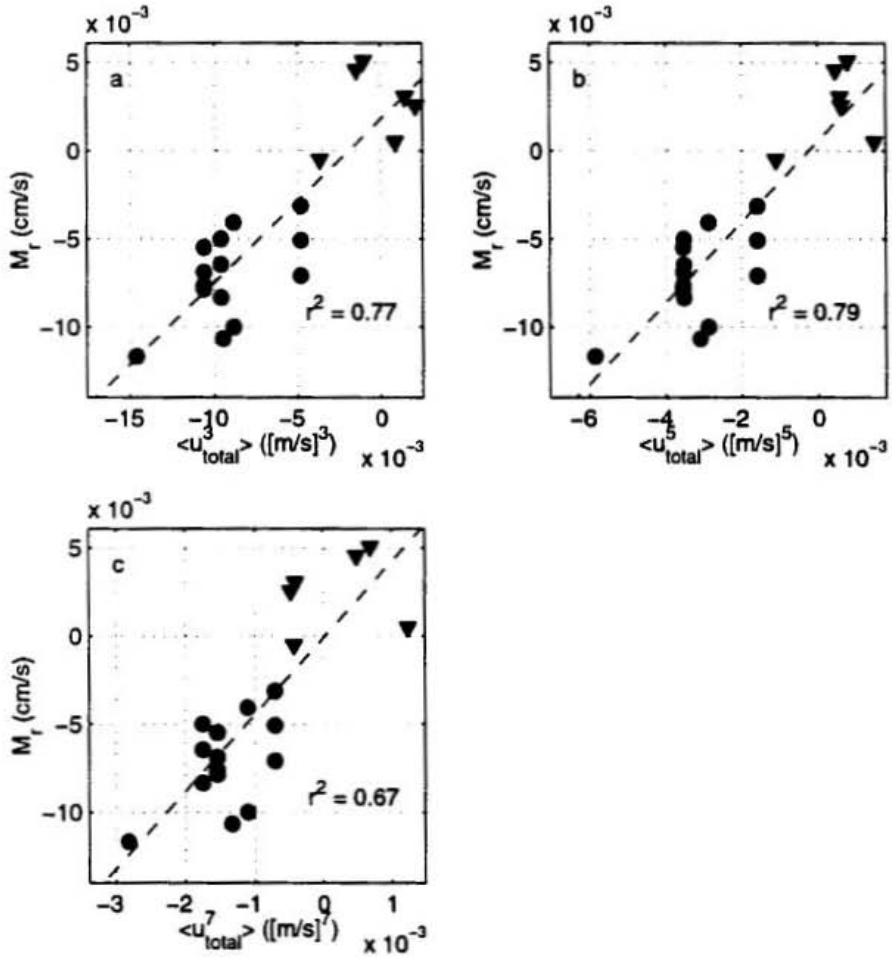


Figure B.3: Regressions of ripple migration velocity and a range of odd power total velocity quantities: total velocity cubed (a); total velocity to the fifth power (b) and total velocity to the seventh power (c). Measurements during Interval I are shown by • symbols and during Interval II, by ▼ symbols.